

# Efficient Turbulence Modeling for CFD Wake Simulations

**van der Laan, Paul**

*Publication date:*
2014

*Document Version*
Publisher's PDF, also known as Version of record

# Efficient Turbulence Modeling for CFD Wake Simulations

DTU Wind Energy - PhD

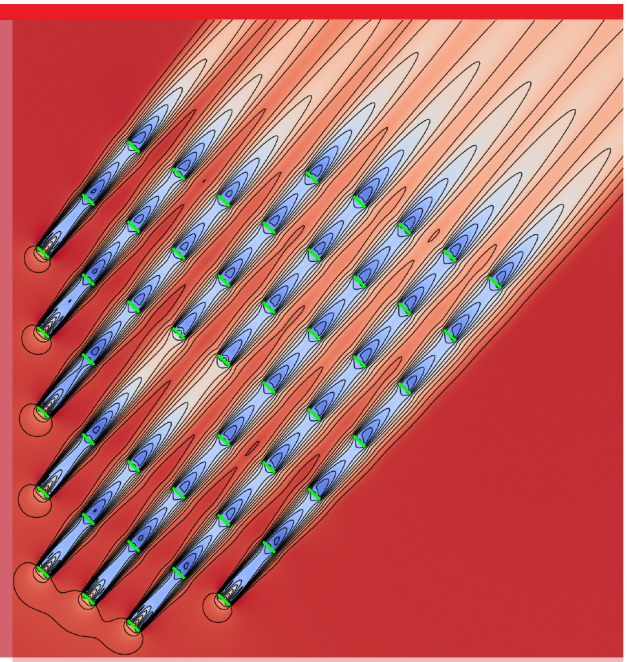

M. Paul van der Laan
DTU Wind Energy PhD-0047(EN)
December 2014

# Efficient Turbulence Modeling for CFD Wake Simulations

M. Paul van der Laan
December 2014

DTU Wind Energy
Department of Wind Energy

DTU

**Author:** M. Paul van der Laan
**Title:** Efficient turbulence modeling for CFD wake simulations
**Division:** Department of Wind Energy

Abstract:

Wind turbine wakes can cause 10-20% annual energy losses in wind farms, and wake turbulence can decrease the lifetime of wind turbine blades. One way of estimating these effects is the use of computational fluid dynamics (CFD) to simulate wind turbines wakes in the atmospheric boundary layer. Since this flow is in the high Reynolds number regime, it is mainly dictated by turbulence. As a result, the turbulence modeling in CFD dominates the wake characteristics, especially in Reynolds-averaged Navier-Stokes (RANS). The present work is dedicated to study and develop RANS-based turbulence models, that can accurately and efficiently simulate wind turbine wakes.
The linear $k$-$\varepsilon$ eddy viscosity model (EVM) is a popular turbulence model in RANS; however, it underpredicts the velocity wake deficit and cannot predict the anisotropic Reynolds-stresses in the wake. In the current work, nonlinear eddy viscosity models (NLEVM) are applied to wind turbine wakes. NLEVMs can model anisotropic turbulence through a nonlinear stress-strain relation, and they can improve the velocity deficit by the use of a variable eddy viscosity coefficient, that delays the wake recovery. Unfortunately, all tested NLEVMs show numerically unstable behavior for fine grids, which inhibits a grid dependency study for numerical verification. Therefore, a simpler EVM is proposed, labeled as the $k$-$\varepsilon$-$f_P$ EVM, that has a linear stress-strain relation, but still has a variable eddy viscosity coefficient. The $k$-$\varepsilon$-$f_P$ EVM is numerically verified with a grid dependency study. With respect to the standard $k$-$\varepsilon$ EVM, the $k$-$\varepsilon$-$f_P$ EVM compares better with measurements of the velocity deficit, especially in the near wake, which translates to improved power deficits of the first wind turbines in a row. When the CFD methology is applied to a large wind farm, the simulated results cannot be compared directly with wind farm measurements that have a high uncertainty in the measured reference wind direction. When this uncertainty is used to post-process the CFD results, a fairer comparison with measurements is achieved.
*The thesis is submitted to the Danish Technical University in partial fulfillment of the requirements for the PhD degree.*

**DTU PhD-0047(EN)**
**December 2014**

**ISBN**
**978-87-93278-31-8**

**Sponsorship:**
The Center for Computational Wind Turbine Aerodynamics and Atmospheric Turbulence, funded by the Danish Council for Strategic Research (grant number 09-067216)

**Pages: 136**
**References: 81**
**Figures: 57**
**Tables: 22**

Department of Wind Energy
Technical University of Denmark
Risø Campus, 118
Frederiksborgvej 399
DK-4000 Roskilde
Denmark
Telephone: +45 24921678
plaa@dtu.dk
www.vindenergi.dtu.dk

# ABSTRACT IN DANISH

Kølvandet bag vindmøller kan forårsage 10-20% tab i den årlige energiproduktion i en vindmøllepark, og den ekstra turbulens der genereres i møllens kølvand kan desuden forårsage en nedsat levetid af møller der er påvirket af kølvandet. Der eksisterer en lang række modeller til vurdering af disse effekter, og en af de mere avancerede metoder er baseret på en koblet simulering af det atmosfæriske grænselag og kølvandseffekterne ved brug af Computational Fluid Dynamics (CFD). Strømningen i det atmosfæriske grænselag og i møllens kølvand er typisk karakteriseret ved meget høje Reynoldstal, og dermed styret af turbulent opblanding med negligibel viskose effekter. Som en konsekvens af dette, spiller turbulensmodelleringen en stor rolle for nøjagtigheden af de modellerede kølvandseffekter, specielt i forbindelse med de såkaldte Reynolds-Averaged Navier-Stokes (RANS) modeller. I dette Ph.D. arbejde er der fokuseret på udvikling og anvendelse af RANS turbulensmodeller, med henblik på at opnå høj nøjagtighed og effektivitet.

En af de mest anvendte turbulensmodeller i forbindelse med RANS simuleringer, er den lineære Eddy Viscosity Model (EVM). Det er dog velkendt, at den lineære EVM overestimerer henfaldet af møllens kølvand og mangler beskrivelsen af de anisotropiske effekter af turbulensen. Det er på denne baggrund, at dette Ph.D. projekt har fokuseret på anvendelsen af Non-Linear Eddy Viscosity Models (NLEVMs) til simulering af kølvandseffekter bag møller og i vindmølleparker. NLEVMs har den fordel, at de kan beskrive de anisotropiske Reynoldsspændinger i kølvandet bag møllen ved brug af ikke-lineære relationer mellem spændinger og forskydninger og desuden kan forbedre bestemmelsen af kølvandets henfald ved brug af en variable eddyviskositetskoefficient. En uheldig egenskab ved den implementerede og testede NLEVMs er dens numeriske ustabilitet. Netforninings studier har vist at modellen er ustabil på højopløste beregningsnet, og konsekvensen af dette er, at modellen ikke kan benyttes i forbindelse med en standard netforfiningstest.

For at undgå dette problem, blev en simplere EVM foreslået, her kaldet $k$-$\varepsilon$-$f_p$ eddy viscosity modellen. Denne model har en lineær relation mellem forskydning og spænding, men bibeholder den variable eddyviskositetskoefficient. Der er blevet udført netforfiningstest af den udviklede $k$-$\varepsilon$-$f_p$ EVM, og det er for en række problemer eftervist, at den har gode konvergensegenskaber ved gentagne netforfininger. Den udviklede $k$-$\varepsilon$-$f_p$ EVM, har sammenlignet med den gængse $k$-$\varepsilon$ EVM bedre overensstemmelse med målinger og Large Eddy Simulation (LES) i kølvandet tæt bag en mølle. Denne egenskab er specielt vigtig ved forudsigelse af produktionen fra de første rækker af vindmøller i

store vindmølleparker.

Sammenligningen af simuleringer med målinger fra fuldskala vindmølleparker er ikke nogen let øvelse, bl.a. på grund af den store usikkerhed som referencevindhastigheden er behæftet med. I det nærværende arbejde er der benyttet en procedure, der kan korrigere CFD beregningerne for denne usikkerhed, og dermed opnå en mere retvisende sammenligning af beregninger og målinger.

# ACKNOWLEDGEMENTS

The past three years have been great experience. I was in the lucky position to have access to four knowledgeable supervisors, who have been a great support during my PhD. First of all, I would like to thank my main supervisor Niels Sørensen for sharing his ideas, daily trouble shooting, and giving me the freedom to choose my own research path. I would also like to express my gratitude to my co-supervisors: Pierre-Elouan Réthoré, who gave useful feedback in planning and writing articles, Mark Kelly, who gave inspirational ideas through interesting discussions, and Jakob Mann, who taught me that the fun of research is cooperation and knowledge sharing. There are also other colleagues who have contributed to this work. For example, I would like to thank Niels Troldborg for sharing his knowledge about wind turbine wake simulations using LES, Ewan Machefaux for providing his wake measurements, Patrick Volker and Rogier Floors for their fruitful discussions about meteorological physics with respect to wakes, Kurt Hansen and Juan Pablo Murcia for their feedback on wind farm measurements, and all others that I forgot to mention here.

Furthermore, I am thankful that Niels Troldborg helped me to organize an external stay at the University of Auckland, New Zealand. My colleagues in Auckland: Rupert Storey, Stuart Norris and John Cater, have made this stay abroad a very pleasant one, and I would like to thank them for this. It could not have been such a great experience, without their positive input.

I have also received help from my home country, the Netherlands. The discussions with Gerard Schepers about the field measurements of the Dutch wind farm Wieringermeer were very useful for comparison with CFD results.

In addition, this work could not have been carried out without the financial support of the Center for Computational Wind Turbine Aerodynamics and Atmospheric Turbulence, which is funded by the Danish Council for Strategic Research, grant number 09-067216.

Finally, I would like to thank my friends and family, especially my lovely wife Lina Carolina, who has always been a great support.

# DISSEMINATION

## Peer-reviewed journal articles

**van der Laan, M. P.**, Sørensen, N. N., Réthoré, P.-E., Mann, J., Kelly, M. C., Troldborg, N., Schepers, J. G. and Machefaux, E. An improved $k$-$\varepsilon$ model applied to a wind turbine wake in atmospheric turbulence. *Wind Energy*, 2014, Published online: DOI: 10.1002/we.1736.

**van der Laan, M. P.**, Sørensen, N. N., Réthoré, P.-E., Mann, J., Kelly, M. C. and Troldborg, N. The $k$-$\varepsilon$-$f_P$ model applied to double wind turbine wakes using different actuator disk force methods. *Wind Energy*, 2014, Published online: DOI: 10.1002/we.1816.

**van der Laan, M. P.**, Sørensen, N. N., Réthoré, P.-E., Mann, J., Kelly, M. C., Troldborg, N., Hansen, K. S. and Murcia, J. P. The $k$-$\varepsilon$-$f_P$ model applied to wind farms. *Wind Energy*, 2014, Published online: DOI: 10.1002/we.1804.

Réthoré, P.-E., **van der Laan, M. P.**, Troldborg, N., Zahle, F. and Sørensen, N. N. Verification and validation of an actuator disc model. *Wind Energy*, 17:919-937, 2014, DOI: 10.1002/we.1607

## Peer-reviewed conference proceedings

**van der Laan, M. P.**, Sørensen, N. N., and Réthoré,P.-E., Mann, J., Kelly, M. C. and Schepers, J. G. Nonlinear Eddy Viscosity Models applied to Wind Turbine Wakes. In *Proceedings of International Conference on Aerodynamics of Offshore Wind Energy Systems and Wakes*, pages 514-525, 2013, link.

**van der Laan, M. P.**, Storey, R. C., Sørensen, N. N, Norris, S. E. and Cater, J. E. A CFD code comparison of wind turbine wakes. In *Journal of Physics: Conference Series 524, 012140*, 2014, DOI: 10.1088/1742-6596/524/1/012140

# NOMENCLATURE

Only global abbreviations and symbols are listed.

## Abbreviations

| | |
|---|---|
| ABL | atmospheric boundary layer |
| AD | actuator disk |
| AL | actuator line |
| CFD | computational fluid dynamics |
| DES | detached-eddy simulation |
| EVM | eddy viscosity model |
| LES | large-eddy simulation |
| MM | meteorological mast |
| NLEVM | nonlinear eddy viscosity model |
| RANS | Reynolds-averaged Navier-Stokes |
| RSM | Reynolds-stress model |
| SCADA | supervisory control and data acquisition |
| TSR | tip speed ratio |

## Roman symbols

| | | |
|---|---|---|
| $\mathbf{a} = a_{ij} \equiv \overline{u_i' u_j'}/k - \frac{2}{3}\delta_{ij}$ | normalized anisotropic Reynolds-stress tensor | $[-]$ |
| $\tilde{a}_{ij}$ | $a_{ij}$ in the calibration flow | $[-]$ |
| $a_x$ | axial induction, eq. (5.4) | $[-]$ |
| $C_P = P/(\frac{1}{2}\rho\pi R^2 U_{H,\infty}^3)$ | power coefficient | $[-]$ |
| $C_R$ | (Rotta) constant in model for $\mathscr{R}_{ij}^s$, eq. (2.18) | $[-]$ |
| $C_T = F_N/(\frac{1}{2}\rho\pi R^2 U_{H,\infty}^2)$ | thrust coefficient | $[-]$ |
| $C_2$ | constant in model for $\mathscr{R}_{ij}^r$, eq. (2.19) | $[-]$ |
| $C_{\varepsilon,1}$, $C_{\varepsilon,2}$ | constants in transport model for $\varepsilon$, eq. (2.63) | $[-]$ |
| $C_\mu$ | eddy viscosity coefficient | $[-]$ |
| $C_\mu^*$ | variable eddy viscosity coefficient | $[-]$ |
| $D$ | rotor diameter | $[m]$ |
| $F_N$ | normal rotor force, eq. (4.12) | $[N]$ |
| $f_P$ | scalar limiter function, eq. (2.57) and eq. (2.58) | $[-]$ |

| | | |
|---|---|---|
| $f_0$ | constant in $f_P$, eq. (2.58) | $[-]$ |
| $G^{(\lambda)}$ | scalar functions of NLEVMs, eq (2.28) | $[-]$ |
| $I_{H,\infty} = \sqrt{\frac{2}{3}k}/U_{H,\infty}$ | total turbulent intensity at hub height, in the free-stream | $[-]$ |
| $I_{u,H,\infty} = \sqrt{\sigma_u}/U_{H,\infty}$ | streamwise turbulent intensity at hub height, in the free-stream | $[-]$ |
| $k \equiv \frac{1}{2}\overline{u_i u_i'}$ | turbulent kinetic energy | $[m^2 s^{-2}]$ |
| $L$ | Monin-Obukhov length | $[m]$ |
| $n$ | number of blades | $[-]$ |
| $P$ | mean pressure | $[Nm^{-2}]$ |
| | rotor power, eq. (4.12) | $[kW]$ |
| $p'$ | fluctuating pressure | $[Nm^{-2}]$ |
| $\mathscr{P}_{ij}$ | production rate of Reynolds-stress, eq. (2.4) | $[m^2 s^{-3}]$ |
| $\mathscr{P} \equiv \frac{1}{2}\mathscr{P}_{ll}$ | production rate of turbulent kinetic energy | $[m^2 s^{-3}]$ |
| $q_N$ | distribution of normal blade force | $[Nm^{-1}]$ |
| $q_T$ | distribution of tangential blade force | $[Nm^{-1}]$ |
| $R$ | rotor radius | $[m]$ |
| $r$ | radial coordinate | $[m]$ |
| $\mathscr{R}_{ij}$ | pressure-rate-of-strain tensor, eq. (2.5) | $[m^2 s^{-3}]$ |
| $\mathscr{R}^s_{ij}$ | slow part of $\mathscr{R}_{ij}$, eq. (2.18) | $[m^2 s^{-3}]$ |
| $\mathscr{R}^r_{ij}$ | rapid part of $\mathscr{R}_{ij}$, eq. (2.19) and eq. (2.20) | $[m^2 s^{-3}]$ |
| $\mathbf{s} = s_{ij} \equiv \frac{1}{2}\frac{k}{\varepsilon}(U_{i,j} + U_{i,j})$ | normalized strain rate tensor | $[-]$ |
| $T_{kij}$ | Reynolds-stress flux, eq. (2.3) | $[m^3 s^{-3}]$ |
| $T^{(\lambda)}$ | Tensor groups of NLEVMs, eq. (2.25) and eq. (2.52) | $[-]$ |
| $U_i = [U, V, W]$ | mean velocity in Cartesian coordinates | $[ms^{-1}]$ |
| $\langle U_{AD} \rangle$ | disk-averaged velocity at the AD | $[ms^{-1}]$ |
| $U_{H,\infty}$ | free-stream at hub height | $[ms^{-1}]$ |
| $u_i' = [u', v', w']$ | fluctuating velocity in Cartesian coordinates | $[ms^{-1}]$ |
| $u_*$ | friction velocity | $[ms^{-1}]$ |
| $\overline{u_i' u_j'}$ | Reynolds-stress tensor | $[m^2 s^{-2}]$ |
| $x_i = [x, y, z]$ | Cartesian coordinates | $[m]$ |
| $z_H$ | hub height | $[m]$ |
| $z_0$ | roughness height | $[m]$ |

# Greek symbols

| | | |
|---|---|---|
| $\alpha, \beta, \gamma$ | parameters in implicit algebraic RSM, eq. (2.22) and eq. (2.23) | $[-]$ |
| $\delta_{ij} = \mathbf{I}$ | Kronecker delta | $[-]$ |
| $\varepsilon_{ij}$ | dissipation rate of Reynolds-stress, eq. (2.6) | $[m^2 s^{-3}]$ |
| $\varepsilon \equiv \frac{1}{2}\varepsilon_{ll}$ | dissipation rate of turbulent kinetic energy | $[m^2 s^{-3}]$ |
| $\eta_i$ | invariants in scalar functions $G^{(\lambda)}$, eq. (2.27) | $[-]$ |
| $\theta$ | angular coordinate | [rad] |
| $\theta_p$ | blade pitch | $[^\circ]$ |
| $\kappa$ | Von Kármán constant | $[-]$ |
| $\nu_T \equiv C_\mu k^2/\varepsilon$ | (kinematic) eddy viscosity | $[m^2 s^{-1}]$ |
| $\nu$ | kinematic molecular viscosity | $[m^2 s^{-1}]$ |
| $\rho$ | density | $[kgm^{-3}]$ |
| $\sigma \equiv \frac{k}{\varepsilon}\sqrt{(U_{i,j})^2} = \sqrt{s_{ll}^2 - \omega_{ll}^2}$ | shear parameter | $[-]$ |
| $\tilde{\sigma}$ | $\sigma$ in the calibration flow, e.g. $\tilde{\sigma} = 1/\sqrt{C_\mu}$ in the log law solution | $[-]$ |
| $\sigma_k, \sigma_\varepsilon$ | constants in transport model for $k$, eq. (2.63) | $[-]$ |
| $\sigma_i = [\sigma_u, \sigma_v, \sigma_w]$ | standard deviation of $U_i$ | $[ms^{-1}]$ |
| $\tau$ | rotor torque, eq. (5.2) | $[Nm]$ |
| $\Omega$ | rotational speed | $[\mathrm{rad}s^{-1}]$ |
| $\omega = \omega_{ij} \equiv \frac{1}{2}\frac{k}{\varepsilon}(U_{i,j} - U_{i,j})$ | normalized vorticity tensor | $[-]$ |

# CONTENTS

# 1

# INTRODUCTION

## 1.1 Motivation

A wind turbine produces electricity by extracting momentum from the atmospheric boundary layer (ABL), which creates a velocity deficit in the downstream flow. These deficits are better known as wind turbine wakes. When a wind turbine operates below rated power and it is positioned in the lee of another wind turbine, the velocity deficit of the upstream wind turbine can cause power losses to the downstream wind turbine. This phenomenon can cause annual energy losses in wind farms in the order of 10% to 20%.[6,24] The magnitude of these losses are mainly related to the inter spacing of wind turbines in a wind farm, and factors that influence the mixing of the wake with the undisturbed flow, e.g., atmospheric conditions and terrain features. Wind turbine wakes are also characterized by increased levels of turbulence, which can lead to early blade fatigue of a downstream wind turbine. It is therefore important to model the effects of wind turbine wakes in the early design phase of wind farms. Such a model should be able to give reliable and fast results that can be used to optimize a wind farm layout. A range of wake models exist that differ in computational effort and fidelity. Engineering models as the N.O. Jensen model[25] are fast but not always reliable.[21] Fuga[39] is a fast linearized computational fluid dynamics (CFD) method that has proven to provide reliable results of power deficits in wind farms, however; it cannot give information about wind turbine loads. In the last decades, the computational resources have increased, which allows more expensive nonlinear CFD methods as Reynolds-averaged Navier Stokes (RANS) and large-eddy simulation (LES) in particular, to be used for simulating wind turbine wakes. LES has proven to compare well with field measurements,[69] although the computational costs are high when it is applied to wind farms, because fine grids are necessary to resolve the wake turbulence, and long simulation times are required in order to capture time independent statistics from the transient simulation. RANS methods require roughly three orders of magnitude less computational resources than LES,[76] because RANS models all the turbulence, which allows coarser grids, and it is a steady state simulation, which avoids the necessity of long simulation times. Unfortunately, RANS methods are dependent on turbulence models, which have shown to dominate wind turbine wake simulations.[46] When the popular $k$-$\varepsilon$ eddy viscosity model (EVM) is employed, the near wake deficit of a single wind turbine is underpredicted, while the turbulence intensity is overpredicted.[10,16,45,46,76] Réthoré[46] argued that the underlying assumptions of the Boussinesq hypothesis (a linear stress-strain relation), which forms

the basis of the $k$-$\varepsilon$ EVM, are violated in the vicinity of a wind turbine. The goal of the present work is to develop a practical RANS-based turbulence model that can reliably predict the wind turbine wake flow.

## 1.2 Wind turbines wakes in the atmospheric boundary layer

A sketch of a wind turbine wake in the ABL is shown in Figure 1.1. When the wind approaches a wind turbine, it is slowed down under the presence of a high adverse pressure gradient. The blade forces create small vortex structures, which form larger root and tip vortices that are convected in a circular motion downstream. This flow region is known as the near wake, which is dictated by the thrust force. The blade loading forms a shear layer that grows in thickness further downstream. The shear layer is characterized by high velocity gradients, which create local flow regions that are far from being in equilibrium with the free-stream. The atmospheric turbulence destabilizes and breaks up the shear layer into smaller turbulence scales. At this point, turbulent diffusion processes dominate the wake recovery, a region that is referred as the far wake.

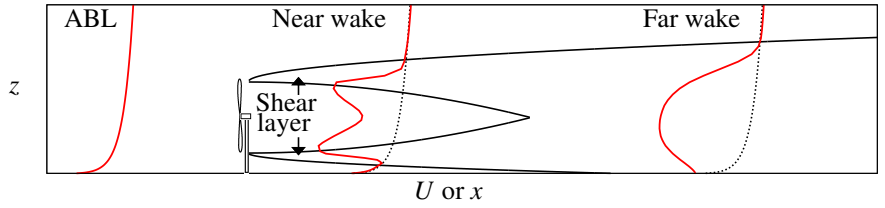


Figure 1.1: A sketch of a wind turbine wake in the ABL.

## 1.3 CFD modeling of wind turbine wakes

In the recent decades, CFD methods have become a popular tool to simulate wind turbine wakes. A brief introduction of these methods will be given here, while an extensive literate review can be found in the work of Sanderse et al.[54]

The representation of the wind turbine (rotor) in CFD can be carried out with different levels of model fidelity. In Figure 1.2, contours of constant vorticity are shown for three different wind turbine representations with corresponding CFD methods. The most left figure is a rotor where the blade geometry is fully gridded, and a detached-eddy simulation (DES) is used to model the blade turbulence and resolve the large scale turbulence in the wake. Not only the tip and root vortices are visible, but also the small

vortex structures that originate from the blade are present. This type of simulation has a high computational cost because a large number of cells is necessary to capture the blade turbulence, and a small time step is required to accurately resolve the blade turbulence in time. The actuator line method, shown in the middle of Figure 1.2 and first introduced by Sørensen and Shen,[61] is a computational less costly method because it does not represent the rotor geometry in the grid. Instead, each blade is modeled as a line, on which the blade force is applied, that is based on tabulated airfoil data and blade element momentum theory. The blade forces are added to the momentum Navier-Stokes equations as a sink term. The actuator line (AL) method does not resolve the blade turbulence, but the tip and root vortices are captured if the resolution of the loading and grid are sufficient. The method is transient and it is mostly applied in LES. A further reduction in computational effort can be achieved by representing the rotor as an actuator disk (AD), on which the rotor forces are also distributed over the azimuth.[37,46,48] The main advantage of the AD method over the AL method, is the fact that the AD method can be also used in a steady-state simulation, using RANS. Even though the flow fields of the AL method and the AD method in particular, are very different in the near wake compared to the fully gridded rotor, Troldborg et al.[73] showed that the three methods predict a very simlar wake flow at two rotor diameters downstream, as long as some inflow turbulence is present. Aubrun et al.[3] made similar conclusions using wind tunnel measurements of a scaled rotor model and a porous disk. This means that the use of ADs is justified if the wind turbine operates in the surface layer of the ABL, where there is always some level of ambient turbulence. Therefore, only the AD method is considered in the present work.

Fully gridded (DES) | Actuator line (LES) | Actuator disk (LES/RANS)

Figure 1.2: Contour of constant vorticity for different wind turbine representations in CFD. Figures prepared by P.-E. Réthoré.

The AD method can be combined with RANS (where all the turbulence is modeled) or LES (where the large scale turbulence is resolved and only the small scales are modeled). In an ideal world, where the turbulence is properly modeled in RANS,

it should provide the same flow field as an LES that is averaged in time, using an infinitely long data set. Unfortunately, turbulence models are often not accurate enough to have this property, and LES is mainly used for reasonably short simulation times because of limited computational resources. Nevertheless, one can still calibrate RANS based turbulence models against finite LES data, because LES compares well with field measurements of wind turbine wakes.[69]

## 1.4 Existing modifications of the $k$-$\varepsilon$ eddy viscosity model applied to wind turbine wakes

Modifications of the $k$-$\varepsilon$ EVM have been proposed and tested successfully for wind turbines wakes. El Kasmi and Masson[16] used an extra source term in the dissipation equation of the $k$-$\varepsilon$ EVM (originally proposed by Chen and Kim[12]), which is only active in the vicinity of the rotor. This source term includes a constant $C_{\varepsilon,4}$ that, together with the size of region where the source term is applied, determines the performance of the model. El Kasmi and Masson showed that the source term improves the velocity deficit for several cases compared with single wake measurements. Unfortunately, a thorough calibration of the source term is not published in the work of El Kasmi and Masson. Prospathopoulos et al.[45] and Réthoré[46] investigated the modified $k$-$\varepsilon$ EVM of El Kasmi and Masson, using different values of $C_{\varepsilon,4}$, while keeping the region of activity constant. Their work shows that the value of $C_{\varepsilon,4}$ is not general and needs to be adjusted for different single wind turbine wake cases. In addition, Prospathopoulos et al. showed that if the source term is calibrated to describe the velocity wake deficit at the far wake, it may not perform well in the near wake and vice versa. It should be noted that Prospathopoulos et al. and El Kasmi and Masson only compared the modified $k$-$\varepsilon$ EVM with measurements, not with LES, which can lead to an unfair comparison due to uncertainties in measurements. Cabezón et al.[10] investigated another modified $k$-$\varepsilon$ EVM, known as the realizable $k$-$\varepsilon$ EVM of Shih et al.[60] The model has a variable eddy viscosity coefficient ($C_\mu$) that is a complex scalar function of the local flow, i.e., a flow-dependent $C_\mu$, and it has a new transport equation for the dissipation rate. Cabezón et al. showed that the velocity deficit and the Reynolds-stresses (in some extent) predicted by the realizable $k$-$\varepsilon$ EVM compares better with those of LES and measurements, with respect to the standard $k$-$\varepsilon$ EVM. However, Cabezón et al. only considered one test case.

Réthoré[46] argued that the existing modifications of the $k$-$\varepsilon$ EVM, are not general enough for the wind turbine wake applications. Hence, there is a need for a more general turbulence model that is valid for a wide range of wake parameters, e.g., thrust coefficient, turbulence intensity, etc.

## 1.5 Present study

In the present work, alternative RANS-based turbulence models are applied to wind turbine wakes. These models range from complex nonlinear eddy viscosity models (NLEVMs), which have a nonlinear stress-strain relation and a variable eddy viscosity coefficient, up to a new $k$-$\varepsilon$ EVM with a simple modification, labeled as the $k$-$\varepsilon$-$f_P$ EVM. The $k$-$\varepsilon$-$f_P$ EVM is exactly the same as the standard $k$-$\varepsilon$ EVM, apart from a variable eddy viscosity coefficient that is an explicit function of the local flow.

This thesis is written as a collection of three journal articles, which can be found in Chapters 4-6. The papers should be treated as real chapters, not appendices. Prior to the journal article chapters, an introduction to turbulence modeling in RANS is presented in Chapter 2, where derivations and assumptions of $k$-$\varepsilon$-based turbulence models are discussed, using a hierarchy of model complexity. A number of NLEVMs are derived in Chapter 2, which are summarized in Appendix A, and their potential to simulate wind turbine wakes is discussed in Chapter 3. The problems of the NLEVMs are also addressed, which motivate us to develop a new, simpler turbulence model, namely the $k$-$\varepsilon$-$f_P$ EVM. In the three journal papers of Chapters 4-6, the $k$-$\varepsilon$-$f_P$ EVM is applied to single wakes, double wakes and wind farms, respectively. The journal papers are presented in unmodified form and can therefore have overlapping information. In the first paper, presented in Chapter 4, the $k$-$\varepsilon$-$f_P$ EVM is numerically verified using a grid dependency study. The $k$-$\varepsilon$-$f_P$ EVM is calibrated against LES and validated with field measurements, for 8 and 4 single wake cases, respectively. The performance of the $k$-$\varepsilon$-$f_P$ EVM for double wakes is tested in the second paper (Chapter 5), using LES. Since the force definition of interacting ADs is not trivial, a comparison of existing AD variable force methods is presented, and they are compared with a new proposed method that assures correct power and thrust predictions. In the third paper (Chapter 6), the $k$-$\varepsilon$-$f_P$ EVM and the new proposed AD variable force method are applied to three different wind farms, and a comparison with field measurements is given. This comparison is difficult because the measurements of the free-stream wind direction often contains a high uncertainty when the measurements are post-processed with narrow wind direction bins. Therefore, the uncertainty of wind direction measurements is quantified, and it is used to post-process the CFD results such that a fairer comparison can be made. In Chapter 7, the conclusions of all previous chapters are summarized, and a number of recommendations for further research are proposed. Finally, a number of guidelines for using the $k$-$\varepsilon$-$f_P$ EVM for CFD wake simulations are presented in Appendix B.

# 2

# TURBULENCE MODELING IN RANS

## 2.1 Introduction

The wake behind a wind turbine in the ABL is characterized by a high Reynolds number: $Re = U_{H,\infty} D/\nu \approx 10^7$, with $U_{H,\infty}$ as the free-stream velocity at hub height, $D$ as the rotor diameter and $\nu$ as the kinematic viscosity. Hence the flow is driven by turbulence rather than viscous processes. Assuming a constant density $\rho$, the incompressible Reynolds-averaged Navier-Stokes equations (RANS) can be employed:

$$\begin{aligned} &\text{Mass:} && \frac{\partial U_i}{\partial x_i} = 0, \\ &\text{Momentum:} && \frac{\bar{D}U_i}{\bar{D}t} = -\frac{1}{\rho}\frac{\partial P}{\partial x_i} + \frac{\partial}{\partial x_j}\left[\nu\left(\frac{\partial U_i}{\partial x_j} + \frac{\partial U_j}{\partial x_i}\right) - \overline{u_i' u_j'}\right], \end{aligned} \tag{2.1}$$

Here, $U_i$ are the three mean velocity components, $\bar{D}/\bar{D}t$ is the substantial derivative with respect to the mean velocity, $P$ is the mean pressure and $\overline{u_i' u_j'}$ are the Reynolds-stresses. Since the Reynolds number is high, the term with the kinematic viscosity is small and can be neglected. However, the viscous terms in the proceeding derivations are kept for generality. The derivation of the RANS equations is described in detail by Pope.[43] The RANS equations (2.1) contain ten variables, while only four equations are available. This problem is known as the turbulence clossure problem and it is has not been solved despite decades of research. In order to circumvent the problem, a wide range of turbulence models have been developed that add equations/relations for the Reynolds-stress and often introduce new flow variables that represent turbulence quantities.

In this chapter, RANS-based turbulence models are presented and derived, which are all related, as shown in a model hierarchy in Figure 2.1. The most complex model in Figure 2.1 is the differential Reynolds-stress model, which consists of six differential equations for the Reynolds-stress tensor, that are directly derived from the Navier-Stokes equations. In addition, two extra differential equations are used to model the turbulent kinetic energy $k$ and a dissipation variable, in this case $\varepsilon$. All other turbulence models in Figure 2.1 can be derived from the model that is one level higher in hierarchy. Thus, the model assumptions from parental models are directly inherrited by the models that are lower in the hierarchy. The simplest turbulence model in Figure 2.1 is the standard $k$-$\varepsilon$ eddy viscosity model. One could derive even simpler models, however, it is not expected that these models are applicable for single wind turbine wake simulations because the $k$-

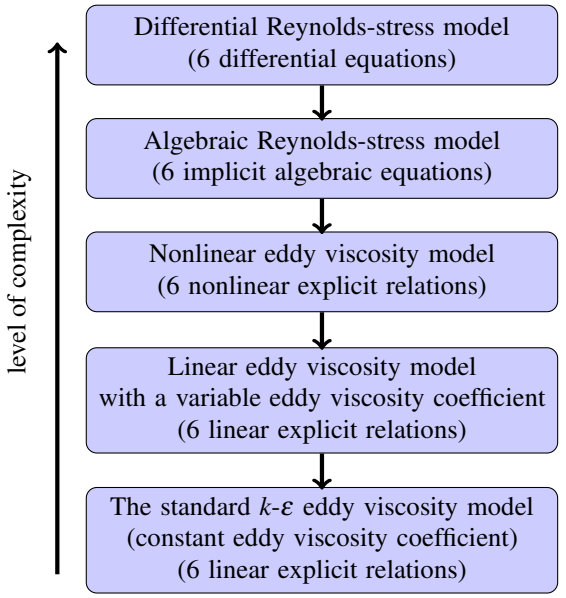


Figure 2.1: Turbulence model hierarchy in RANS: from a differential Reynolds-stress model to the standard $k$-$\varepsilon$ model. Note that all models have two extra differential equations, one for $k$ and one for $\varepsilon$.

$\varepsilon$ eddy viscosity model already fails to describe a wake. In the five proceeding sections, each turbulence model is derived and the corresponding assumptions are discussed.

## 2.2 The Reynolds-stress equations

The closure of the RANS equations (2.1) can be achieved by six transport equations for the six unknown Reynolds-stresses $\overline{u_i' u_j'}$, the so called Reynolds-stress equation(s). The traditional Reynolds-stress models (RSM) are based on this concept. Following Pope,[43] the Reynolds-stress equations are derived from substituting the transport equation of fluctuating velocity $u'$ (the remainder resulting from subtracting the Renolds-averaged momentum equation from the full momentum equation) into: $\overline{u_i' \frac{Du_j'}{Dt} + u_i' \frac{Du_j'}{Dt}}$, which leads

to:

$$\underbrace{\frac{\bar{D}\overline{u_i'u_j'}}{\bar{D}t}}_{\substack{\text{Change of Reynolds-stress}\\ \text{while moving with } U}} + \underbrace{\frac{\partial T_{kij}}{\partial x_k}}_{\text{transport}} = \underbrace{\mathscr{P}_{ij}}_{\text{production}} + \underbrace{\mathscr{R}_{ij}}_{\substack{\text{pressure-}\\ \text{redistribution}}} - \underbrace{\varepsilon_{ij}}_{\text{dissipation}}, \tag{2.2}$$

where $\bar{D}/\bar{D}t$ is the substantial derivative with respect to the mean velocity $U$. The transport tensor $T_{kij}$, the production tensor $\mathscr{P}_{ij}$, the pressure-redistribution tensor $\mathscr{R}_{ij}$ and the dissipation tensor $\varepsilon_{ij}$ are defined as:

$$T_{kij} \equiv \overline{u_i'u_j'u_k'} + \frac{1}{\rho}\overline{u_i'p'}\delta_{jk} + \frac{1}{\rho}\overline{u_j'p'}\delta_{ik} - \nu\frac{\partial\overline{u_i'u_j'}}{\partial x_k}, \tag{2.3}$$

$$\mathscr{P}_{ij} \equiv -\overline{u_i'u_k'}\frac{\partial U_j}{\partial x_k} - \overline{u_j'u_k'}\frac{\partial U_i}{\partial x_k}, \tag{2.4}$$

$$\mathscr{R}_{ij} \equiv \overline{\frac{p'}{\rho}\left(\frac{\partial u_i'}{\partial x_j} + \frac{\partial u_j'}{\partial x_i}\right)}, \tag{2.5}$$

$$\varepsilon_{ij} \equiv 2\nu\overline{\left(\frac{\partial u_i'}{\partial x_k}\frac{\partial u_j'}{\partial x_k}\right)}, \tag{2.6}$$

with $\rho$ as the density, $p'$ as the fluctuating pressure, $\nu$ as the kinematic viscosity and $\delta_{ij}$ as the Kronecker delta. The Reynolds-stress equation (2.2) can be approximated using models for the transport $T_{kij}$ and, more importantly, the pressure-redistribution term $\mathscr{R}_{ij}$, which is also known as the pressure-rate-of-strain tensor. In addition, it is common to assume isotropic dissipation, which is valid for high Reynolds numbers:[43]

$$\varepsilon_{ij} = \frac{2}{3}\varepsilon\delta_{ij}, \qquad \varepsilon = \frac{1}{2}\varepsilon_{ll} = \nu\overline{\left(\frac{\partial u_i'}{\partial x_j}\frac{\partial u_i'}{\partial x_j}\right)} \tag{2.7}$$

with $\varepsilon$ as the turbulent dissipation. In RANS, $\varepsilon$ is often modeled with a transport equation that is empirically derived. Taking half of the trace of the Reynolds-stress equation (2.2) leads to the transport equation for the turbulent kinetic energy $k \equiv \frac{1}{2}\overline{u_i'u_i'}$:

$$\frac{\bar{D}k}{\bar{D}t} + \frac{\partial}{\partial x_i}\left(\frac{1}{2}\overline{u_i'u_j'u_j'} + \overline{\frac{u_i'p'}{\rho}}\right) = -\nu\frac{\partial^2 k}{\partial x_i^2} + \mathscr{P} - \varepsilon, \tag{2.8}$$

with $\mathscr{P}$ as the production:

$$\mathscr{P} \equiv \frac{1}{2}\mathscr{P}_{ll} = -\overline{u_i'u_j'}\frac{\partial U_j}{\partial x_i}. \tag{2.9}$$

The pressure-rate-of-strain tensor $\mathscr{R}_{ij}$ does not appear in equation (2.8) because $\mathscr{R}_{ij}$ is deviatoric (trace is zero). In other words, $\mathscr{R}_{ij}$ does not contain turbulent kinetic energy, it only redistributes the magnitude of the invidual Reynolds-stress components. $\mathscr{R}_{ij}$ is therefore very important in flows that are characterized by anisotropic turbulence, e.g. a wind turbine wake.

## 2.3 Rodi's algebraic Reynolds-stress equation

Rodi[51] developed an algebraic RSM based on the assumption that the advection minus diffusion in the Reynolds-stress equation is proportional to the advection minus diffusion in the tranport equation of turbulent kinetic energy. Rodi's algebraic Reynolds-stress equation can be derived from the differential Reynolds-stress equation (2.2), in which the Reynolds-stress transport is neglected ($T_{ijk} = 0$) and isotropic turbulent dissipation is assumed using equation (2.7):

$$\frac{\bar{D}\overline{u_i'u_j'}}{\bar{D}t} = \mathscr{P}_{ij} + \mathscr{R}_{ij} - \frac{2}{3}\varepsilon\delta_{ij}, \tag{2.10}$$

Taking half of the trace of equation (2.10) leads to a simplified form of the turbulent kinetic energy equation (2.8):

$$\frac{\bar{D}k}{\bar{D}t} = \mathscr{P} - \varepsilon. \tag{2.11}$$

using equation (2.9). The Reynolds-stress tensor can be decomposed as:

$$\overline{u_i'u_j'} = k\frac{\overline{u_i'u_j'}}{k}. \tag{2.12}$$

Substituting the decomposition into the substantial derivative of the Reynolds-stress tensor of equation (2.10) leads to:

$$\frac{\bar{D}\overline{u_i'u_j'}}{\bar{D}t} = \frac{\bar{D}}{\bar{D}t}\left(k\frac{\overline{u_i'u_j'}}{k}\right) = \frac{\overline{u_i'u_j'}}{k}\frac{\bar{D}k}{\bar{D}t} + k\frac{\bar{D}}{\bar{D}t}\left(\frac{\overline{u_i'u_j'}}{k}\right) \approx \frac{\overline{u_i'u_j'}}{k}\frac{\bar{D}k}{\bar{D}t} = \frac{\overline{u_i'u_j'}}{k}\left(\mathscr{P} - \varepsilon\right), \tag{2.13}$$

where Rodi[51] makes an approximation in the second-to-last step by neglecting the temporal variation of the normalized Reynolds-stresses $\overline{u_i'u_j'}/k$ relative to $\bar{D}k/\bar{D}t$, which is called the weak-equilibrium assumption. This is equivalent to assume that the change of the normalized anisotropic Reynolds-stress is zero while moving with mean flow: $\bar{D}a_{ij}/\bar{D}t = 0$, where $a_{ij} \equiv \overline{u_i'u_j'}/k - \frac{2}{3}\delta_{ij}$. In the last step, the right hand side of equation (2.11) is inserted. As a result, the left hand side of the differential Reynolds-stress of equation (2.10) becomes algebraic and the full algebraic Reynolds-stress equation can be written as:

$$\frac{\overline{u_i'u_j'}}{k}\left(\mathscr{P} - \varepsilon\right) = \mathscr{P}_{ij} + \mathscr{R}_{ij} - \frac{2}{3}\varepsilon\delta_{ij}. \tag{2.14}$$

## 2.4 Nonlinear eddy viscosity models

An algebraic RSM is based on equation (2.14), in which a model for the pressure-rate-of-strain tensor $\mathscr{R}_{ij}$ is used. If the model for $\mathscr{R}_{ij}$ is linear in terms of the Reynolds-stress, the resulting implicit system of equations that defines the algebraic RSM can be solved analytically. These solutions are known as explicit algebraic RSMs or nonlinear eddy viscosity models (NLEVMs). When deriving an NLEVM, it is convenient to use the normalized anisotropic Reynolds-stress tensor $\mathbf{a}$, the normalized strain-rate tensor $\mathbf{s}$ and the normalized vorticity tensor $\boldsymbol{\omega}$:

$$\mathbf{a} = a_{ij} \equiv \frac{\overline{u_i' u_j'}}{k} - \frac{2}{3}\delta_{ij}, \quad \mathbf{s} = s_{ij} \equiv \frac{1}{2}\frac{k}{\varepsilon}\left(\frac{\partial U_i}{\partial x_j} + \frac{\partial U_j}{\partial x_i}\right), \quad \boldsymbol{\omega} = \omega_{ij} \equiv \frac{1}{2}\frac{k}{\varepsilon}\left(\frac{\partial U_i}{\partial x_j} - \frac{\partial U_j}{\partial x_i}\right). \tag{2.15}$$

Since the derivation of an NLEVM can become lengthy, a brief tensor notation is used for tensor multiplication, traces of multiple tensors and the Kronecker delta:

$$\mathbf{x} = x_{ij}, \qquad \mathbf{xy} = x_{ik}y_{kj}, \qquad \{\mathbf{xy}\} = x_{ij}y_{ji}, \qquad \delta_{ij} = \mathbf{I}. \tag{2.16}$$

A widely used model for $\mathscr{R}_{ij}$ is the model of Launder et al.:[30]

$$\mathscr{R}_{ij} = \mathscr{R}_{ij}^s + \mathscr{R}_{ij}^r, \tag{2.17}$$

which contains a slow part $\mathscr{R}_{ij}$ that represents Rotta's model[52] with $C_R$ as the Rotta constant:

$$\frac{\mathscr{R}_{ij}^s}{\varepsilon} = -C_R\mathbf{a}, \tag{2.18}$$

and a rapid part $\mathscr{R}_{ij}^r$, which exists for two model versions labeled as LRR-IP and LRR-QI:

$$\text{LRR-IP: } \frac{\mathscr{R}_{ij}^r}{\varepsilon} = \frac{4}{3}C_2\mathbf{s} + C_2\left(\mathbf{sa} + \mathbf{as} + \frac{2}{3}\{\mathbf{as}\}\mathbf{I}\right) + C_2(\boldsymbol{\omega}\mathbf{a} - \mathbf{a}\boldsymbol{\omega}), \tag{2.19}$$

$$C_R = 1.8, \qquad C_2 = 0.6,$$

$$\text{LRR-QI: } \frac{\mathscr{R}_{ij}^r}{\varepsilon} = \frac{4}{5}\mathbf{s} + \frac{9C_2+6}{11}\left(\mathbf{sa} + \mathbf{as} + \frac{2}{3}\{\mathbf{as}\}\mathbf{I}\right) - \frac{7C_2-10}{11}(\boldsymbol{\omega}\mathbf{a} - \mathbf{a}\boldsymbol{\omega}), \tag{2.20}$$

$$C_R = 1.5, \qquad C_2 = 0.4.$$

Subtituting $\mathscr{R}_{ij}$ of equation (2.17) into the algebraic Reynolds-stress equation (2.14) leads to:

$$\mathbf{a} = -\alpha\mathbf{s} - \beta\left(\mathbf{sa} + \mathbf{as} - \frac{2}{3}\{\mathbf{as}\}\mathbf{I}\right) + \gamma(\mathbf{a}\boldsymbol{\omega} - \boldsymbol{\omega}\mathbf{a}), \tag{2.21}$$

with parameters $\alpha$, $\beta$ and $\gamma$:

$$\text{LRR-IP: } \alpha = \frac{4}{3}(1-C_2)\,r, \qquad \beta = \gamma = (1-C_2)\,r, \tag{2.22}$$

$$\text{LRR-QI: } \alpha = \frac{8}{15}r, \qquad \beta = \frac{5-9C_2}{11}r, \qquad \gamma = \frac{7C_2+1}{11}r, \tag{2.23}$$

$$r \equiv \frac{1}{C_R + \mathscr{P}/\varepsilon - 1}. \tag{2.24}$$

Equation (2.21) is the basis for deriving explicit solutions for the anisotropic Reynolds-stress **a**, that are used as nonlinear stress-strain relations in the NLEVMs. We will derive general explicit solutions for **a**, by leaving $\alpha$, $\beta$ and $\gamma$ implicit. (Note this choice is not trivial because $\alpha$, $\beta$ and $\gamma$ are a function of **a**, since $\mathscr{P}/\varepsilon = -\{\mathbf{as}\}$, but is nevetherless widely adopted.[2,17,42,65]) There are two methods to derive these explicit solutions: an exact algebraic method - first introduced by Pope[42] for 2D flows and later adopted by Gatski and Speziale[17] for 3D flows - and an iterative method of Apsley and Leschziner,[2] which leads to approximative solutions. Both methods are individually presented in Sections 2.4.1 and 2.4.2, respectively. In Section 2.4.2 it will be shown that Pope's method and the iterative method of Apsley and Leschziner approach the same solution, if the iterative method of Apsley and Leschziner converges.

### 2.4.1 The algebraic method of Pope

Pope[42] recognized that the explicit solution for the anisotropic Reynolds-stress **a** can be constructed by ten tensorially independent tensor groups $T^{(\lambda)}$ for 3D flows:

$$\begin{array}{lcllcl}
\mathbf{T}^{(1)} &=& \mathbf{s}, & \mathbf{T}^{(6)} &=& \omega^2\mathbf{s} + \mathbf{s}\omega^2 - \frac{2}{3}\{\mathbf{s}\omega^2\}\mathbf{I}, \\
\mathbf{T}^{(2)} &=& \mathbf{s}\omega - \omega\mathbf{s}, & \mathbf{T}^{(7)} &=& \omega\mathbf{s}\omega^2 - \omega^2\mathbf{s}\omega, \\
\mathbf{T}^{(3)} &=& \mathbf{s}^2 - \frac{1}{3}\{\mathbf{s}^2\}\mathbf{I}, & \mathbf{T}^{(8)} &=& \mathbf{s}\omega\mathbf{s}^2 - \mathbf{s}^2\omega\mathbf{s}, \\
\mathbf{T}^{(4)} &=& \omega^2 - \frac{1}{3}\{\omega^2\}\mathbf{I}, & \mathbf{T}^{(9)} &=& \omega^2\mathbf{s}^2 + \mathbf{s}^2\omega^2 - \frac{2}{3}\{\omega^2\mathbf{s}^2\}\mathbf{I}, \\
\mathbf{T}^{(5)} &=& \omega\mathbf{s}^2 - \mathbf{s}^2\omega, & \mathbf{T}^{(10)} &=& \omega\mathbf{s}^2\omega^2 - \omega^2\mathbf{s}^2\omega,
\end{array} \tag{2.25}$$

where the explicit solution for **a** has the form:

$$\mathbf{a} = \sum_{\lambda=1}^{10} G^{(\lambda)}(\eta_i)\,\mathbf{T}^{(\lambda)}(\mathbf{s},\omega), \tag{2.26}$$

with $G^{(\lambda)}(\eta_i)$ as scalar functions of the invariants $\eta_i$ of the (incompressible) flow. The number of linear independent tensor groups is a finite because any other higher order tensor, e.q. $\omega\mathbf{s}^3\omega^2 - \omega^2\mathbf{s}^3\omega$, can be written as a linear combination of $T^{(\lambda)}$ employing the Cayley-Hamilton theorem.[42] In other words, a higher order tensor group will

break up into lower order tensors multiplied by invariants which are stored in the scalar functions $G^{(\lambda)}$. Five linear independent invariants exists:

$$\eta_1 = \{\mathbf{s}^2\},\ \eta_2 = \{\boldsymbol{\omega}^2\},\ \eta_3 = \{\mathbf{s}^3\},\ \eta_4 = \{\mathbf{s}\boldsymbol{\omega}^2\},\ \eta_5 = \{\mathbf{s}^2\boldsymbol{\omega}^2\}. \tag{2.27}$$

Due to the linear independence, all tensor groups $T^{(\lambda)}$ must share the properties of $\mathbf{a}$, hence, each $T^{(\lambda)}$ is a second order symmetric deviatoric tensor.

Pope[42] presented a procedure to derive an explicit solution of an implicit algebraic RSM of the form of equation (2.21), which is the basis of an NLEVM. Recognizing that the NLEVM has the form of equation (2.26) only the ten scalar functions $G^{(\lambda)}$ needs to be determined (in 3D). This can be achieved by leaving $\mathscr{P}/\varepsilon$ implicit in the coefficients $\alpha$, $\beta$ and $\gamma$ from equations (2.22) or (2.23). The scalar functions $G^{(\lambda)}$ are obtained from the linear system of equations:

$$A_{\gamma\lambda} G^{(\lambda)} = -\alpha\delta_{1\gamma}, \tag{2.28}$$

with

$$A_{\gamma\lambda} = \left(\delta_{\gamma\lambda} + \beta H_{\gamma\lambda} - \gamma J_{\gamma\lambda}\right), \tag{2.29}$$

where $J_{\gamma\lambda}$ and $H_{\gamma\lambda}$ are also scalar functions, which can be evaluated from:

$$\begin{aligned} H_{\lambda\gamma}\mathbf{T}^{(\gamma)} &= \mathbf{T}^{(\lambda)}\mathbf{s} + \mathbf{s}\mathbf{T}^{(\lambda)} - \frac{2}{3}\{\mathbf{s}\mathbf{T}^{(\lambda)}\}\mathbf{I}, \\ J_{\lambda\gamma}\mathbf{T}^{(\gamma)} &= \mathbf{T}^{(\lambda)}\boldsymbol{\omega} - \boldsymbol{\omega}\mathbf{T}^{(\lambda)}, \end{aligned} \tag{2.30}$$

using the Cayley-Hamilton theorem. As a result, matrix $A_{\gamma\lambda}$ becomes:

$$A_{\gamma\lambda} = \begin{bmatrix} 1 & \gamma\eta_2 & \frac{1}{3}\beta\eta_1 & -\frac{2}{3}\beta\eta_2 & 0 & \frac{2}{3}\beta\eta_4 & -\gamma\eta_2^2 & -2\gamma\eta_5 + \gamma\eta_1\eta_2 & -\frac{1}{3}\beta\eta_5 & 0 \\ -\gamma & 1 & 0 & 0 & -\frac{1}{2}\beta\eta_1 & -\frac{1}{2}\gamma\eta_2 & -\beta\eta_4 & \frac{1}{3}\beta\eta_3 & 0 & -\frac{1}{3}\beta\eta_5 - \frac{1}{6}\beta\eta_1\eta_2 \\ 2\beta & 0 & 1 & 0 & -\gamma\eta_2 & 2\beta\eta_2 & 0 & 2\gamma\eta_4 & \beta\eta_4 & -\gamma\eta_2^2 \\ 0 & 0 & 0 & 1 & -2\gamma\eta_1 & \beta\eta_1 & 2\gamma\eta_4 & 0 & \frac{1}{3}\beta\eta_3 & -2\gamma\eta_1\eta_2 + 2\gamma\eta_5 \\ 0 & -\beta & \gamma & 0 & 1 & 0 & \beta\eta_2 & 0 & \frac{1}{2}\gamma\eta_2 & \frac{2}{3}\beta\eta_4 \\ 0 & -3\gamma & 0 & \beta & 0 & 1 & 2\gamma\eta_2 & -\gamma\eta_1 & \frac{1}{2}\beta\eta_1 & 0 \\ 0 & 0 & 0 & 0 & 0 & \gamma & 1 & 0 & 0 & -\frac{1}{3}\beta\eta_1 \\ 0 & 0 & 0 & 0 & \beta & 0 & 0 & 1 & 0 & -\frac{1}{3}\beta\eta_2 \\ 0 & 0 & 0 & 0 & 3\gamma & -\beta & 0 & 0 & 1 & 2\gamma\eta_2 \\ 0 & 0 & 0 & 0 & 0 & 0 & -2\beta & 0 & \gamma & 1 \end{bmatrix} \tag{2.31}$$

Note that the subscript and superscript $\gamma$ is an index while $\gamma$ on its own is one of the coefficients of the algebraic RSM. Pope[42] derived an NLEVM for 2D flow only and argued that the solution for 3D flow is too cumbersome. In the 2D case, only the first three tensor groups from equation (2.25) and the first two invariants from equation (2.27) are nonzero. The full 3D explicit solution of the algebraic RSM equation (2.21) is derived by Gatski and Speziale[17] using software that can perform linear algebra to determine the inverse of $A_{\gamma\lambda}$. The resulting NLEVM is complex and it is given in Appendix A. In addition, the obtained scalar functions $G^{(\lambda)}$ can become singular. Gatski and Speziale proposed a method to regularize the singular $G^{(\lambda)}$ through a Padé approximation of the invariants, e.g.:

$$\{\omega^2\} \approx 1 - \frac{1}{1+\{\omega^2\}}, \tag{2.32}$$

which is only valid for $\{\omega^2\} << 1$. However, in the logarithmic region of simple shear flow $\{\omega^2\}$ is often much larger than one.

Taulbee[65] observed that $\beta$ is relatively small compared to $\alpha$ and $\gamma$ when the algebraic RSM from equation (2.14) is combined with the LRR-QI model of Launder[30] from equation (2.20), using the recommended constant $C_2 = 0.6$ belonging to the LRR-IP model from equation (2.19). In fact, when setting $C_2 = \frac{5}{9}$, $\beta$ will become zero and the algebraic RSM of equation (2.21) simplifies to:

$$\mathbf{a} = -\alpha\mathbf{s} + \gamma(\boldsymbol{\omega}\mathbf{a} - \mathbf{a}\boldsymbol{\omega}), \tag{2.33}$$

with parameters:

$$\alpha = \frac{8}{15}r, \qquad \gamma = \frac{4}{9}r. \tag{2.34}$$

However, when the recommended constant $C_2 = 0.4$ is used for the LRR-QI model, $\beta/\gamma = 1.4/3.8 \approx 0.37$, hence, the approximation of $\beta = 0$ used by Taulbee is quite demanding. In addition, the fact that $\beta$ is set to zero will result into an NLEVM that can only represent Reynolds-stress anisotropy for two normal components in simple shear flow:

$$\mathbf{a} = \begin{bmatrix} a_{11} & 0 & a_{13} \\ 0 & 0 & 0 \\ a_{13} & 0 & -a_{11} \end{bmatrix}, \tag{2.35}$$

where the first and third normal component are equal in magnitude but opposite in sign and the second normal component is zero. This means that the NLEVM can never replicate measurements or computations of simple shear flow with $a_{22} \neq 0$, e.g. results of direct numerical simulation of fully developed channel flow at low Reynolds numbers of Kim et al.[28]: $a_{11} = 0.333$, $a_{22} = -0.0707$ and $a_{33} = -0.263$ (for $y^+ \rightarrow$

$\infty$). In this case, the relative error in the normal components of $\mathbf{a}$, calculated by the NLEVM in simple shear flow, would be around 10% if the NLEVM is calibrated for $a_{11} = \frac{1}{2}(0.333 - 0.263) \approx 0.30$. Nevertheless, Taulbee derived a complex NLEVM from equation (2.33), which has been applied to a single wind turbine wake by Gómez-Elvira et al.[19] Wallin and Johansson[78] also derived an NLEVM based on the ideas of Taulbee, which is applicable to compressible rotational 3D flows. In addition, Wallin and Johansson derived an algebraic relation for $\mathscr{P}/\varepsilon$ for 2D flows, instead of leaving $\mathscr{P}/\varepsilon$ explicit, as done by Pope.[42] In the present work, an NLEVM with $\beta = 0$ is derived with the method of Pope, and it is given in Appendix A using the present notation. We will refer to this NLEVM as the quartic NLEVM of Taulbee, even though it is a simplified version of the orginal NLEVM of Taulbee.

### 2.4.2 The iterative method of Apsley and Leschziner

In Section 2.4.1, an NLEVM is algebraically derived using the method of Pope. Apsley and Leschziner[2] proposed an alternative procedure to derive an NLEVM from an algebraic RSM, which is based on a formal iteration routine. Writing the algebraic RSM of equation (2.21) in the form

$$\mathbf{a} = \mathbf{b} + f(\mathbf{a}), \tag{2.36}$$

with:

$$\mathbf{b} \equiv -\alpha\mathbf{s}, \qquad f(\mathbf{a}) \equiv -\beta\left(\mathbf{sa} + \mathbf{as} - \frac{2}{3}\{\mathbf{as}\}\mathbf{I}\right) + \gamma(\mathbf{a}\omega - \omega\mathbf{a}); \tag{2.37}$$

it is hypothesized that the explicit solution can be found by iterating equation (2.36) with:

$$\mathbf{a}^{(n)} = \mathbf{a}^{(1)} + f\left(\mathbf{a}^{(n-1)}\right), \qquad n = 2, 3..., \tag{2.38}$$

where the first solution $\mathbf{a}^{(1)}$ represents the stress-strain relation of a linear eddy viscosity model (EVM) $\mathbf{a}^{(1)} = -\alpha\mathbf{s}$ when setting $\alpha = 2C_\mu$, with $C_\mu$ as the eddy viscosity coefficient. Explicit solutions can be obtained by successive iteration, however, there is no guarantee of convergence. Nevertheless, Apsley and Leschziner used the technique to manually derive a quadratic NLEVM $\mathbf{a}^{(2)}$ and a cubic NLEVM $\mathbf{a}^{(3)}$, using the Cayley-Hamilton theorem.[42] The results are summarized in Appendix A.

Although not mentioned by Apsley and Leschziner,[2] the algebraic method of Pope can be used to obtain succesive NLEVMs with the iterative method of Apsley and Leschziner by performing simple matrix multiplications. Substituting the form of the solution of $\mathbf{a}$ from equation (2.26) at iteration step $n$:

$$\mathbf{a}^{(n)} = \sum_{\lambda=1}^{10} G_n^{(\lambda)}\mathbf{T}^{(\lambda)} = G_n^{(\lambda)}\mathbf{T}^{(\lambda)}, \tag{2.39}$$

(where summation over index $\lambda$ is performed) into the proposed iteration procedure of Apsley and Leschziner of equation (2.38) gives:

$$G_{n+1}^{(\gamma)}\mathbf{T}^{(\gamma)} = -\alpha\delta_{1\gamma}\mathbf{T}^{(\gamma)} + f\left(G_n^{(\lambda)}\mathbf{T}^{(\lambda)}\right), \qquad n = 1,2,3..., \tag{2.40}$$

where the initital solution: $\mathbf{a}^{(1)} = -\alpha\delta_{1\gamma}\mathbf{T}^{(\gamma)}$ is used in accordance with equation (2.28). Hence,

$$\begin{aligned} G_{n+1}^{(\gamma)}\mathbf{T}^{(\gamma)} &= -\alpha\delta_{1\gamma}\mathbf{T}^{(\gamma)} - \beta\left(\mathbf{s}G_n^{(\lambda)}\mathbf{T}^{(\lambda)} + G_n^{(\lambda)}\mathbf{T}^{(\lambda)}\mathbf{s} - \frac{2}{3}\{G_n^{(\lambda)}\mathbf{T}^{(\lambda)}\mathbf{s}\}\mathbf{I}\right) \\ &\quad + \gamma G_n^{(\lambda)}\left(\mathbf{T}^{(\lambda)}\boldsymbol{\omega} - \boldsymbol{\omega}\mathbf{T}^{(\lambda)}\right), \\ &= -\alpha\delta_{1\gamma}\mathbf{T}^{(\gamma)} - G_n^{(\lambda)}\left(\beta H_{\lambda\gamma}\mathbf{T}^{(\gamma)} - \gamma J_{\lambda\gamma}\mathbf{T}^{(\gamma)}\right). \end{aligned} \tag{2.41}$$

Cancelling $\mathbf{T}^{(\gamma)}$ and further rewriting using equation (2.29) gives:

$$\begin{aligned} G_{n+1}^{(\gamma)} &= -\alpha\delta_{1\lambda} - \left(\beta H_{\gamma\lambda} - \gamma J_{\gamma\lambda}\right) G_n^{(\gamma)}, \\ &= -\alpha\delta_{1\lambda} - \left(A_{\gamma\lambda} - \delta_{\gamma\lambda}\right) G_n^{(\gamma)}. \end{aligned} \tag{2.42}$$

Since $A_{\gamma\lambda}$ is determined by Gatski and Speziale in 3D (equation (2.31)), the solution for $G_{n+1}$ is easily obtained, using the inital solution $G_1^{(\gamma)} = -\alpha\delta_{1\gamma}$. To investigate convergence, one could write equation (2.42) as:

$$\mathbf{x}_{n+1} = \mathbf{x}_1 + \mathbf{A}\mathbf{x}_n, \tag{2.43}$$

with:

$$\mathbf{x}_n \equiv G_n^{(\gamma)}, \qquad \mathbf{x}_1 \equiv -\alpha\delta_{1\lambda}, \qquad \mathbf{A} \equiv -\left(\beta H_{\gamma\lambda} - \gamma J_{\gamma\lambda}\right) = \delta_{\gamma\lambda} - A_{\gamma\lambda}, \tag{2.44}$$

from which it follows that:

$$\mathbf{x}_{n+1} = \left(\mathbf{I} + \mathbf{A} + \mathbf{A}^2 + ... + \mathbf{A}^{n-1} + \mathbf{A}^n\right)\mathbf{x}_1 \qquad \Rightarrow \mathbf{x}_{n+1} - \mathbf{x}_n = \mathbf{A}^n\mathbf{x}_1. \tag{2.45}$$

The iteration procedure converges if the difference between successive realizations $\mathbf{x}_{n+1} - \mathbf{x}_n$ goes to zero for large $n$:

$$\lim_{n\to\infty} \mathbf{x}_{n+1} - \mathbf{x}_n = 0. \tag{2.46}$$

Thus, the iteration procedure converges if:

$$\max\left(\mathrm{abs}\left(\lambda_i\right)\right) < 1, \tag{2.47}$$

where $\lambda_i$ are the eigenvalues of $\mathbf{A}$. Unfortunately, proofing this convergence in 3D flows is impossible because a 10th order characteristic polynomial needs to be solved to obtain the eigenvalues of $\mathbf{A}$. If the iteration procedure converges the solution converges to:

$$\lim_{n\to\infty} \mathbf{x}_n = -\left(\mathbf{A}-\mathbf{I}\right)^{-1}\mathbf{x}_1, \tag{2.48}$$

which is found by substitution of equation (2.43) into equation (2.46). Equation (2.48) can be written in the notation of Pope's method using equation (2.44):

$$\lim_{n\to\infty} G_n^{(\lambda)} = -\alpha\delta_{1\lambda}A^{-1}_{\gamma\lambda}, \tag{2.49}$$

which is exactly the result that Gatski and Speziale found by using Pope's method of equation (2.28) for 3D flow. Thus the algebraic method of Pope and the formal iteration procedure of Apsley and Leschziner give the same result for large $n$ IF the formal iteration procedure converges.

### 2.4.3 Calibration

The derived NLEVMs, listed in Appendix A, are completely defined by the orignal coefficients from equations (2.22) and (2.23), and do not need calibration. However, the derivations of the NLEVMs are carried out from an algebraic RSM, in which wall reflections are not present. Therefore, if the NLEVMs are used for wall-bounded flows, a calibration of $\alpha,\beta$ and $\gamma$ is justified. In addition, except for the full NLEVM of Gatski and Speziale, the other NLEVMs are approximate solutions that need calibration. In the current work, the NLEVMs are calibrated using the procedure described by Apsley and Leschziner,[2] where $\alpha,\beta$ and $\gamma$ are determined from a basic simple shear flow with anisotropic Reynolds-stress $\tilde{\mathbf{a}}$:

$$\tilde{\mathbf{a}} = \begin{bmatrix} \tilde{a}_{11} & 0 & \tilde{a}_{13} \\ 0 & -\tilde{a}_{11}-\tilde{a}_{33} & 0 \\ \tilde{a}_{13} & 0 & \tilde{a}_{33} \end{bmatrix}. \tag{2.50}$$

Note that the tilde symbol is used for the flow variables that correspond to the calibration flow. When defining $x$ as the streamwise coordinate and $z$ as the normal coordinate with respect to the wall, the only non zero velocity gradient is $\partial U/\partial z$. In this case, the normalized strain and vorticity tensors are equal to:

$$\mathbf{s} = \frac{1}{2}\tilde{\sigma}\begin{bmatrix} 0&0&1 \\ 0&0&0 \\ 1&0&0 \end{bmatrix},\ \boldsymbol{\omega} = \frac{1}{2}\tilde{\sigma}\begin{bmatrix} 0&0&1 \\ 0&0&0 \\ -1&0&0 \end{bmatrix}, \tag{2.51}$$

with $\tilde{\sigma}$ as the shear parameter belonging to the flow for which the calibration is carried out: $\tilde{\sigma} = \frac{k}{\varepsilon}\frac{\partial U}{\partial z}$. In the calibration of the NLEVMs, the tensor groups as defined by Apsley

and Leschziner[2] are applied because they lead to a simpler set of equations:

$$\begin{array}{lcllcl} \mathbf{T}^{(1)} & = & \mathbf{s}, & \mathbf{T}^{(6)} & = & \boldsymbol{\omega}^2\mathbf{s}+\mathbf{s}\boldsymbol{\omega}^2-\{\boldsymbol{\omega}\}\mathbf{s}-\frac{2}{3}\{\mathbf{s}\boldsymbol{\omega}^2\}\mathbf{I}, \\ \mathbf{T}^{(2)} & = & \boldsymbol{\omega}\mathbf{s}-\mathbf{s}\boldsymbol{\omega}, & \mathbf{T}^{(7)} & = & \boldsymbol{\omega}\mathbf{s}\boldsymbol{\omega}^2-\boldsymbol{\omega}^2\mathbf{s}\boldsymbol{\omega}, \\ \mathbf{T}^{(3)} & = & \mathbf{s}^2-\frac{1}{3}\{\mathbf{s}^2\}\mathbf{I}, & \mathbf{T}^{(8)} & = & \mathbf{s}\boldsymbol{\omega}\mathbf{s}^2-\mathbf{s}^2\boldsymbol{\omega}\mathbf{s}, \\ \mathbf{T}^{(4)} & = & \boldsymbol{\omega}^2-\frac{1}{3}\{\boldsymbol{\omega}^2\}\mathbf{I}, & \mathbf{T}^{(9)} & = & \boldsymbol{\omega}^2\mathbf{s}^2+\mathbf{s}^2\boldsymbol{\omega}^2-\frac{2}{3}\{\boldsymbol{\omega}^2\mathbf{s}^2\}\mathbf{I}, \\ \mathbf{T}^{(5)} & = & \boldsymbol{\omega}\mathbf{s}^2-\mathbf{s}^2\boldsymbol{\omega}, & \mathbf{T}^{(10)} & = & \boldsymbol{\omega}\mathbf{s}^2\boldsymbol{\omega}^2,-\boldsymbol{\omega}^2\mathbf{s}^2\boldsymbol{\omega}, \end{array} \tag{2.52}$$

where $\mathbf{T}^{(2)}$ and $\mathbf{T}^{(6)}$ are different from the original tensor groups as defined by Pope in equation (2.25). Note, that these changes do not lead to different NLEVMs because $\mathbf{T}^{(2)}$ and $\mathbf{T}^{(6)}$ of Apsley and Leschziner are linear dependent on the original tensor groups of Pope. The non-zero tensor groups in the calibration flow are found by substitution of the strain and the vorticity tensor in equation (2.52):

$$\mathbf{T}^{(1)}=\frac{1}{2}\tilde{\sigma}\begin{bmatrix}0&0&1\\0&0&0\\1&0&0\end{bmatrix}, \quad \mathbf{T}^{(2)}=\frac{4}{\tilde{\sigma}^2}\mathbf{T}^{(7)}=\frac{4}{\tilde{\sigma}^2}\mathbf{T}^{(8)}=\frac{1}{2}\tilde{\sigma}^2\begin{bmatrix}-1&0&0\\0&0&0\\0&0&1\end{bmatrix}, \tag{2.53}$$

$$\mathbf{T}^{(3)}=-\mathbf{T}^{(4)}=-\frac{2}{\tilde{\sigma}^2}\mathbf{T}^{(9)}=\frac{1}{12}\tilde{\sigma}^2\begin{bmatrix}1&0&0\\0&-2&0\\0&0&1\end{bmatrix}.$$

Note that the original definition of $\mathbf{T}^{(6)}$ from equation (2.25) would have non zero components $\mathbf{T}^{(6)}_{13}$ and $\mathbf{T}^{(6)}_{31}$, making the calibration slightly more complicated. From the five invariants of equation (2.27) only three are not zero in the simple shear flow:

$$\eta_1=\{\mathbf{s}^2\}=\frac{1}{2}\tilde{\sigma}^2,\ \eta_2=\{\boldsymbol{\omega}^2\}=-\frac{1}{2}\tilde{\sigma}^2,\ \eta_5=\{\mathbf{s}^2\boldsymbol{\omega}^2\}=-\frac{1}{8}\tilde{\sigma}^4. \tag{2.54}$$

The parameters $\alpha,\beta$ and $\gamma$ for a particular NLEVM are found by substitution of the corresponding scalar coefficients of Tables A.1 and A.2 (including the invariants of equation (2.54)) and the tensor groups in simple shear flow from equation (2.53) into:

$$\tilde{\mathbf{a}}=\begin{bmatrix}\tilde{a}_{11}&0&\tilde{a}_{13}\\0&-\tilde{a}_{11}-\tilde{a}_{33}&0\\\tilde{a}_{13}&0&\tilde{a}_{33}\end{bmatrix}=\sum_{\lambda=1}^{10}G^{(\lambda)}(\eta_i)\,\mathbf{T}^{(\lambda)}(\mathbf{s},\boldsymbol{\omega}). \tag{2.55}$$

The resulting system of equations has three linearly independent equations from which $\alpha,\beta$ and $\gamma$ can be determined. Note that for the NLEVM of Taulbee, in which $\beta=0$, only two linearly independent equations exist. Gómez-Elvira[19] has calibrated the complete NLEVM of Taulbee, which includes extra relations and calibration parameters. Although not mentioned by Gómez-Elvira,[19] this calibration leads to an under-determined linear system of calibration equations, in which one of the constants is a free parameter. In addition, the given calibration results presented in the work of Gómez-Elvira[19] do not

reflect the intended calibration flow, although the actual implemented set of constants does.[14] The simplified NLEVM of Taulbee (as used in the present work and defined in Appendix A) only has two calibration parameters ($\alpha$ and $\beta$), which leads to a closed system of calibration equations. The results of the calibration of the NLEVMs of Apsley and Leschziner and the simplified NLEVM of Taulbee, are listed in Tables A.3 and A.4, respectively.

### 2.4.4 Boundedness

Apsley and Leschziner[2] constrained the scalar coefficent $G^{(\lambda)}$ of their cubic NLEVM by multiplying $\alpha, \beta$ and $\gamma$ with a limiter function $f_P$, such that $G^{(\lambda)}$ cannot grow to infinity:

$$\alpha' = f_P \alpha, \qquad \beta' = f_P \beta, \qquad \gamma' = f_P \gamma, \tag{2.56}$$

with $f_P$ defined as:

$$f_P = \frac{C_R + \widetilde{\mathscr{P}/\varepsilon} - 1}{C_R + \mathscr{P}/\varepsilon - 1}, \tag{2.57}$$

where $\widetilde{\mathscr{P}/\varepsilon}$ is the ratio of turbulent production and turbulent dissipation in the simple shear flow, which is equal to one. The denominator of $f_P$ is based on the orginal denominator of $\alpha, \beta$ and $\gamma$ of the pressure-strain models of Launder et al.[30] (equations (2.22) and (2.23)). Apsley and Leschziner found that the direct use of equation (2.57) leads to numerically unstable behavior and proposed to approximate $\mathscr{P}/\varepsilon \approx f_P C_\mu \sigma^2$, which leads to the solution:

$$f_P(\sigma/\tilde{\sigma}) = \frac{2 f_0}{1 + \sqrt{1 + 4 f_0 (f_0 - 1) \left(\frac{\sigma}{\tilde{\sigma}}\right)^2}}, \qquad f_0 = \frac{C_R}{C_R - 1}, \tag{2.58}$$

Except for $G^{(4)}$, all scalar functions $G^{(\lambda)}$ of the quartic NLEVM of Taulbee[65] are all bounded by the invariant $\eta_2$ in the denominator:

$$\begin{aligned} &\lim_{\eta_2 \to 0} G^{(1)} = -\alpha, \qquad \lim_{\eta_2 \to 0} G^{(2)} = \alpha\gamma, \qquad \lim_{\eta_2 \to 0} G^{(6)} = -3\alpha\gamma^2, \\ &\lim_{\eta_2 \to 0} G^{(7)} = 3\alpha\gamma^3, \qquad \lim_{\eta_2 \to -\infty} G^{(1,2,6,7)} = 0. \end{aligned} \tag{2.59}$$

The boundedness of the scalar function $G^{(4)}$ is not obvious since it has the invariant $\eta_4$ in the numerator, which could hypothetically grow faster than its denominator. $\eta_4 = \{\mathbf{s}\boldsymbol{\omega}^2\}$ is a function of all nine velocity derivatives $U_{i,j}$, however, $\eta_2 = \{\boldsymbol{\omega}^2\}$ is only a function of the off-diagonal velocity derivatives. As a result, the derivatives $U_{\alpha,\alpha}$, present in the numerator of $G^{(4)}$, are not bounded by the denominator. When the quartic NLEVM is applied to a flow around a wind turbine, the streamwise derivative $\partial U/\partial x$ is large in vicinity of the rotor, which might cause unstable behavior of the NLEVM, because of $G^{(4)}$.

## 2.5 Linear eddy viscosity models

### 2.5.1 The standard $k$-$\varepsilon$ EVM

In the standard $k$-$\varepsilon$ EVM, the deviatoric Reynolds-stress is defined by the Boussinesq approximation:[9]

$$\overline{u_i' u_j'} - \frac{2}{3} k \delta_{ij} = -\nu_T \left( \frac{\partial U_i}{\partial x_j} + \frac{\partial U_j}{\partial x_i} \right), \tag{2.60}$$

which can also be written in terms of the normalized anisotropic Reynolds-stress $\mathbf{a}$ from equation (2.15):

$$\mathbf{a} = -2C_\mu \mathbf{s}, \tag{2.61}$$

with $C_\mu$ as a constant eddy viscosity coefficient that is used to define the kinematic eddy viscosity $\nu_T$:

$$\nu_T = C_\mu \frac{k^2}{\varepsilon}. \tag{2.62}$$

Hence the $k$-$\varepsilon$ EVM has a linear stress-strain relation and can therefore only model isotropic turbulence. The turbulent kinetic energy $k$ and the turbulent dissipation $\varepsilon$ are modeled through two transport equations:

$$\begin{aligned} \frac{Dk}{Dt} &= \nabla \cdot \left[ \left( \nu + \frac{\nu_T}{\sigma_k} \right) \nabla k \right] + \mathscr{P} - \varepsilon, \\ \frac{D\varepsilon}{Dt} &= \nabla \cdot \left[ \left( \nu + \frac{\nu_T}{\sigma_\varepsilon} \right) \nabla \varepsilon \right] + \left( C_{\varepsilon,1} \mathscr{P} - C_{\varepsilon,2} \varepsilon \right) \frac{\varepsilon}{k}, \end{aligned} \tag{2.63}$$

where $\nu$ is the kinematic molecular viscosity, the turbulent production $\mathscr{P}$ and dissipation $\varepsilon$ are defined in equations (2.9) and (2.7), and $C_{\varepsilon,1}, C_{\varepsilon,2}$, $\sigma_k$, $\sigma_\varepsilon$ are constants. The transport equation for $k$ is directly related to the trace of the Reynolds-stress equations, as shown by equation (2.8). An exact transport equation for turbulent dissipation $\varepsilon$ can be derived, although it is not practical to use as a model equation because it is not closed.[43] The equation for $\varepsilon$ in equation (2.63) is therefore assembled empirically.

### 2.5.2 A variable eddy viscosity coefficient

In the general notation of the NLEVMs of equation (2.26), the standard $k$-$\varepsilon$ EVM has only one non-zero scalar coefficient: $G^{(1)} = -2C_\mu$, which is constant. In Section 2.4, five NLEVMs are derived and the results are summarized in Appendix A. If one would neglect the nonlinear terms in the stress-strain relation of the NLEVMs, i.e. $G^{(2-10)} = 0$

in equation (2.26), the anisotropic Reynolds-stress of the five NLEVMs reduce to form of the standard $k$-$\varepsilon$ EVM:

$$\mathbf{a} = G^{(1)}\mathbf{s} + \sum_{\lambda=2}^{10} G^{(\lambda)}(\eta_i)\mathbf{T}^{(\lambda)}(\mathbf{s},\boldsymbol{\omega}), \tag{2.64}$$

with the scalar coefficient $G^{(1)}$ as listed in Table A.1. Since $G^{(1)}$ is variable in all NLEVMs it implies that $C_\mu$ should also be variable. Note that in the NLEVMs of Apsley and Leschziner $\alpha$, $\beta$ and $\gamma$ are multiplied by the scalar function $f_P$ from equation (2.58), hence the linear ($n=1$) and quadratic solution ($n=2$) also include a variable $G^{(1)}$. The variable $C_\mu$, labeled as $C_\mu^*$, is defined as:

$$C_\mu^* = -\frac{1}{2}G^{(1)}, \tag{2.65}$$

and it is listed in Table 2.1 for each NLEVM.

Table 2.1: $C_\mu^*$ in NLEVMs. $Q$ and $R$ are defined in equations (A.3) and (A.4), respectively.

| | $C_\mu^*$ |
|---|---|
| method of Apsley and Leschziner | |
| $n=1$ | $\frac{1}{2}\alpha f_P$ |
| $n=2$ | $\frac{1}{2}\alpha f_P$ |
| $n=3$ | $\frac{1}{2}\alpha f_P\left(1+\frac{2}{3}\beta^2 f_P^2\eta_1+2\gamma^2 f_P^2\eta_2\right)$ |
| $n=4$ | $\frac{1}{2}\alpha f_P\left(1+\frac{2}{3}\beta^2 f_P^2\eta_1+2\gamma^2 f_P^2\eta_2-2\beta\gamma^2 f_P^3\eta_4\right)$ |
| method of Pope | |
| ($\beta=0$) | $\frac{1}{2}\alpha\left(1-\frac{1}{2}\eta_2\gamma^2\right)Q$ |
| full NLEVM | $\frac{1}{2}\alpha\left(1-\frac{1}{2}\beta^2\eta_1-\frac{1}{2}\gamma^2\eta_2-\frac{1}{3}\beta^3\eta_3+5\beta\gamma^2\eta_4\right)R$ |

The need for a variable $C_\mu^*$ can be further motivated from realizability arguments, as shown by Pope.[43] A proper turbulence model should have the following properties for the Reynolds-stress $\overline{u_i'u_j'}$:

$$\overline{u_i'u_j'}\delta_{ij} > 0, \tag{2.66}$$

$$\|\overline{u_\alpha'u_\beta'}\|^2 \leq \overline{u_\alpha'u_\alpha'}\;\overline{u_\beta'u_\beta'}, \tag{2.67}$$

where summation is not performed over greek indices. Equation (2.66) means that the normal Reynolds-stress should always be positive and equation (2.67) is a form of the Cauchy-Schwartz inequality. In a simple shear flow, as defined in equations (2.51) and (2.50), the only non-zero off-diagonal Reynolds-stress $\|\overline{u'w'}\|$ in the standard $k$-$\varepsilon$ EVM

becomes:

$$\left.\begin{array}{c} \|\overline{u'w'}\| = \nu_T \frac{\partial U}{\partial z} = C_\mu \frac{k^2}{\varepsilon} \frac{\partial U}{\partial z} \\ \mathscr{P} = \|\overline{u'w'}\| \frac{\partial U}{\partial z} \end{array}\right\} \Rightarrow \|\overline{u'w'}\|^2 = k^2 C_\mu \mathscr{P}/\varepsilon. \tag{2.68}$$

The normal Reynolds-stresses are equal to $\overline{u'_\alpha u'_\alpha} = 2/3k$, hence the Cauchy-Schwartz inequality in simple shear flow for the standard $k$-$\varepsilon$ EVM reads:

$$C_\mu \leq \frac{4/9}{\mathscr{P}/\varepsilon}. \tag{2.69}$$

For $\mathscr{P}/\varepsilon \gg 1$, $C_\mu$ needs to be lowered in order to avoid violating the Cauchy-Schwartz inequality and producing non-realizable Reynolds-stresses. Thus, $C_\mu$ cannot be a constant for flows with a high shear, which are characterized by $\mathscr{P}/\varepsilon >> 1$, e.g. the shear layer in the near wind turbine wake.

### 2.5.3 The $k$-$\varepsilon$-$f_P$ EVM

The simplest $k$-$\varepsilon$ EVM with a variable $C^*_\mu$ from Table 2.1 is:

$$C^*_\mu = \frac{1}{2}\alpha f_P = -\frac{\tilde{a}_{13}}{\tilde{\sigma}} f_P, \tag{2.70}$$

where $\alpha = -2\tilde{a}_{13}/\tilde{\sigma}$ is defined by calibration with a simple shear flow (Table A.3). This new $k$-$\varepsilon$ EVM is labeled as the $k$-$\varepsilon$-$f_P$ EVM, and it is further explained in Chapter 4. The $k$-$\varepsilon$-$f_P$ EVM is a simple modification of the standard $k$-$\varepsilon$ EVM because one does not need to solve extra equations ($f_P$ is only an explicit function of local flow variables) or include additional boundary conditions. The influence of the variable $C^*_\mu$ on a wind turbine simulation is large, which is shown in Chapter 3, and it is used to improve the velocity deficit prediction of the standard $k$-$\varepsilon$ EVM in Chapters 4, 5 and 6, for single, double and multi wind turbine wakes, respectively.

## 2.6 Conclusions

A range of RANS-based turbulence models has been derived and the governing assumptions are discussed. The turbulence models can be written in an hierarchal order, first introduced in Figure 2.1 and also shown in Figure 2.2, where the individual assumptions per model are illustrated. The differential RSM is the most complex turbulence model in the given hierarchy from which the simpler models can be derived. It is important to realize that a simpler model inherits the assumption made by their parental models. The differential RSM is based on six differential equations for the Reynolds-stress that are directly derived from the Navier-Stokes equations. When the transport of Reynolds-stress

is neglected, isotropic dissipation is assumed and Rodi's weak equilibrium assumption is employed, the differential equations can be simplified to a set of six implicit algebraic equations. The pressure-rate-of-tensor needs to be modeled and if the chosen model is linear in terms of Reynolds-stress, explicit solutions of the 6 implicit algebraic equations can be derived, which are the basis of NLEVMs. One analytic and one iterative method are used to derive five NLEVMs. The NLEVMs can model anisotropic turbulence, and they have a variable eddy viscosity coefficient ${}^*C_\mu$. When the nonlinear terms are disregarded, an isotropic $k$-$\varepsilon$ EVM with a variable $C_\mu^*$ is obtained. Finally, the standard $k$-$\varepsilon$ EVM appears when $C_\mu^*$ is assumed to be constant: $C_\mu^* = C_\mu$. However, if the standard $k$-$\varepsilon$ EVM is applied to a flow that is far from equilibrium, i.e., $\mathscr{P}/\varepsilon >> 1$, $C_\mu^*$ must be inversely proportional with $\mathscr{P}/\varepsilon$ in order to remain realizable, and the assumption of a constant $C_\mu$ is violated. This indicates why the standard $k$-$\varepsilon$ EVM cannot predict the highly non-equilibrium flow in the near vicinity of a wind turbine.

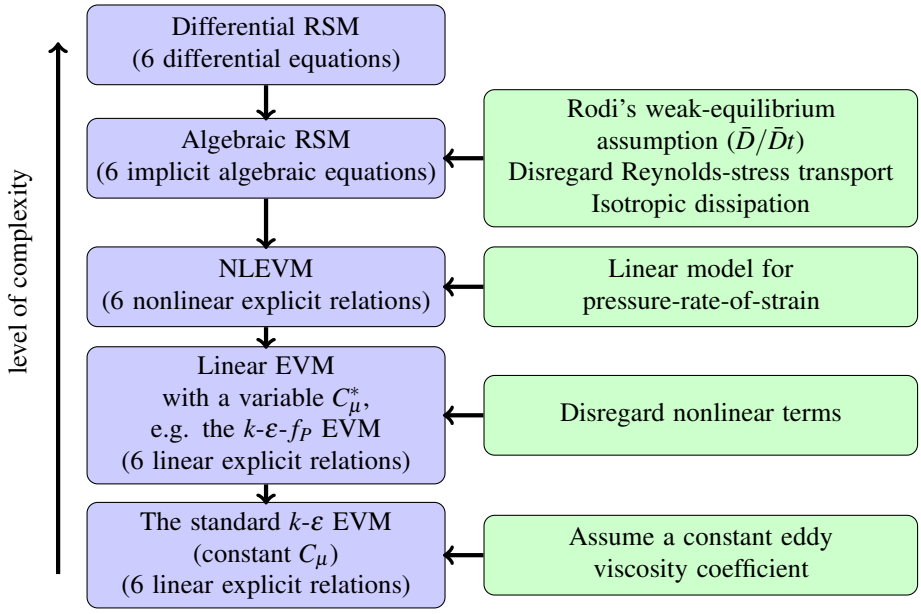


Figure 2.2: Turbulence model hierarchy in RANS continued: from a differential RSM to the standard $k$-$\varepsilon$ EVM. Blue boxes are models and green boxes are assumptions. Note that all models have two extra differential equations, one for $k$ and one for $\varepsilon$.

# 3

# THE POTENTIAL AND PROBLEMS OF NONLINEAR EDDY VISCOSITY MODELS APPLIED TO A WIND TURBINE WAKE IN ATMOSPHERIC TURBULENCE

## 3.1 Introduction

In Chapter 2, a range of RANS-based turbulence models is derived. It has been shown that a complex differential Reynolds-stress model (RSM), in which each individual Reynolds component is modeled with a differential transport equation, can be simplified to an eddy viscosity model (EVM) with a nonlinear stress-strain relation. These so called nonlinear eddy viscosity models (NLEVMs), can account for anisotropic Reynolds-stresses. Since the turbulence in the wind turbine wake and the ABL is anisotropic, as shown in Chapter 1, the NLEVMs are potentially more suited to model a wind turbine wake in an ABL compared to the standard (isotropic) $k$-$\varepsilon$ EVM. In addition, the NLEVMs have a variable eddy viscosity coefficient $C_\mu^*$, which can be beneficial for flows that are far from it's equilibrium, e.g., the high gradients in pressure and velocity, in the vicinity of a wind turbine. In this Chapter, the NLEVMs of Apsley and Leschziner[2] and a simplified version of the NLEVM of Taulbee[65] are applied to an ABL, with and without a single wind turbine wake. The methodology is presented in Section 3.2. In Section 3.3, the results of the NLEVMs are compared with LES, the standard $k$-$\varepsilon$ EVM and a new modified $k$-$\varepsilon$ EVM with a variable $C_\mu^*$, called the $k$-$\varepsilon$-$f_P$ EVM. Note that the $k$-$\varepsilon$-$f_P$ EVM is based on the initial solution of the iterative method of Apsley and Leschziner from Section 2.4.2, and it is also discussed and applied in Chapters 4-6. The comparisons show the potential and problems of the NLEVMs, when they are applied to ABL flows, with and without a wind turbine.

---

Parts of this chapter are published in: van der Laan, M. P., Sørensen, N. N., Réthoré, P.-E., Mann, J., Kelly, M. C. and Schepers, J. G. Nonlinear Eddy Viscosity Models applied to Wind Turbine Wakes. *Proceedings for the ICOWES2013, Copenhagen, Denmark*, 2013, 514-525.

## 3.2 Method

Two test cases are simulated; a clean ABL and a single wind turbine in an ABL that is based on field measurements from Wieringermeer in the Netherlands, which is presented in Section 4.3. The methodology of the single wind turbine wake simulations is given in Section 4.4.1, in which the flow domain, the boundary conditions, the wind turbine parametrization and the CFD solver are discussed in detail. The ABL simulations without a wind turbine use the same setup; however, the flow domain size and discretization is different. The size of the domain is $10\times1\times1$ km$^3$, and the domain is discretized with $192\times64\times32$ cells, for the streamwise, wall-normal and spanwise directions, respectively. The first cell height at the rough wall is set to the order of the roughness height, while the cells further away from the wall are stretched in the $z$-direction, using a maximum expansion ratio of 1.2. The flow domain of the clean ABL case is shown in Figure 3.1.

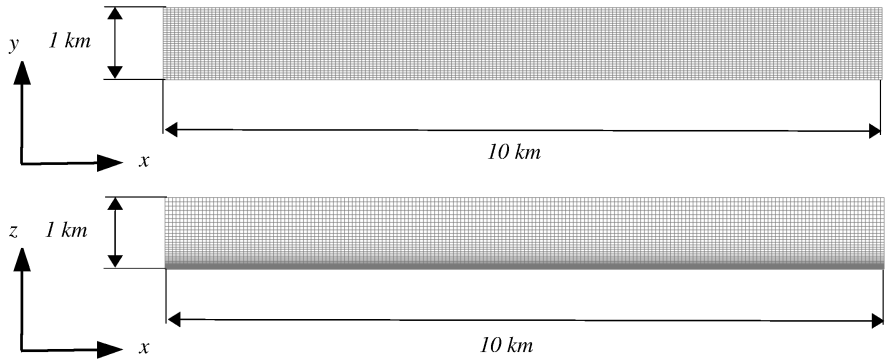


Figure 3.1: Computational domain of the clean ABL simulations (grid shown for $z_0 =$ 0.1 m). Top: top view. Bottom: side view.

### 3.2.1 Turbulence modeling

The following turbulence models are used to simulate an ABL, with and without a single wind turbine: the standard $k$-$\varepsilon$ EVM of Launder and Spalding,[31] the $k$-$\varepsilon$-$f_P$ EVM (from Chapter 4), the quadratic and the cubic NLEVMs of Apsley and Leschziner,[2] and a simplified version of the quartic NLEVM of Taulbee.[65] The order of the NLEVM refers to the highest power of the mean velocity gradients in the stress-strain relation, e.g., the cubic NLEVM has terms with $U_{i,k}U_{k,l}U_{l,j}$. An overview of the tested turbulence models is given in Table 3.1. The NLEVMs are derived in Chapter 2, and the definition of corresponding stress-strain relations are summarized in Appendix A. The kinematic eddy viscosity is defined in equation (2.62), in which the eddy viscosity coefficient $C_\mu$

Table 3.1: Description of the simulated turbulence models.

| Turbulence model | Source | Stress-strain | Effective $C_\mu$ |
|---|---|---|---|
| $k$-$\varepsilon$ EVM | Launder and Spalding[31] | linear, eq. (2.60) | constant |
| $k$-$\varepsilon$-$f_P$ EVM | van der Laan et al.,[76] based on Apsley and Leschziner[2] | linear, eq. (2.60) | variable, Tab. 2.1 |
| quadratic NLEVM | Apsley and Leschziner[2] | quadratic, Tab. A.1 | variable, Tab. 2.1 |
| cubic NLEVM | Apsley and Leschziner[2] | cubic, Tab. A.1 | variable, Tab. 2.1 |
| quartic NLEVM | Taulbee[65] | quartic, Tab. A.2 | variable, Tab. 2.1 |

is variable for all turbulence models except for the standard $k$-$\varepsilon$ EVM. All turbulence models use the transport equations for the turbulent kinetic energy $k$ and the turbulent dissipation $\varepsilon$, as defined in equation (2.63). In Section 2.4.3, the NLEVMs are calibrated against a simple shear flow that is characterized by the anisotropic Reynolds-stress components $\tilde{a}_{11}, \tilde{a}_{33}, \tilde{a}_{13}$ and the shear parameter $\tilde{\sigma}$. Apsley and Leschziner[2] extended their cubic NLEVM with wall functions for $\tilde{a}_{11}$, $\tilde{a}_{33}$, $\tilde{a}_{13}$ and $\tilde{\sigma}$, which are based on the results of direct numerical simulations of channel flow performed by Kim et al.[28] Since only the logarithmic region of the ABL is modeled in the present work, $\tilde{a}_{11}$, $\tilde{a}_{33}$, $\tilde{a}_{13}$ and $\tilde{\sigma}$ are chosen to be constant. The choice of these four constants will determine the scalar functions $G^{(\lambda)}$ that are present in the stress-strain relation from equation (2.26), hence, the model performance of the NLEVM is directly related to $\tilde{a}_{11}$, $\tilde{a}_{33}$, $\tilde{a}_{13}$ and $\tilde{\sigma}$. In a simple shear flow, an equilibrium between turbulent production $\mathscr{P}$ and turbulence dissipation $\varepsilon$ exists, i.e., $\mathscr{P}/\varepsilon = 1$, and $C_\mu$ can be related to $\tilde{\sigma}$ and $\tilde{a}_{13}$. The solution for the logarithmic region of a simple shear flow with a rough wall is equal to:

$$U = \frac{u_*}{\kappa} \ln\left(\frac{z}{z_0}\right), \qquad k = \frac{u_*^2}{\sqrt{C_\mu}}, \qquad \varepsilon = \frac{u_*^3}{\kappa z}, \tag{3.1}$$

with $U$ as the streamwise mean velocity, $u_*$ as the friction velocity, $\kappa$ as the Von Kármán constant, $z$ as the distance from the wall and $z_0$ as the wall roughness.[50] Hence:

$$\tilde{\sigma} = \frac{k}{\varepsilon}\left\|\frac{\partial U}{\partial z}\right\| = \frac{1}{\sqrt{C_\mu}}, \tag{3.2}$$

and

$$\left.\begin{aligned} \mathscr{P}/\varepsilon &\equiv -\{\mathbf{as}\} = 1 \\ &= -2\tilde{a}_{13}\tilde{s}_{13} = -\tilde{a}_{13}\tilde{\sigma} = -\tilde{a}_{13}\tfrac{1}{\sqrt{C_\mu}} \end{aligned}\right\} \Rightarrow \tilde{a}_{13} = -\sqrt{C_\mu}, \tag{3.3}$$

where equations (2.50) and (2.51) are employed. In atmospheric flows, the constant $C_\mu$ from the standard $k$-$\varepsilon$ EVM is chosen to be 0.03,[50] and it can be adopted in the

calibration of the NLEVMs. The value of $C_\mu$ is based on the log law solution for $k$ of equation (3.1):

$$C_\mu = \frac{u_*^4}{k^2} = \frac{u_*^4}{\frac{1}{4}\left(\sigma_u^2 + \sigma_v^2 + \sigma_w^2\right)^2} = 0.03, \tag{3.4}$$

where $\sigma_u$, $\sigma_v$ and $\sigma_w$ are measured standard deviations of the velocity components in a neutral ABL, that have been summarized by Panofsky and Dutton:[40]

$$\frac{\sigma_u}{u_*} = 2.39 \pm 0.03, \qquad \frac{\sigma_v}{u_*} = 1.92 \pm 0.05, \qquad \frac{\sigma_w}{u_*} = 1.25 \pm 0.03. \tag{3.5}$$

The other two calibration parameters $\tilde{a}_{11}$ and $\tilde{a}_{33}$ can also be derived from the same atmospheric measurements. The measured standard deviations can be rewritten into the normal components of the anisotropic Reynolds ($\tilde{a}_{ij} \equiv \overline{u_i' u_j'}/k - 2/3\delta_{ij}$):

$$\tilde{a}_{11} = 0.38, \qquad \tilde{a}_{22} = 0.00, \qquad \tilde{a}_{33} = -0.38. \tag{3.6}$$

Since $\tilde{a}_{11} + \tilde{a}_{33} = 0$, $\overline{\beta}$ becomes zero using Tables A.3 and A.4. Therefore, the stress-strain relation of the quadratic and cubic NLEVM of Apsley and Leschziner only include one and two nonlinear terms, respectively, since $G^{(3)}$ and $G^{(5)}$ are zero. In addition, the assumption of Taulbee ($\overline{\beta} = 0$) that is used to derive the corresponding quartic NLEVM, holds for this set of atmospheric measurements.

The nonlinear terms of the NLEVMs are implemented as source terms in the RANS momentum equations. The source terms are under-relaxed with a relaxation factor of 0.5.[38]

#### 3.2.1.1 Setting the turbulence level in RANS

For simulating atmospheric flows employing the standard $k$-$\varepsilon$ EVM, it is common to set $C_\mu$ such that the desired ambient turbulence intensity is obtained at a reference height $I_{H,\infty}$ (e.g. wind turbine hub height $z_H$):

$$I_{H,\infty} \equiv \frac{\sqrt{\frac{2}{3}k}}{U_{H,\infty}} = C_\mu^{-\frac{1}{4}} \sqrt{\frac{2}{3}} \frac{\kappa}{\ln\left(\frac{z_H}{z_0}\right)}, \tag{3.7}$$

where $U_{H,\infty}$ is the free-stream velocity at hub height. Subsequently, the logarithmic solution of equation (3.1) is preserved by adapting $C_{\varepsilon,1}$ as follows:[50]

$$C_{\varepsilon,1} = C_{\varepsilon,2} - \frac{\kappa^2}{\sqrt{C_\mu}\sigma_\varepsilon}. \tag{3.8}$$

Note that the other turbulence constants in the transport equations for $k$ and $\varepsilon$ of equation (2.63) are chosen to be: $C_{\varepsilon,2} = 1.92$, $\kappa = 0.4$, $\sigma_\varepsilon = 1.3$ and $\sigma_k = 1$. Unfortunately, it

is not possible to set $I_{H,\infty}$ with $C_\mu$ in the $k$-$\varepsilon$-$f_P$ EVM and NLEVMs, because the behavior of the variable $C_\mu^*$ relation changes unphysically with respect to the wake recovery, when it is adapted to have a desired $C_\mu$ value in equilibrium conditions (in the simple shear flow). This unphysical behavior is illustrated in Section 3.3.2.1. Therefore, we will use an alternative method to set $I_{H,\infty}$ by adapting $z_0$ in equation (3.7), while keeping the equilibrium value of $C_\mu$ to be 0.03. Subsequently, $u_*$ is adapted to obtain the desired free-stream velocity at hub height through equation (3.1). As a result, the simulated velocity profile can deviate from the measured profile, although the typical differences in the rotor area are in the order of a few percent. If the measured turbulence intensity is very different compared to the expected value that corresponds to the site roughness, then the simulated profile and the measured profile can have large differences. In such a case, it is most likely that the ambient turbulence level is dictated by processes that are not modeled in the current RANS setup, e.g. atmospheric stability or terrain effects.

## 3.3 Results and Discussion

The simulation results of the ABL with and without a wind turbine are discussed in Sections 3.3.2 and 3.3.1, respectively.

### 3.3.1 An ABL without wind turbine

All five turbulence models from Table 3.1 are applied to the ABL simulations, using two roughness heights: $z_0 = 0.1$ m and $z_0 = 10^{-4}$ m, which correspond to farmland with closed appearances and open sea, respectively.[67] Each model is simulated with four different values of $C_\mu$ that represent the traditional value ($C_\mu = 0.09$), the recommended value for atmospheric flows ($C_\mu = 0.03$) and two additional values that are used for testing ($C_\mu = 0.5$ and $C_\mu = 0.01$). Note that the velocity at a reference height of 100 m is set to 10 m/s. In addition, $C_{\varepsilon,1}$ is adapted through equation (3.8), such that the log law solution is maintained.

In Figure 3.2, the turbulent kinetic energy at $x = 5000$ m and $y = 500$ m, normalized with the friction velocity, is plotted against height. In each plot, four sets of solutions are presented that correspond to the four different $C_\mu$ values. The analytic solution of $k$ is shown as a dashed line. Not all results are shown because the cubic NLEVM and especially the quartic NLEVM are numerically unstable for most cases. Typically, these NLEVMs become more unstable for a lower $C_\mu$, which correspond to higher ambient turbulence intensities. The quartic NLEVM is only stable for $z_0 = 0.1$ m and $C_\mu = 0.5$, while the cubic NLEVM shows converged solutions for $C_\mu = 0.5$ and $C_\mu = 0.09$, for both roughness heights. However, the cubic NLEVM produces converged wiggles in the solution for $k$, for $z_0 = 0.1$ m and $C_\mu = 0.09$. The quartic NLEVM is unstable for $z_0 = 10^{-4}$ because the first cell height is set in the order of the roughness, which means that the resolved velocity gradient near the wall is increased since: $U_{i,j} = u_*/(\kappa z)$. The

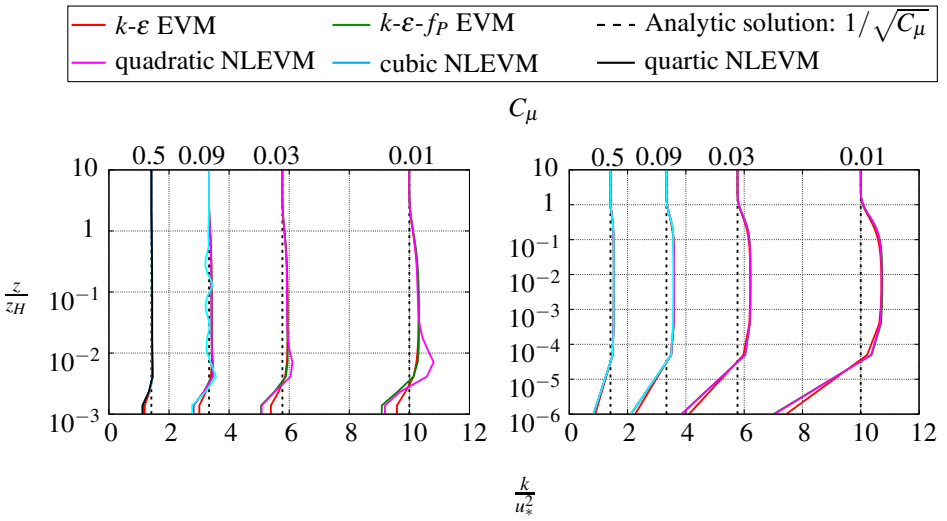


Figure 3.2: Turbulent kinetic energy at $x = 5000$ m, $y = 500$ m, for different $C_\mu$ and $z_0$ ($C_R = 1.8$). Left: $z_0 = 0.1$ m, right: $z_0 = 10^{-4}$ m. Reference height: $z_H = 100$ m.

numerically unstable behavior of the cubic and quartic NLEVMs, inhibits the use of these models for wind turbine wakes simulations in an ABL, using the recommended value of $C_\mu$ for atmospheric flows ($C_\mu = 0.03$). The other three turbulence models are stable for all cases. These models show a growth in the numerical error in $k$ with decreasing $C_\mu$, although the maximum relative error remains constant around 8%. The error in $k$ is associated with the rough wall, as discussed by Sumner and Masson.[64] In terms of $k$, the quadratic NLEVM is only different near the wall compared to the two linear EVMs, especially for $z_0 = 0.1$ m. Although not shown here, the difference in the velocity profile between these three turbulence models is negligible. The advantage of the quadratic NLEVM over the linear EVMs is that the quadratic NLEVM can predict the anisotropic Reynolds-stresses from equation (3.6), while the linear EVMs cannot, since their stress-strain relation is isotropic, i.e., $a_{kk} = 0$. This is illustrated in Figure 3.3, where the anisotropic Reynolds-stresses of the quadratic NLEVM are plotted at $x = 5000$ m and $y = 500$ m. Errors occur the near the wall because the anisotropic Reynolds-stresses are the normalized with $k$, which has large numerical errors in this region, as shown in Figure 3.2.

### 3.3.2 Single wind turbine in an ABL

The five turbulence models from Table 3.1 are applied to the two Wieringermeer cases described in Section 4.3. These cases differ in ambient turbulence intensity. In Sec-

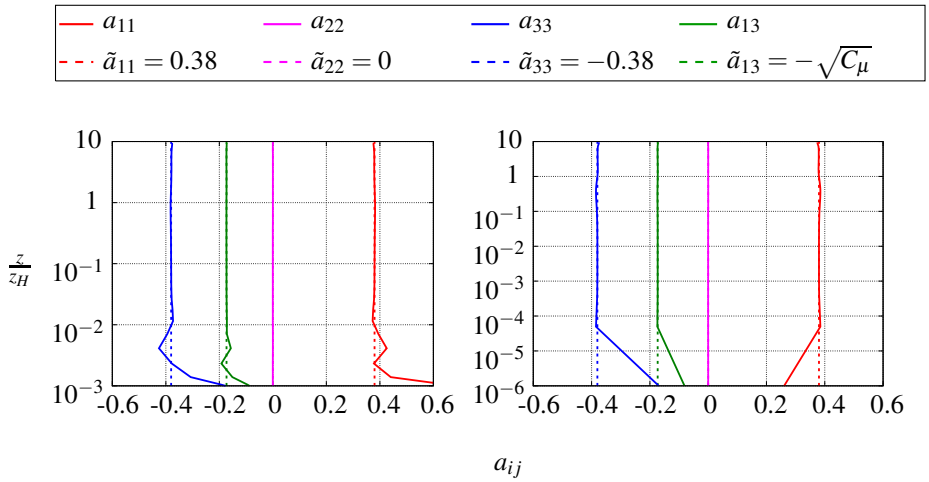


Figure 3.3: Anisotropic Reynolds-stresses at $x = 5000$ m, $y = 500$ m, predicted by the quadratic NLEVM with $C_\mu = 0.03$ ($C_R = 1.8$). Left: $z_0 = 0.1$ m, right: $z_0 = 10^{-4}$ m. Reference height: $z_H = 100$ m.

tion 3.3.2.1, the behavior of the variable $C_\mu^*$ is discussed. A grid study is presented in Section 3.3.2.2. Finally, the results of the RANS-based turbulence models are compared with LES in Section 3.3.2.3.

#### 3.3.2.1 Behavior of a variable $C_\mu^*$

In Figure 3.4, the wake recovery is shown by the streamwise velocity at hub height as function of the streamwise distance, at the AD center. The results of the $k$-$\varepsilon$ EVM, $k$-$\varepsilon$-$f_P$ EVM and the quadratic NLEVM are shown for the two Wieringermeer cases that differ in ambient turbulence intensity. The ambient turbulence intensity is set with $C_\mu$, using equation (3.7). The Rotta constant that is present in the $f_P$ function (equation (2.58)) of the $k$-$\varepsilon$-$f_P$ EVM and the quadratic NLEVM is set to its original value of 1.8. The $k$-$\varepsilon$-$f_P$ EVM and the quadratic NLEVM predict a slower wake recovery than the $k$-$\varepsilon$ EVM, which is caused by the variable part of $C_\mu^*$: $f_P$. In other words, $f_P$ delays the wake recovery. When comparing the two Wieringermeer cases in Figure 3.4, the $k$-$\varepsilon$ EVM predicts a faster wake recovery for a higher ambient turbulence intensity. This is expected, since increased turbulence levels enhance mixing. On the contrary, the $k$-$\varepsilon$-$f_P$ EVM and the quadratic NLEVM show the opposite behavior, which is unphysical. The effect is caused by $f_P$, which is a function of the $C_\mu$ that is present in the calibration flow (i.e., the ABL), since $f_P(\sigma/\tilde{\sigma})$ and $\tilde{\sigma} = 1/\sqrt{C_\mu}$. When $C_\mu$ is lowered to increase the ambient turbulence intensity through equation (3.7), the delaying effect of $f_P$ on

the wake recovery is increased. A similar behavior is observed for the more complex variable $C_\mu^*$ relations of the cubic and quartic NLEVMs (using test cases where these NLEVMs are stable). This indicates that the ambient turbulence intensity cannot be set using $C_\mu$, for the turbulence models that have a variable $C_\mu^*$.

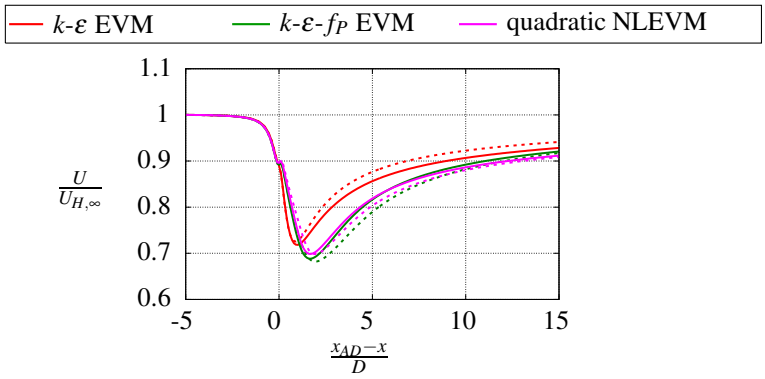


Figure 3.4: Wake recovery for different $C_\mu$ used to set $I_{H,\infty}$. Solid lines: Western Wieringermeer case ($I_{H,\infty} = 6\%$), dashed lines: Eastern Wieringermeer case ($I_{H,\infty} = 8\%$). $C_R = 1.8$.

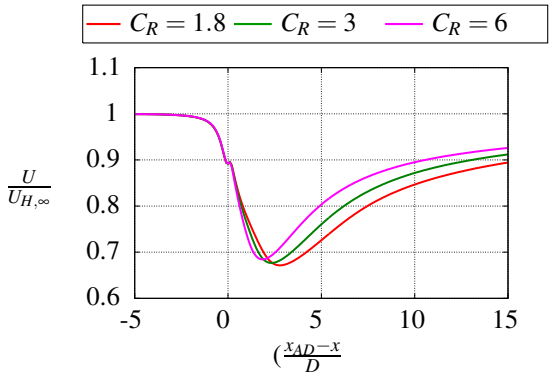


Figure 3.5: Wake recovery in the Western Wieringermeer case ($I_{H,\infty} = 8\%$) for different $C_R$, using the $k$-$\varepsilon$-$f_P$ EVM with $C_\mu = 0.03$.

The dependence of $C_R$ (the constant that is present in the $f_P$ function) on the wake recovery of the high ambient turbulence intensity case, is shown in Figure 3.5, for the $k$-$\varepsilon$-$f_P$ EVM. Three values of $C_R$ are used, the original 1.8 and two higher values of 3 and 6. It is clear that decreasing $C_R$, increases the delaying effect of $f_P$ on the wake recovery.

Therefore, $C_R$ is an important parameter that should not be used to fit the model results with a certain measurement. In Section 4.4.1.3, an extensive calibration of $C_R$ is carried out, using eight single wind turbine cases, to establish a generic ABL/turbine value. Although not shown in Figure 3.5, the quadratic and cubic NLEVMs show a similar behavior of $C_R$ on the wake recovery.

#### 3.3.2.2 Grid dependence study and numerical instability

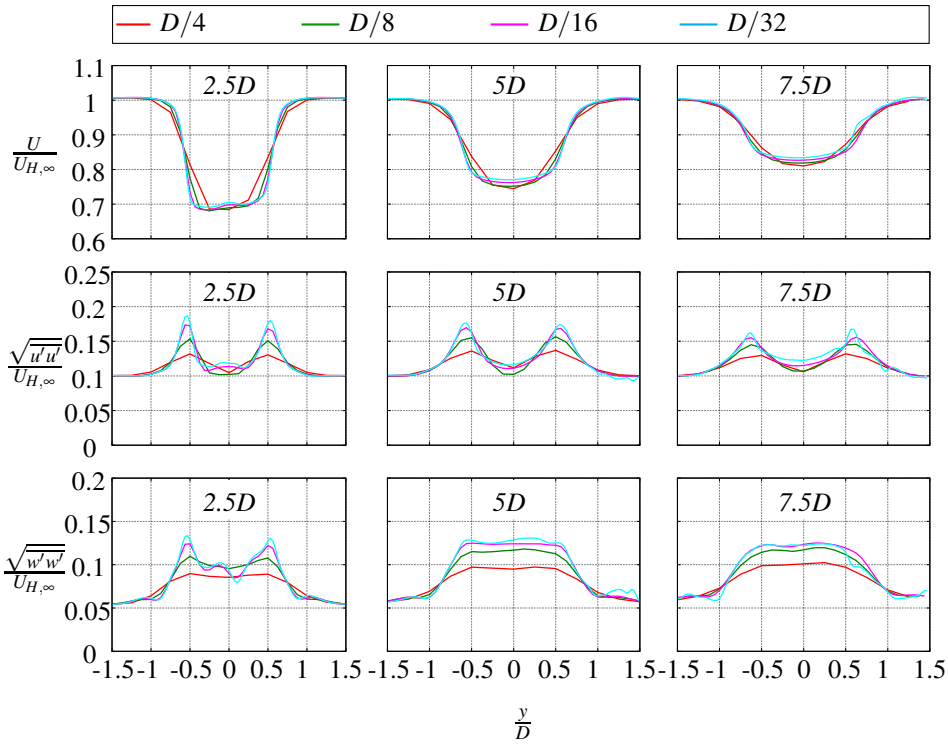


Figure 3.6: Grid dependency of quadratic NLEVM. Velocity deficit and Reynolds-stresses in Western Wieringermeer test case. $C_R = 1.8$, $C_\mu = 0.03$.

A grid dependency study is carried out for the quadratic NLEVM using the Western Wieringermeer case. Four grid levels are used with different cell sizes in the wake domain, namely: $D/4$, $D/8$, $D/16$ and $D/32$. In Figure 3.6, the velocity deficit, the streamwise Reynolds-stress $\overline{u'u'}$ and the vertical Reynolds-stress $\overline{w'w'}$ are plotted at hub height as function of $y$, for downstream distances 2.5D, 5D and 7.5D. The velocity gradient at the wake edge increases with grid refinement, which increases the peak in the

streamwise Reynolds-stress. In addition, the center of velocity deficit becomes more flat when the number of cells is increased. This indicates that the quadratic NLEVM is grid dependent for the presented grid solutions. More importantly, the finest two grids ($D/16$ and $D/32$) are not converged completely (2-3 orders of magnitude with respect to the initial solution), and further refinements leads to more unstable results. This means that the quadratic NLEVM cannot be numerically verified in a detailed grid study as performed for the $k$-$\varepsilon$-$f_P$ EVM in Section 4.4.1.1. The instability problems of the quadratic NLEVM that occur due to grid refinement are even worse for the cubic and quartic NLEVMs. The grid refinement study indicates that these instabilities are related to a too low eddy-viscosity, which creates a large velocity deficit that develops into a top hat profile when the grid is refined. In Chapter 2, the NLEVMs are derived from an algebraic RSM, which is derived from a differential RSM by neglecting the transport of Reynolds-stress as defined in equation (2.3). Therefore, the NLEVMs do not include the Reynolds-stress transport, which could explain the lack of diffusion that is observed when the NLEVMs become numerically unstable. More research is needed to confirm this statement.

#### 3.3.2.3 Comparison with LES

In Figures 3.7 and 3.8, the results of the $k$-$\varepsilon$ EVM, the $k$-$\varepsilon$-$f_P$ EVM, the quadratic NLEVM and the cubic NLEVM are compared with LES, using the Western and Eastern Wieringermeer cases, respectively. In these figures, the results of field measurements are also shown, but they are discussed in Sections 4.3 and 4.4.2.1. The LES setup is presented in Section 4.4.1.2, and the results correspond to 1 hour of LES data, which is split up into six 10 min bins. The standard deviation of the six bins are plotted as error bars. The cubic NLEVM shows numerical unstable behavior for $C_\mu = 0.03$, which is also observed in the ABL case without wind turbine, as discussed in Section 3.3.1. Therefore, the model is applied with $C_\mu = 0.09$, and $z_0$ and $u_*$ are re-adapted to obtain the desired free-stream velocity and ambient turbulence intensity at hub height. The results for the quartic NLEVM are not shown in Figures 3.7 and 3.8 because the model is unstable for both cases, even with $C_\mu = 0.09$.

In Figures 3.7 and 3.8, the velocity deficit, the streamwise Reynolds-stress $\overline{u'u'}$ and the vertical Reynolds-stress $\overline{w'w'}$ are plotted at hub height as function of $y$, for downstream distances 2.5D, 3.5D and 7.5D. Where the standard $k$-$\varepsilon$ EVM underpredicts the velocity deficit in the near wake, the $k$-$\varepsilon$-$f_P$ EVM, the quadratic NLEVM and the cubic NLEVM show comparable results as observed in the LES. In both Wieringermeer cases, the $k$-$\varepsilon$-$f_P$ EVM and the quadratic NLEVM show very similar results in the velocity deficit, which means that only the variable $C_\mu^*$ is responsible for the improvement in wake deficit, not the extra nonlinear term that is present in the quadratic NLEVM. On the contrary, the vertical Reynolds-stresses are influenced by the extra nonlinear term, because the quadratic NLEVM can reproduce the anisotropic Reynolds-stresses

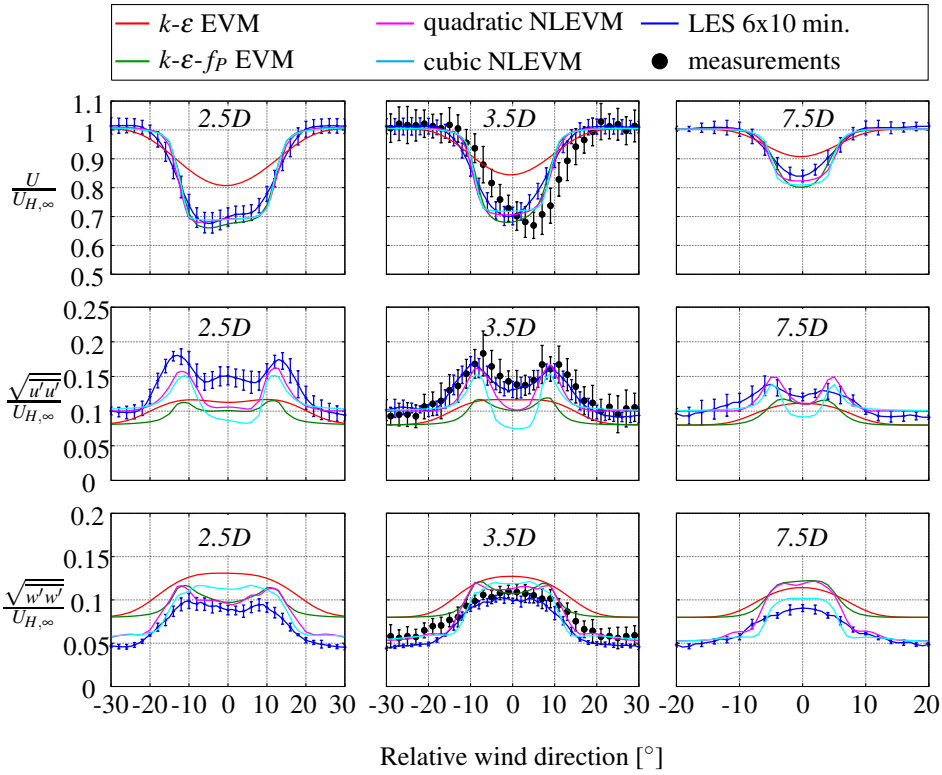


Figure 3.7: Velocity deficit and Reynolds-stresses in Western Wieringermeer test case ($I_{H,\infty} = 8\%$). The LES results include error bars of one standard deviation. All RANS-based turbulence models are simulated with $C_\mu = 0.03$, except for the cubic NLEVM: $C_\mu = 0.09$. $C_R = 1.8$.

in the ABL, whereas the Reynolds-stresses from $k$-$\varepsilon$-$f_P$ EVM are close to the standard (isotropic) $k$-$\varepsilon$ EVM. However, the NLEVMs overpredict the vertical Reynolds-stresses in the wake at 7.5D. The NLEVMs show improved streamwise Reynolds-stresses, although they still underpredict the magnitude in the center of the wake. In addition, the velocity gradients at the wake edge increase with the NLEVM model order, i.e., the cubic NLEVM produces the highest velocity gradients.

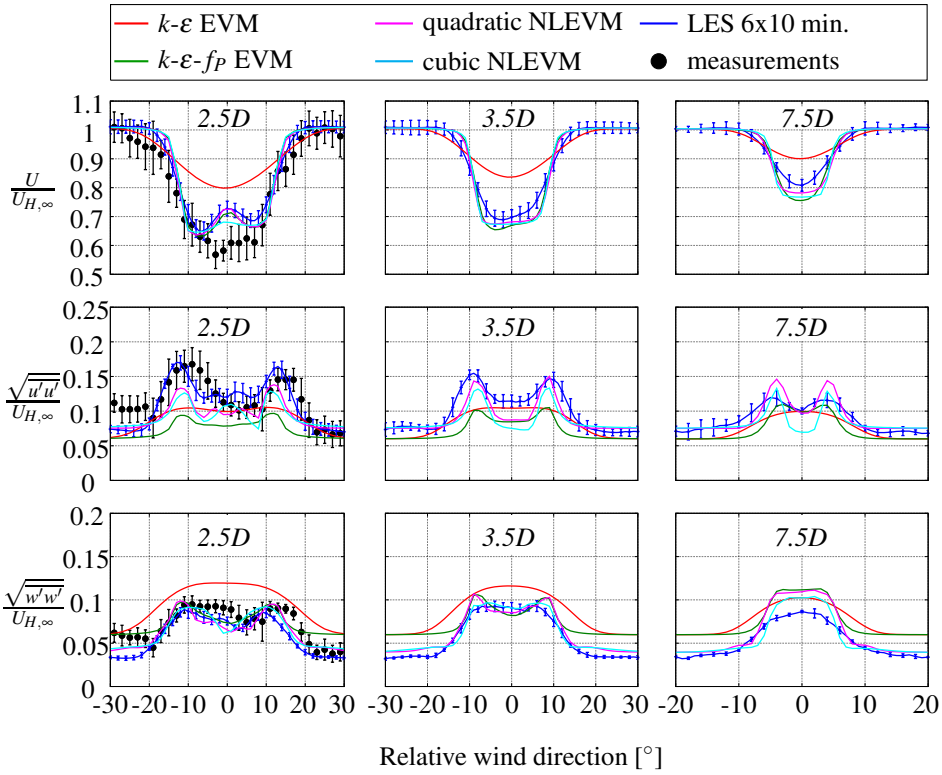


Figure 3.8: Velocity deficit and Reynolds-stresses in Eastern Wieringermeer test case ($I_{H,\infty} = 6\%$). The LES results include error bars of one standard deviation. All RANS-based turbulence models are simulated with $C_\mu = 0.03$, except for the cubic NLEVM: $C_\mu = 0.09$. $C_R = 1.8$.

## 3.4 Conclusions

The quadratic, cubic and quartic NLEVMs are applied to neutral ABL flows, with and without a single wind turbine, and the results are compared with the standard $k$-$\varepsilon$ EVM, the $k$-$\varepsilon$-$f_P$ EVM and LES. The simulations of a single wind turbine in an ABL are based on two field measurement cases from Wieringermeer, the Netherlands. In addition, a parametric study of $C_\mu$, $z_0$, $C_R$, $I_{H,\infty}$ and grid spacing is carried out.

All NLEVMs are numerically unstable for a small grid spacing and low values of $C_\mu$. These problems increase when higher order terms in the stress-strain relation are added. As a result, grid independence cannot be achieved for all NLEVMs and the cubic and quartic NLEVMs cannot be used with the recommended value of $C_\mu$, that is used

for ABL flows (0.03). When $C_\mu$ is lowered to set a higher ambient turbulence intensity at hub height, as traditionally performed for the standard $k$-$\varepsilon$ EVM, the wake recovery is unphysically accelerated. This behavior of the NLEVMs is caused by the variable $C_\mu^*$ (that is a function of the constant $C_\mu$), which has a stronger influence on the wake recovery than the prescribed ambient turbulence intensity. Hence, if the NLEVMs or the $k$-$\varepsilon$-$f_P$ EVM are used in wind turbine wake ABL simulations, the ambient turbulence intensity should be set with a different parameter, e.g., the roughness height.

The two single wind turbine cases show that the NLEVMs and the $k$-$\varepsilon$-$f_P$ EVM can predict velocity deficits that are comparable with LES. In fact, the quadratic NLEVM predicts very similar velocity deficits as the $k$-$\varepsilon$-$f_P$ EVM, which shows that the variable $C_\mu^*$ is mainly responsible for the improved velocity deficit, not the nonlinear terms in the stress-strain relation of the NLEVMs. However, only the NLEVMs improve the Reynolds-stresses compared to LES, while the $k$-$\varepsilon$-$f_P$ EVM shows similar results as the standard $k$-$\varepsilon$ EVM. This is caused by the fact that the $k$-$\varepsilon$-$f_P$ EVM is isotropic, and it cannot predict the anisotropic turbulence that is present in the wind turbine wake and the ABL. The NLEVMs still underpredict the streamwise Reynolds-stress in the center of wake, and overpredict the vertical Reynolds-stress in the far wake.

The most promising NLEVM is the quadratic NLEVM, since it is the most stable and simplest model of the tested NLEVMs, and it can improve the velocity deficit and the Reynolds-stresses. If the numerically unstable behavior of the quadratic NLEVM can be solved, the model is a good alternative to the standard $k$-$\varepsilon$ EVM to simulate wind turbine wakes in ABL flows.

# 4

# PAPER I: AN IMPROVED $k$-$\varepsilon$ MODEL APPLIED TO A WIND TURBINE WAKE IN ATMOSPHERIC TURBULENCE


## Abstract

An improved $k$-$\varepsilon$ turbulence model is developed and applied to a single wind turbine wake in a neutral atmospheric boundary layer using a Reynolds-averaged Navier-Stokes solver. The proposed model includes a flow-dependent $C_\mu$ that is sensitive to high velocity gradients, e.g. at the edge of a wind turbine wake. The modified $k$-$\varepsilon$ model is compared with the original $k$-$\varepsilon$ eddy viscosity model, large-eddy simulations and field measurements using eight test cases. The comparison shows that the velocity wake deficits, predicted by the proposed model are much closer to the ones calculated by the large-eddy simulations and those observed in the measurements, than predicted by the original $k$-$\varepsilon$ model.


## 4.1 Introduction

The energy losses in a wind farm due to the effects of wind turbine wakes can often range between 10% to 20%.[4] Wind turbine wakes also increase turbulence levels and can lead to early fatigue of wind turbines downstream. Therefore reliable and practical modeling of the influence of wind turbine wakes in wind farms is necessary, in order to estimate the wind farm annual energy production and the wind turbine loads. Wake effects have been studied using many tools, ranging from simple empirical engineering models to computational fluid dynamics (CFD) methods such as Reynolds-averaged Navier-Stokes (RANS) or large-eddy simulation (LES). LES results have proven to compare well with results of wake measurements,[69] but the computational costs are still high, especially if complete wind farms are considered. RANS is roughly three orders of magnitude less

This chapter has been published as: van der Laan, M. P., Sørensen, N. N., Réthoré, P.-E., Mann, J., Kelly, M. C., Troldborg, N., Schepers, J. G. and Machefaux, E. An improved $k$-$\varepsilon$ model applied to a wind turbine wake in atmospheric turbulence. *Wind Energy*, Published online, 2014.

of computational resources than LES (as illustrated in Section 4.4.2.3); however, previous studies have shown that the most widely used turbulence models in RANS, e.g., the (linear) $k$-$\varepsilon$ eddy viscosity model (EVM), fail to predict the wake deficit and the Reynolds-stresses in a wake.[10,16,45,46] The basis of a linear EVM is the eddy viscosity hypothesis of Boussinesq, which linearly relates the Reynolds-stresses to the symmetrical part of the velocity gradients.[9] Boussinesq hypothesis is seldom valid and can only predict isotropic turbulence.[43] Therefore, the $k$-$\varepsilon$ EVM cannot describe the anisotropic turbulence that is present in a neutral atmospheric boundary layer (ABL) nor in a wind turbine wake. In addition, the parameter $C_\mu$ present in definition of the eddy viscosity is a constant in the $k$-$\varepsilon$ EVM, which makes the model too dissipative when it is employed for a wake.

Modifications of the $k$-$\varepsilon$ EVM have been proposed and tested successfully for wind turbines wakes. El Kasmi and Masson[16] used an extra source term in the dissipation equation of the $k$-$\varepsilon$ EVM (originally proposed by Chen and Kim[12]), which is only active in the vicinity of the rotor. This source term includes a constant $C_{\varepsilon,4}$ that, together with the size of region where the source term is applied, determines the performance of the model. El Kasmi and Masson showed that the source term improves the velocity deficit for several cases compared with single wake measurements. Unfortunately, a thorough calibration of the source term is not published in the work of El Kasmi and Masson. Prospathopoulos et al.[45] and Réthoré[46] investigated the modified $k$-$\varepsilon$ EVM of El Kasmi and Masson, using different values of $C_{\varepsilon,4}$, while keeping the region of activity constant. Their work shows that the value of $C_{\varepsilon,4}$ is not general and needs to be adjusted for different single wind turbine wake cases. In addition, Prospathopoulos et al. showed that if the source term is calibrated to describe the velocity wake deficit at the far wake, it may not perform well in the near wake and vice versa. It should be noted that Prospathopoulos et al. and El Kasmi and Masson only compared the modified $k$-$\varepsilon$ EVM with measurements, not with LES, which can lead to an unfair comparison due to uncertainties in measurements. Cabezón et al.[10] investigated another modified $k$-$\varepsilon$ EVM, known as the realizable $k$-$\varepsilon$ EVM of Shih et al.[60] The model has a variable $C_\mu$ that is a complex scalar function of the local flow, i.e., a flow-dependent $C_\mu$, and it has a new transport equation for the dissipation rate. Cabezón et al. showed that the velocity deficit and the Reynolds-stresses (in some extent) predicted by the realizable $k$-$\varepsilon$ EVM compares better with those of LES and measurements, with respect to the standard $k$-$\varepsilon$ EVM. However, Cabezón et al. only considered one test case.

Another type of alternative eddy viscosity models are the nonlinear eddy viscosity models (NLEVMs). Instead of using the traditional Boussinesq hypothesis, the NLEVMs are based on a nonlinear stress-strain relationship in which products of the velocity gradients are present. In addition, the NLEVMs often have a flow-dependent $C_\mu$ that has similar behavior as the flow-dependent $C_\mu$ of the realizable $k$-$\varepsilon$ EVM of Shih et al.[60] In previous work, modified versions of the cubic NLEVM of Apsley and Leschziner[2] and the quartic NLEVM of Taulbee[65] have been employed for wind tur-

bine wake simulations.[74] The NLEVM of Taulbee is also applied to a single wind turbine wake in the work of Gomez-Elvira et al.[19] In terms of wake deficit and Reynolds-stresses, the performance of these NLEVMs is improved compared with the $k$-$\varepsilon$ EVM. The nonlinear terms in the stress-strain relationship can model anisotropic turbulence, and this is the main reason for the improved Reynolds-stress predictions. The flow-dependent $C_\mu$ lowers the eddy viscosity downstream of the wind turbine, which increases the wake deficit. As a result, the wake deficit predicted by the NLEVMs is closer to the one calculated by LES and observed in measurements. Unfortunately, the tested NLEVMs show numerically unstable behavior for high turbulence levels.[74] In addition, it has been found that the cubic and the quartic NLEVMs are not stable for fine grids, which is a major problem for grid refinement studies.

The goal of the present research is to develop a general RANS-based turbulence model that solves the shortcomings of the $k$-$\varepsilon$ EVM, without losing its simplicity and numerical stability. In addition, a model is desired that is general for a large range of different wind turbine wake cases and does not need recalibration. In this paper, a modified $k$-$\varepsilon$ EVM is presented that has a flow-dependent $C_\mu$, which we label as the $k$-$\varepsilon$-$f_P$ EVM. $f_P$ is a scalar function that includes the variability of the flow-dependent $C_\mu$. Hereafter, the flow-dependent $C_\mu$ is referred as $C_\mu^*$, i.e, $C_\mu^* = C_\mu f_P$ with $C_\mu$ as the traditional constant from the standard $k$-$\varepsilon$ EVM. The proposed model is a simplified version of the cubic NLEVM of Apsley and Leschziner,[2] in which the nonlinear terms in the stress-strain relationship are disregarded. By removing the nonlinear terms, the model is stable for the practical range of turbulence levels and grid spacings. Hence a grid refinement study is feasible, and the results show that the model becomes grid independent for fine enough grids, as discussed in Section 4.4.1.1. Since the proposed model is linear, only isotropic turbulence can be predicted, and one should not expect to observe significant improved Reynolds-stresses compared with the original $k$-$\varepsilon$ EVM, as observed for NLEVMs in the work of van der Laan et al.[74] Therefore, the current work focuses on improving the wake deficit. An advantage of the $k$-$\varepsilon$-$f_P$ EVM over the modified $k$-$\varepsilon$ EVM of El Kasmi and Masson,[16] is that the $k$-$\varepsilon$-$f_P$ EVM lets the flow decide where the modification is active, instead of using an arbitrary region in which it should be activated.

The $k$-$\varepsilon$-$f_P$ EVM is presented in Section 4.2, where the effect of $C_\mu^*$ is discussed. Section 4.2, also shows that the relation of $C_\mu^*$ in the $k$-$\varepsilon$-$f_P$ EVM is very similar to the one of the realizable $k$-$\varepsilon$ EVM of Shih et al.;[60] however, it is much simpler and has only one constant to calibrate, namely the Rotta constant $C_R$. The constant $C_R$ can be used to fit a certain measurement; however, it would be preferable not to calibrate the turbulence model each time a flow parameter is changed. Therefore, a comprehensive calibration of $C_R$ in the $k$-$\varepsilon$-$f_P$ EVM is presented in Section 4.4, in which eight single-wake cases are used. Four of the eight single-wake cases are based on field measurements and they are discussed in Section 4.3. Section 4.4 also covers the simulation methods, and a comparison is made between the $k$-$\varepsilon$-$f_P$ EVM, original $k$-$\varepsilon$ EVM, LES and available

measurements.

## 4.2 Model description

In Section 4.2.1 a brief description of the proposed $k$-$\varepsilon$-$f_P$ EVM is presented. The background and the effect of $C_\mu^*$ are discussed in Section 4.2.2. Note that repetitive indices are summed and an index after a comma represents a derivative.

### 4.2.1 Definition

The stress-strain relationship in the $k$-$\varepsilon$-$f_P$ EVM is exactly the same as the standard $k$-$\varepsilon$ EVM:

$$\overline{u_i' u_j'} = \frac{2}{3} k \delta_{ij} - \nu_T \left( U_{i,j} + U_{j,i} \right), \tag{4.1}$$

with $\overline{u_i' u_j'}$ as the Reynolds-stress, $k$ as the turbulent kinetic energy, $\delta_{ij}$ as the Kronecker delta and $U_{i,j}$ as the mean velocity gradient. The turbulent eddy viscosity $\nu_T$ in the proposed model is different from the standard $k$-$\varepsilon$ EVM but has the same form:

$$\nu_T = C_\mu^* \frac{k^2}{\varepsilon}, \tag{4.2}$$

with $\varepsilon$ as the turbulent dissipation and $C_\mu^*$ as a flow-dependent parameter, which is a constant in the original $k$-$\varepsilon$ EVM, i.e., $C_\mu$. The flow-dependent parameter $C_\mu^*$ is defined as:[2]

$$C_\mu^* = C_\mu f_P, \tag{4.3}$$

in which $f_P$ is a scalar function that models the effect of non-equilibrium flow conditions:[2]

$$f_P \left( \sigma / \tilde{\sigma} \right) = \frac{2 f_0}{1 + \sqrt{1 + 4 f_0 \left( f_0 - 1 \right) \left( \frac{\sigma}{\tilde{\sigma}} \right)^2}}, \qquad f_0 = \frac{C_R}{C_R - 1}, \tag{4.4}$$

with $C_R$ as the Rotta constant, originally chosen as 1.8.[29] Equation (4.4) is motivated in Section 4.2.2. The shear parameter $\sigma \equiv \frac{k}{\varepsilon} \sqrt{\left( U_{i,j} \right)^2}$ is used to quantify how far the local flow deviates from the log law regime of a simple shear flow, for which the $k$-$\varepsilon$-$f_P$ EVM is calibrated. In the calibration flow, the shear parameter $\sigma$ is equal to $\tilde{\sigma}$, i.e. $\tilde{\sigma} = \frac{k}{\varepsilon} \left\| \frac{\partial U}{\partial z} \right\| = 1 / \sqrt{C_\mu}$, using the log law solution of the $k$-$\varepsilon$ EVM.[50] Hence, $f_P$ is also a function of $C_\mu$, i.e., $f_P \left( C_\mu \right)$.

The $k$-$\varepsilon$-$f_P$ model uses the same transport equations for $k$ and $\varepsilon$ as employed in the original $k$-$\varepsilon$ EVM:

$$\frac{Dk}{Dt} = \nabla \cdot \left[ \left( \nu + \frac{\nu_T}{\sigma_k} \right) \nabla k \right] + \mathscr{P} - \varepsilon, \tag{4.5}$$
$$\frac{D\varepsilon}{Dt} = \nabla \cdot \left[ \left( \nu + \frac{\nu_T}{\sigma_\varepsilon} \right) \nabla \varepsilon \right] + \left( C_{\varepsilon,1} \mathscr{P} - C_{\varepsilon,2} \varepsilon \right) \frac{\varepsilon}{k},$$

where $\nu$ is the kinematic molecular viscosity, $\mathscr{P}$ is the turbulent production, and $C_{\varepsilon,1}, C_{\varepsilon,2}$, $\sigma_k$, $\sigma_\varepsilon$ are constants. In total, seven model constants exist in the $k$-$\varepsilon$-$f_P$ EVM, which are summarized in Table 4.1. The traditional $k$-$\varepsilon$ EVM constants are chosen to be able to describe a neutral ABL in which $C_\mu = 0.03$ and $C_{\varepsilon,1}$ is set such that the log law solution is recovered. The constant $C_R$ is calibrated with LES, as discussed in Section 4.4.

Table 4.1: Model constants.

| $C_R$ | $C_\mu$ | $C_{\varepsilon,1}$ | $C_{\varepsilon,2}$ | $\sigma_k$ | $\sigma_\varepsilon$ | $\kappa$ |
|---|---|---|---|---|---|---|
| 4.5 | 0.03 | 1.21 | 1.92 | 1.00 | 1.30 | 0.40 |

### 4.2.2 The $f_P$ function

Apsley and Leschziner[2] introduced the limiter function $f_P$ (equation (4.4)) to bound the nonlinear terms of their cubic NLEVM and extended it to non-equilibrium conditions. In the cubic NLEVM, $f_P$ is also used to obtain the relation for $C_\mu^*$, similar to equation (4.3). In the present research, the relation for $C_\mu^*$ is adopted, but all nonlinear terms are disregarded. Hence, the standard linear $k$-$\varepsilon$ EVM is recovered, including a variable $C_\mu$. Apsley and Leschziner derived their cubic NLEVM from an algebraic Reynolds-stress model in an approximate manner, with algebraic Reynolds-stress parameters $\alpha$, $\beta$ and $\gamma$ that are proportional to $1/(C_R + \mathscr{P}/\varepsilon - 1)$. $C_R$ represents the constant in the 'slow' part of the pressure-strain model of Launder et al.,[30,52] where $\mathscr{P}/\varepsilon$ is the ratio of turbulent production to dissipation. The derived cubic NLEVM includes the same parameters $\alpha$, $\beta$ and $\gamma$; however, they are used to calibrate the cubic NLEVM with a simple shear flow. Therefore, one can suggest to multiply the calibrated $\alpha$, $\beta$ and $\gamma$ in the cubic NLEVM with a factor:

$$f_P = \frac{C_R + \widetilde{\mathscr{P}/\varepsilon} - 1}{C_R + \mathscr{P}/\varepsilon - 1}, \tag{4.6}$$

in which $\widetilde{\mathscr{P}/\varepsilon}$ is the ratio of turbulent production and dissipation in the calibration flow, i.e., $\widetilde{\mathscr{P}/\varepsilon} = 1$. Apsley and Leschziner found that the direct use of equation (4.6) is numerically unstable and proposed the approximation $\mathscr{P}/\varepsilon \approx f_P C_\mu \sigma^2$, which is adopted

in the present research. This approximation, and using $\widetilde{\mathscr{P}/\varepsilon} = C_\mu \tilde{\sigma}^2$, leads to equation (4.4).

The behavior of $C_\mu^*$ is plotted in Figure 4.1 in terms of $f_P$ for the original and the calibrated value of $C_R$; 1.8 and 4.5, respectively. For comparison, a normalized $C_\mu^*$ of Shih et al.[60] is also shown, which is discussed in the next paragraph. $f_P$ is unity when the flow is in equilibrium ($\sigma = \tilde{\sigma}$, irrespective of $f_0$) and $C_\mu^*$ is equal to $C_\mu$. For $\sigma > \tilde{\sigma}$, $f_P < 1$, $C_\mu^*$ is lower than $C_\mu$. As a result, the eddy viscosity from equation (4.2) is lowered, and the $k$-$\varepsilon$-$f_P$ EVM behaves less dissipatively for high shear parameters compared with the original $k$-$\varepsilon$ EVM. In the near wake of a wind turbine, $\sigma$ can be much larger than $\tilde{\sigma}$, hence, $C_\mu^*$ has a high impact on the flow solution, which is mainly seen in the wake deficit, as shown in Section 4.4. When $C_R$ is increased the effect of $f_P$ is reduced, and the model behavior of the $k$-$\varepsilon$-$f_P$ EVM will approach that of the original $k$-$\varepsilon$ EVM. In terms of wake deficit, increasing $C_R$ will enhance the wake recovery, hence, $C_R$ controls the flow solution and should be carefully chosen. Instead of using the original value of 1.8, a comprehensive calibration of $C_R$ is carried out in Section 4.4.

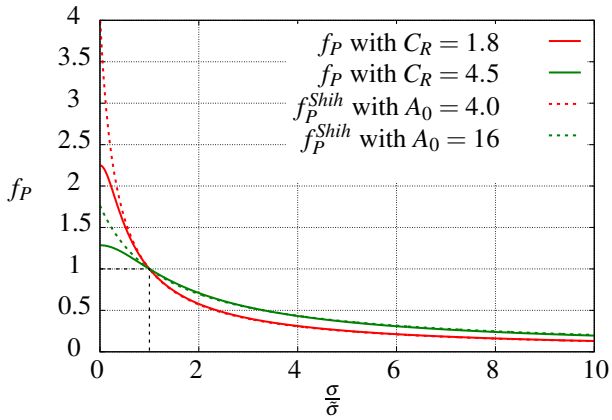


Figure 4.1: $f_P$ of $k$-$\varepsilon$-$f_P$ EVM and $f_P^{Shih}$, derived from the realizable $k$-$\varepsilon$ EVM of Shih et al., in a stationary frame of reference with $S_{kl}S_{lm}S_{mk} = 0$.

Another $C_\mu^*$ function is developed by Shih et al.,[60] which is derived using realizability arguments. This $C_\mu^*$ function is part of the realizable $k$-$\varepsilon$ EVM of Shih et al., which Cabezón et al.[10] tested successfully for wind turbine wake simulations. The function

can be written in the form of equation (4.4) (in a stationary frame of reference):

$$f_P^{Shih} \equiv \frac{C_\mu^*}{C_\mu^*\,|_{\sigma=\tilde{\sigma}}} = \frac{f_0}{1+(f_0-1)\,\frac{\sigma}{\tilde{\sigma}}}, \qquad f_0 = 1+\tilde{\sigma}\frac{A_s}{A_0},$$
$$A_s = \sqrt{6}\cos\left[1/3\arccos\left(\sqrt{6}\frac{S_{kl}S_{lm}S_{mk}}{(S_{kl}S_{lk})^{(3/2)}}\right)\right], \tag{4.7}$$

where $A_0$ is a constant, originally set to 4.0.[60] $A_s$ is a complex relation of traces of products of the strain-rate tensor $S_{ij} \equiv 1/2\,(U_{i,j}+U_{j,i})$. Note that the normalization is performed with $C_\mu^*\,|_{\sigma=\tilde{\sigma}}$, such that a comparison can be made with the limiter function $f_P$ of Apsley and Leschziner. For $S_{kl}S_{lm}S_{mk}=0$ (valid in the log law region of the ABL and for 2D flows), $A_s = 3/2\sqrt{2}$ and $f_P^{Shih}$ is very similar to the $f_P$ with $C_R = 1.8$, especially for $\frac{\sigma}{\tilde{\sigma}} > 1$. Deviations between $f_P^{Shih}$ and $f_P$ are observed for $\frac{\sigma}{\tilde{\sigma}} < 1$. In addition, Figure 4.1 shows that increasing $A_0$ ($A_0 = 16$) has a similar effect as increasing $C_R$. In principle $f_P^{Shih}$ can also be applied in the $k$-$\varepsilon$-$f_P$ EVM instead of $f_P$, however, it has been found that $f_P$ is more robust compared with $f_P^{Shih}$.

## 4.3 Test cases

The $k$-$\varepsilon$-$f_P$ EVM is used to simulate the wake of a single wind turbine for eight test cases. An overview of the test cases is given in Table 4.2. The first two test cases are based on meteorological mast (MM) wake measurements from the Wind Turbine Test Site Wieringermeer, owned by the Energy Research Centre of the Netherlands (ECN).[57] The third test case is based on an old measurement campaign, namely the field wake measurements of the Nibe B wind turbine conducted in Denmark.[66] The fourth test case is derived from a set of recent lidar measurements of a Nordtank (Vestas Wind Systems A/S, Hedeager 44, 8200 Aarhus N, Denmark) 500 test wind turbine, owned and maintained by the Technical University of Denmark (DTU).[34] Finally, four additional test cases are defined to investigate the influence of the undisturbed turbulence intensity at hub height $I_{H,\infty} \equiv \sqrt{(2/3k)}/U_H$ and the thrust coefficient $C_T$. These parameters are considered as the most important ones for a wind turbine wake in a neutral ABL, since other parameters are either used to normalize the wake deficit (undisturbed wind speed at hub height $U_{H,\infty}$ and rotor diameter $D$) or else they can be related to the turbulence intensity (roughness height $z_0$, friction velocity $u_*$ and hub height $z_H$). In addition, the rotational force component is not expected to play a large role in the wake deficit compared with the thrust coefficient. The four additional test cases are based on the National Renewable Energy Laboratory (NREL) 5-MW reference wind turbine.[26] The high undisturbed turbulence intensity in case 6 is chosen to reflect the maximum streamwise undisturbed turbulence intensity of 16%, using equation (4.9). In the last two test cases, only $C_T$ is changed while other parameters ($C_P$, $U_{H,\infty}$, etc.) are kept the same. This approach

leads to a setup that does not resemble the $C_P$ and $C_T$ dependency on wind speed that correspond to the original NREL 5-MW wind turbine, however, the influence of $C_T$ on the wake deficit can now be investigated.

In order to compare the measurements with the numerical simulations, the following input parameters for the numerical simulations are necessary: the undisturbed turbulence intensity at hub height $I_{H,\infty}$, the thrust coefficient $C_T$, the power coefficient $C_P$, the rotational speed $\Omega$, the undisturbed wind speed at hub height $U_{H,\infty}$, the rotor diameter $D$ and the hub height $z_H$. The roughness height $z_0$ and the undisturbed friction velocity $u_*$ are not input parameters for the simulations, because these parameters will be used to control the turbulence intensity at hub height as discussed in Section 4.4.1.1. The test cases that are based on measurements are described in the following sections.

Table 4.2: Summary of cases and corresponding input parameters for numerical computations.

| Case | Description | Data | $I_{H,\infty}$ [%] | $C_T$ [-] | $C_P$ [-] | $\Omega$ [rpm] | $U_{H,\infty}$ [m/s] | $D$ [m] | $z_H$ [m] |
|---|---|---|---|---|---|---|---|---|---|
| 1 | Wieringermeer West | Met. mast | 8.0 | 0.63 | 0.44 | 19.1 | 10.7 | 80 | 80 |
| 2 | Wieringermeer East | Met. mast | 6.0 | 0.63 | 0.44 | 19.1 | 10.9 | 80 | 80 |
| 3 | Nibe B | Met. mast | 8.0 | 0.89 | 0.46 | 34 | 8.5 | 40 | 45 |
| 4 | Nordtank 500 | Lidar | 11.2 | 0.70 | 0.44 | 27.1 | 7.45 | 41 | 36 |
| 5 | NREL 5-MW Low $I_{H,\infty}$ | - | 4.0 | 0.79 | 0.47 | 9 | 8.0 | 126 | 90 |
| 6 | NREL 5-MW High $I_{H,\infty}$ | - | 12.8 | 0.79 | 0.47 | 9 | 8.0 | 126 | 90 |
| 7 | NREL 5-MW Low $C_T$ | - | 8.0 | 0.50 | 0.47 | 9 | 8.0 | 126 | 90 |
| 8 | NREL 5-MW High $C_T$ | - | 8.0 | 0.90 | 0.47 | 9 | 8.0 | 126 | 90 |

### 4.3.1 Wieringermeer

The ECN Wind Turbine Test Site is located in Wieringermeer, an area in the northwest of the Netherlands. The landscape mainly consist of flat farmland. Two kilometers East from the MM a large lake (IJsselmeer) is present. The land and the lake are separated by a dike which rises 8 and 3 m above the land and the lake, respectively. The MM is located south of five 2.5 MW Nordex (Nordex SE, Langenhorner Chaussee 600, 22419 Hamburg, Germany) wind turbines, all with a 80 m rotor diameter and hub height. The layout of the five wind turbine positions is given in Figure 4.2. Two single wake cases are measured for wind directions around 31°and 315°with a corresponding downstream distance of 2.5D and 3.5D, respectively. The results of almost 5 years of measurements have been published by Schepers et al.[57] In addition, the 10 min averaged data was made available for this research.

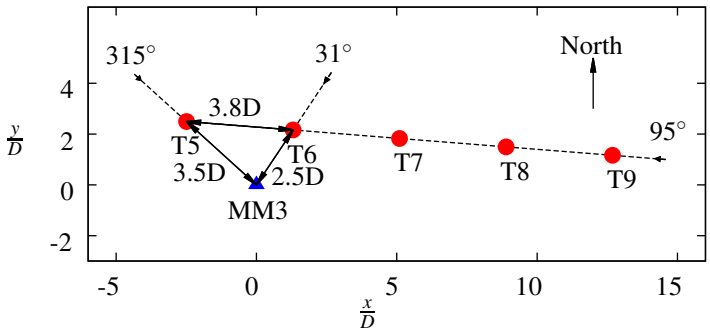


Figure 4.2: Sketch of wind turbines (red dots) and meteorological mast (blue triangle) at EWTW site.

The MM is instrumented with sonic anemometers, cups and vanes at 80 m. Unfortunately, upstream measurements are not carried out. Therefore, the upstream undisturbed wind speed at hub height is estimated from power measurements of wind turbine T5 (Eastern wake case) and wind turbine T6 (Western wake case). Only data with undisturbed wind speeds between 10-12 m/s is selected, which is the highest wind speed bin available. The average wind speed between 1-61°and 285-345°, corresponding to the two single wake cases, are 10.9 m/s and 10.7 m/s, respectively. The lack of upstream measurements makes it impossible to identify and disregard non-neutral atmospheric measurements. However, the probability of a near neutral ABL increases with high wind speeds, i.e., 10-12 m/s. Another important consequence of missing upstream measurements is the fact that the undisturbed turbulence intensity cannot be directly measured for the wind direction of single wake cases. Schepers et al.[57] estimated the undisturbed streamwise turbulence intensities $I_{u,H,\infty} \equiv \sigma_u/U_H$ (outside the region of wind directions corresponding to the single wake cases) to be 10% and 7.5% for the Western and Eastern wind directions, respectively. Since the three standard deviations of the velocity components $\sigma_u, \sigma_v$ and $\sigma_w$ are not all available, the total turbulence intensity $I_{H,\infty}$ is estimated from the standard ratios:

$$\frac{\sigma_v}{\sigma_u} = 0.8, \qquad \frac{\sigma_w}{\sigma_u} = 0.5, \tag{4.8}$$

which have been measured by Panofsky and Dutton[40] and are adopted in the IEC 61400-1 standard.[1] This leads to:

$$I_{H,\infty} = I_{u,H,\infty}\sqrt{\frac{1}{3}\left(1+0.8^2+0.5^2\right)} \approx 0.8 I_{u,H,\infty}, \tag{4.9}$$

hence, the total turbulence intensity $I_{H,\infty}$ is estimated to be 8% and 6% for the Western and Eastern wind directions, respectively.

The thrust coefficient curve is measured and calculated by Schepers.[56] The measurements are based on the tower bending moment, and the calculations are carried out with PHATAS.[33] Both methods estimate a thrust coefficient of 0.63 for the averaged undisturbed wind speeds of 10.7 and 10.9 m/s.

The mechanical power curve is not available. Therefore, it is estimated from the electrical power curve (given by the wind turbine manufacturer Nordex) assuming a loss of 6%. This gives a power coefficient of 0.44 for both Wieringermeer cases.

The Nordex wind turbine has variable rotational speeds ranging from 10.9 to 19.1 rpm. The dependence of the rotational speed on the wind speed is not available. For the present research, it is assumed that the rotor is rotating with 19.1 rpm.

### 4.3.2 Nibe

In the 1980s field measurements of two wind turbines at Nibe, in Northern Denmark, were conducted by Taylor.[66] The wind turbines have a hub height and rotor diameter of 45 and 40 m, respectively. The two wind turbines are located at five rotor diameters away from each other. The Nibe B wind turbine (the Nibe wind turbines were prototypes that were used for a Danish research project, involving several Danish companies) is located South from Nibe A wind turbine. A sketch of the layout is shown in Figure 4.3. Four MMs are placed in a line at downstream distances: 2.5D, 4D, 6D and 7.5D with respect to the Nibe B wind turbine. The masts are instrumented with cup anemometers at several heights. The selected data set includes wind directions from the South, which corresponds to inflow condition over land with a relatively flat terrain. For the current single wake case of the Nibe B wind turbine, the Nibe A wind turbine is not operational; however, an influence of the Nibe A wind turbine on the downstream MMs at 6D and 7.5D cannot be avoided. For this reason, the data at 6D (MM3, located at 1D from the Nibe A wind turbine) is disregarded.

The chosen data set consist of 1 min averages, taken over a period of about 2 years. The averaged velocity of 8.5 m/s is obtained from power measurements and the known power curve.

Due to lack of upstream measurements, the undisturbed streamwise turbulence intensity is estimated from a cup anemometer located at the mast at 2.5D downstream from Nibe B, at a height of 3 m. It is assumed that the wake of the Nibe B turbine has not expanded far enough to influence the measurement at this location.[66] Unfortunately, this estimate of the undisturbed streamwise turbulence intensity is not very accurate because the influence of local surface variations can be significant at 3 m. The rough estimate gives an undisturbed streamwise turbulence intensity of $I_{u,H,\infty} \approx 10\%$ which corresponds to a total turbulence intensity of $I_{H,\infty} \approx 8\%$ using equation (4.9).

Filtering out non-neutral atmospheric measurements has not been been carried out.

The thrust coefficient $C_T$ is estimated as an average of an LES actuator line simulation in which tabulated airfoil data is used to calculated the blade forces. More details

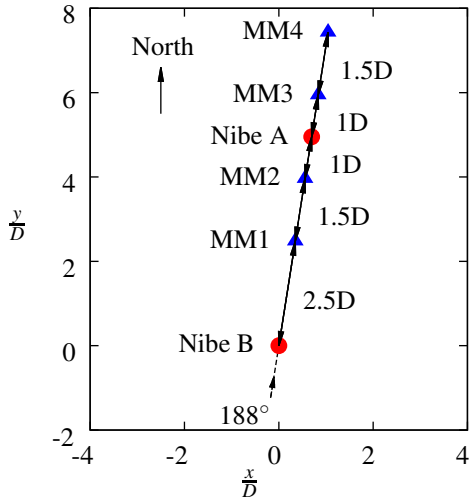


Figure 4.3: Sketch of wind turbines (red dots) and MMs (blue triangles) at Nibe.

about this simulation can be found in the work of Troldborg et al.[71] The method gives a $C_T$ of 0.89, which also corresponds to the calculated thrust curve given in the work of Taylor.[66] The power coefficient could also be taken from the same LES actuator line simulation; however, it has been found that the LES actuator line simulation overestimates the power.[72,73] Therefore, the power coefficient $C_P = 0.46$ is estimated from the measured mechanical power curve, given by Taylor.[66] In addition, the rotational speed is also noted by Taylor: $\Omega = 43$ rpm.

### 4.3.3 Nordtank 500

A test site consisting of three wind turbines is situated on the Risø campus of DTU. An overview is sketched in Figure 4.4. From left to right, the order of wind turbines is as follows: Tellus wind turbine, 95 kW, $D = 18$ m, $z_H = 29$ m, Nordtank 500 wind turbine (NTK), 500 kW, $D = 41$ m, $z_H = 36$ m, Vestas V27 (Vestas Wind Systems A/S, Hedeager 44, 8200 Aarhus N, Denmark) wind turbine, 225 kW, $D = 27$ m, $z_H = 30$ m. In addition, there is an MM at 2.2D West from the Nordtank 500 wind turbine. During the measurement campaign the rotor of the Vestas V27 wind turbine was taken down. The prevailing wind direction is South East, therefore, only data is selected for wind directions between 120° to 150°. The single wake of the Nordtank 500 wind turbine is measured using a nacelle mounted pulsed lidar. The measurements are prepared by Machefaux et al., unpublished data using similar techniques as published in Machefaux et al.[34] The lidar is used to scan the wake in a cross section at five downstream locations

between 1D and 5D with a uniform spacing of 1D. The MM is instrumented with cup and sonic anemometers at several heights. Only the results at a height of 52.5 m are used from this mast, in order to prevent the wake influence of the Tellus wind turbine.

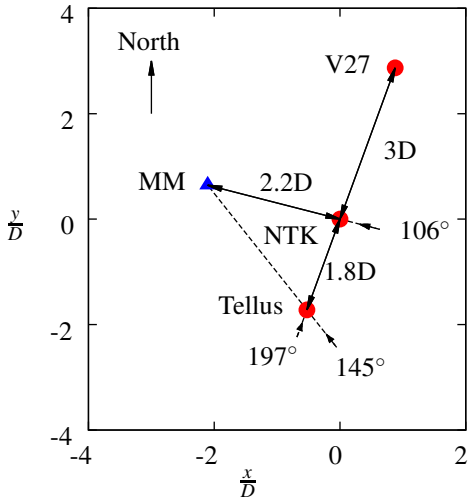


Figure 4.4: Sketch of wind turbines (red dots) and MM (blue triangle) at the Risø campus of the Technical University of Denmark. Distances are normalized with the rotor diameter of the Nordtank 500 (NTK) wind turbine: $D = 41$ m.

The undisturbed velocity at hub height is calculated from power measurements and the known power curve. This velocity is also directly measured at the MM at hub height, however, these measurements are influenced by the wake of Tellus wind turbine. In total 102 samples of approximately 10 min averages are selected, with a velocity of 7-8 m/s and wind directions between 120° to 150°. This represents almost 17 hours of data, and its average velocity is calculated as 7.45 m/s.

The Obukhov length $L$ is calculated from the sonics at the MM, and it is used to identify the stability class of the measurements. It is found that the atmospheric conditions during the time of measurements are neutral: $(\text{mean}(\text{abs}(L)) = 7.5 \times 10^2)$.

The thrust coefficient $C_T$ is estimated from the tower bending moment, which gives $C_T = 0.70$.

The MM is used to estimate the undisturbed turbulence intensity. Since the Tellus wind turbine wake influences the measurements at the MM around hub height, the turbulence intensity $I_{M,\infty}$, obtained from a sonic located at a height: $z_M = 52.5$ m is used. The undisturbed turbulence intensity at hub height is estimated by using the log law and

assuming that $\sigma_u = Au_*$ is constant with height. Hence,

$$I_{H,\infty} = \frac{I_{M,\infty}}{1 - \frac{I_{u,M,\infty}}{\kappa A} \ln\left(\frac{z_M}{z_H}\right)}, \tag{4.10}$$

where $\kappa$ is the Von Kármán constant, and $A$ is function of the roughness height. Following Panofsky and Dutton,[40] $A = 2.4$. Using equation (4.10) the measured total turbulence intensity at the mast ($I_{M,\infty} = 10.7\%$) is extrapolated to the hub height: $I_{H,\infty} = 11.2\%$ which is equivalent to a streamwise turbulence intensity of 14% using equation (4.9).

## 4.4 Simulations

### 4.4.1 Method

The in-house incompressible finite volume code EllipSys3D is used as the flow solver, which can perform RANS and LES simulations.[36,62] The Navier-Stokes equations are solved with the SIMPLE algorithm,[41] and the QUICK scheme[32] is used to discretize the convective terms. The flow variables are stored in a co-located manner. To avoid decoupling of the pressure with body forces, the pressure equation is solved with a modified Rhie-Chow algorithm.[47,49]

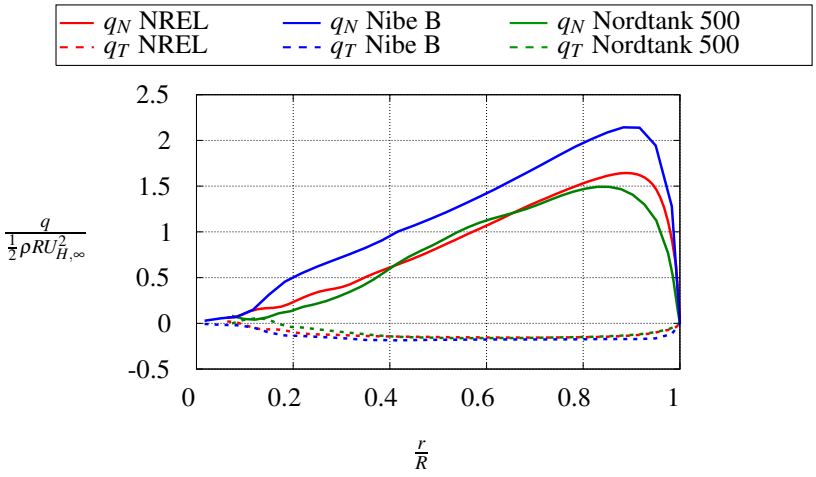


Figure 4.5: Calculated tangential $q_T$ and normal force $q_N$ distributions [n/m].

The wind turbine is modeled as an Actuator Disk (AD)[37,46,48] on which the blade forces are distributed in the radial direction and constant in the circumferential direction. The blade force distributions that are applied on the AD are calculated with a full rotor

detached-eddy simulation (Nordtank 500 and NREL 5 MW) or are calculated with a LES simulation using an actuator line method including airfoil data (Nibe B).[71] The result for the normal and the tangential force distributions are shown in Figure 4.5. The radial blade force is not applied to the AD because it is often smaller than 1% of the normal blade force. The real blade geometry of the Nordex wind turbine from EWTW is not available. Therefore, the detached-eddy simulation of the NREL 5 MW wind turbine blade is used, in which the original tangential ($q_T(r/R)$) and normal blade force distribution ($q_N(r/R)$) are scaled. First, $q_T(r/R)$ and $q_N(r/R)$ are scaled to cover the desired rotor radius $R$. Subsequently, $q_T(r)$ and $q_N(r)$ are individually scaled with $C_P$, $\Omega$ and $C_T$, respectively. In addition, both distributions are scaled with $U_{H,\infty}$, $R$ and $\rho$ to obtain the tangential ($q_T^{AD}(r)$) and normal blade force distribution ($q_N^{AD}(r)$) that are applied to the AD:

$$q_N^{AD}(r) = \hat{q}_N(r)\frac{1}{n}\frac{1}{2}\rho U_{H,\infty}^2 \pi R^2 C_T, \qquad \hat{q}_N(r) = \frac{q_N(r)}{\int_0^R q_N(r)dr}, \tag{4.11}$$

$$q_T^{AD}(r) = \hat{q}_T(r)\frac{1}{n}\frac{\frac{1}{2}\rho U_{H,\infty}^3 \pi R^2 C_P}{2\pi\Omega/60}, \qquad \hat{q}_T(r) = \frac{q_T(r)}{\int_0^R q_T(r)rdr},$$

where $n = 3$ is the number of blades and $\hat{q}(r)$ denotes a normalized blade force distribution. The total normal force $F_N$ and the power $P$ are obtained by integration:

$$F_N = n\int_0^R q_N^{AD}(r)dr = \frac{1}{2}\rho U_{H,\infty}^2 \pi R^2 C_T, \tag{4.12}$$

$$P = 2\pi\Omega/60 n\int_0^R q_T^{AD}(r)rdr = \frac{1}{2}\rho U_{H,\infty}^3 \pi R^2 C_P.$$

The scaling equations can easily be verified by taking analytical force distributions for the original blade, e.q.: $q_N(r) = -q_T(r) = -r(r-R)/R^2$, and substitute these relations into equation (4.11).

The input parameters from Table 4.2 are used in all AD simulations. Standard values for the density and the dynamic fluid viscosity are used as follows: $\rho = 1.225$ kg/m$^3$ and $\mu = 1.784 \times 10^{-5}$ kg/(m·s) (corresponding to a temperature of 15 °C at sea level). It should be noted that the fluid viscosity is negligible compared with the eddy viscosity, since the Reynolds number (based on the rotor diameter and the hub height velocity) is in the order of $10^7$.

#### 4.4.1.1 RANS

In the RANS simulations, the AD is placed in a box shaped domain of dimensions: 25D × 16D × 16D, as shown in Figure 4.6. In total 1.18 million cells are used to discretize the domain. The boundary at $z = 0$ is modeled as a rough wall where the first cell height is on the order of the roughness height. In EllipSys3D, a rough wall is modeled by

placing the flow domain on top of the roughness height. The wall stress and the turbulent dissipation are specified at the first cell, using the analytical expressions of the log law. In addition, a Neumann boundary condition is used for the turbulent kinetic energy. The top boundary at $z = 16\text{D}$ and the boundaries at $x = 0$ are inlets, whereas, the boundary at $x = 25\text{D}$ is an outlet. At the inlet a streamwise logarithmic profile is specified:

$$U = \frac{u_*}{\kappa} \ln\left(\frac{z}{z_0}\right). \tag{4.13}$$

A Neumann boundary condition is applied on the outlet boundary. The side boundaries at $y = 0$ and $y = 16\text{D}$ are modeled as slip walls. Around the AD a wake domain of dimensions: $14\text{D} \times 3\text{D} \times 3\text{D}$ is defined where uniform spacing of D/10 is applied in all directions. (Below $z = 1/2 z_H$ the cells in the wall normal direction are refined due to the presence of the wall.) The grid study in the section below shows that eight cells per diameter is sufficient. Outside the wake domain, stretching is allowed with a maximum edge growth ratio of 1.2.

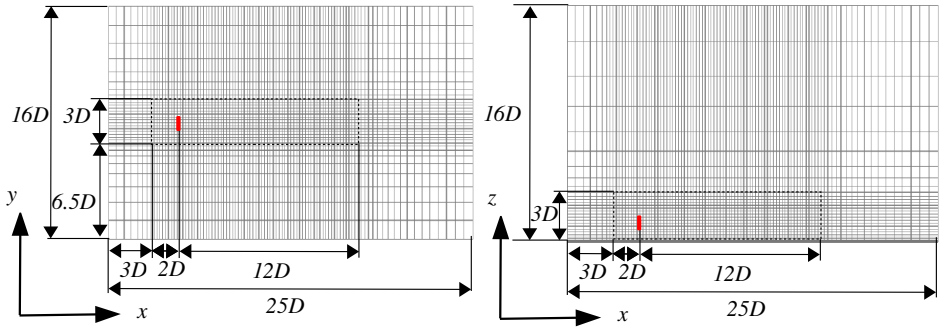


Figure 4.6: Computational domain RANS. Left: top view. Right: side view. Dashed black box marks the wake domain. Actuator disk is illustrated as a red filled box. One in every two nodes is shown.

### Setting the turbulence level in RANS via $z_0$

In the RANS modeling of atmospheric flows using the standard $k$-$\varepsilon$ EVM, it is common to control the ambient turbulence intensity at hub height $I_{H,\infty}$:

$$I_{H,\infty} \equiv \frac{\sqrt{\frac{2}{3}k}}{U_{H,\infty}} = \frac{\kappa\sqrt{\frac{2}{3}}}{\ln\left(\frac{z_H}{z_0}\right)\sqrt[4]{C_\mu}}, \tag{4.14}$$

by changing $C_\mu$ and adapting one of the other model constants such that the log law solution (equation (4.13)) is maintained as follows: $\sqrt{C_\mu}\sigma_\varepsilon\left(C_{\varepsilon,1}-C_{\varepsilon,2}\right)+\kappa^2=0$.[50] Note that equation (4.13) is used for $z=z_H$ and $U=U_H$, together with the analytical solution for the turbulent kinetic energy in the log law: $k=u_*^2/\sqrt{C_\mu}$. However, the behavior of the $k$-$\varepsilon$-$f_P$ EVM changes when the constant $C_\mu$ is modified, because $C_\mu$ is also present in $f_P$: $f_P(C_\mu)$, as explained in Section 4.2.2. Van der Laan et al.[74] showed that $f_P$ reduces the wake recovery for lower values of $C_\mu$, which correspond to a higher turbulence intensity in equation (4.14). This is unphysical, because higher turbulence levels should enhance mixing and increase the wake recovery. Therefore, the ambient turbulence intensity at hub height is set by changing the roughness height $z_0$ in equation (4.14) instead of $C_\mu$. Subsequently, the friction velocity $u_*$ is set using equation (4.13), such that the correct undisturbed hub height velocity is obtained. The changes in the streamwise velocity profile are relatively small, especially at heights in the rotor area. For example, by physical site inspection one could argue to use a roughness height of 3 cm in the Western wake case of Wieringermeer (case 1 from Table 4.2). The relative difference between the velocity profile using a roughness height of 3 cm and the roughness height calculated by the alternative way of controlling the turbulence level: $z_0=0.44$ cm is less than 0.1%, 2% and 5% at 120, 40 and 20 m, respectively. In addition, there is often a high uncertainty in calculating the roughness from field measurements, which can be much larger than the difference in the turbulence adapted $z_0$. Furthermore, the measured velocity profile close to the ground is often influenced by local roughness variations that are not considered in the CFD simulations that use a uniform roughness height. It should be noted that the turbulent adapted $z_0$ can cause large differences in the velocity profile, for a case with a very low measured ambient turbulence intensity, located at a site with relatively large roughness. In this situation, the turbulent adapted $z_0$ can become orders of magnitude smaller than the $z_0$ from site inspection. However, it is most likely that in such a measurement, the ambient turbulence intensity is dictated by a stable ABL instead of the roughness height. These flows cannot be simulated with the current $k$-$\varepsilon$-$f_P$ EVM, since it is calibrated for a neutral ABL in which the shear parameter $\tilde{\sigma}$ is a constant.

**Grid refinement study**

The influence of the grid size on the flow solution for an AD in a uniform flow has been previously investigated in the work of Réthoré et al.[48] This work was meant to verify the numerical procedure of the AD as implemented in EllipSys3D, by estimating the (mixed) order of the discretization error.[53] Therefore, the grid study was performed such that all the individual components are at least second order accurate, i.e., a low Reynolds number was used such that a (low order) turbulence model is redundant. In addition, an analytical quadratic force distribution on the AD was used that made the behavior of the discretization error of the integrated force distribution second order accurate. From the mixed order analysis, Réthoré et al. showed that the AD method in EllipSys3D is still

first order accurate.[48] In the grid study of the present research, the goal is to the estimate the discretization error of a more realistic setup, i.e., including a real wind turbine blade force distribution on the AD, applying a shear and using a high Reynolds number ($Re_D \sim 10^7$) that requires a turbulence model. It should be noted that the EllipSys3D AD method corrects for errors in the integrated force that arise from the discretization of the force distribution. Hence the same total force is used in each grid level, although distributed differently. One could argue that the use of a grid-independent total force is wrong, since a grid study of the same flow problem including the rotor geometry would have a total force that is dependent on grid size. On the other hand, one could claim that having a grid-independent total force is a feature of the AD method since it allows the use of coarser grids, which is the reason to use an AD in the first place.

The grid layout in the grid study is similar to the one presented in Figure 4.6, but the streamwise extent of the wake domain is chosen to be 10D in order to reduce the amount of cells. The number of cells in each grid level is given in Table 4.3. A refinement ratio of two is used.

Table 4.3: Computational grid size.

| Grid level | Cells per rotor diameter in wake domain | Cells |
|---|---|---|
| 1 | 32 | 9830400 |
| 2 | 16 | 1228800 |
| 3 | 8 | 153600 |
| 4 | 4 | 19200 |

The normalized momentum deficit at hub height $\left\langle U_{def}^2 \right\rangle$ taken from a volumetric horizontal straight section $V$ is used to compare the solution on the different grid levels. $\left\langle U_{def}^2 \right\rangle$ is defined as:

$$\left\langle U_{def}^2 \right\rangle \equiv \frac{1}{U_{H,\infty}^2 V} \int_V \left(U_{H,\infty} - U(x,y,z)\right)^2 dV, \tag{4.15}$$

where the normalization is carried out with the undisturbed hub height velocity $U_{H,\infty}^2$, and the integration volume $V$ has dimensions $(\Delta x, \Delta y, \Delta z) = (0.5D, 3D, 0.5D)$. The comparison criterion is computed at three downstream distances from the AD: 2.5D, 5D and 7.5D. In order to make a fair comparison between the grid solutions, only cell-centered values are used within the volume $V$. The discretization error $\varepsilon_n$ of each grid level $n$ is estimated using a mixed order analysis:[53]

$$\varepsilon_n = f_n - f_{h\to 0} = g_1 h_n + g_2 h_n^2 + g_3 h_n^3 + \mathcal{O}(h_n^4), \tag{4.16}$$

where $f_n$ is the grid solution, $f_{h\to 0}$ is the extrapolated solution for an infinitely small grid size $h_n$, and $g_1, g_2, g_3$ are the unknown constants to be evaluated. The finest grid size

($n = 1$) is set to unity ($h_1 = 1$), and the coarser grid sizes are defined as ($h_{n+1} = rh_n$), with $r$ as the refinement ratio. Using the momentum deficit $\left\langle U_{def}^2 \right\rangle$ from equation (4.15) computed at the four grid levels of Table 4.3, the discretization error can be estimated by disregarding fourth order errors $\mathcal{O}(h_n^4)$ and solving the corresponding closed system. The first order ($g_1 h_n$), second order ($g_2 h_n^2$) and third order ($g_3 h_n^3$) contributions to the total discretization error can now be investigated.

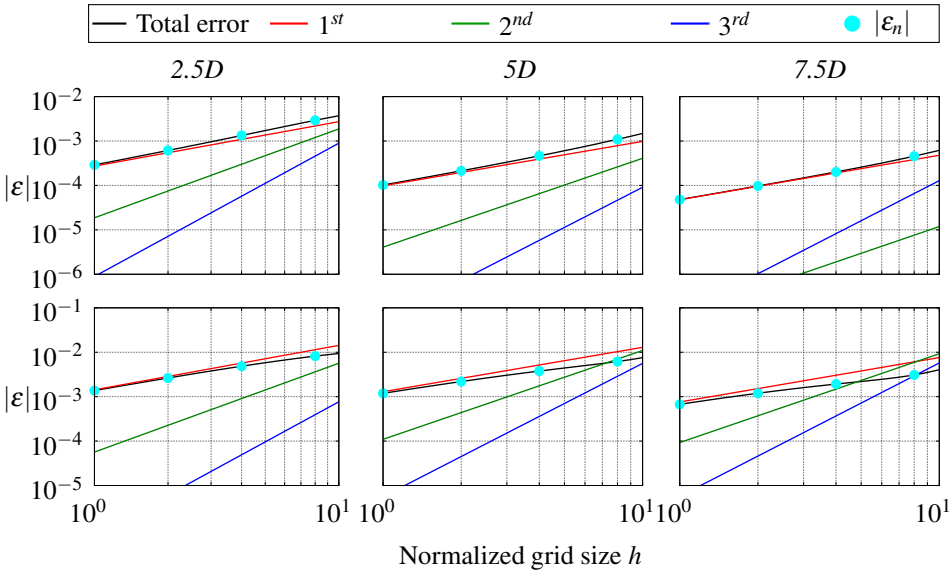


Figure 4.7: Order decomposition. Top row: $k$-$\varepsilon$ EVM. Bottom row: $k$-$\varepsilon$-$f_P$ EVM.

The grid study is performed for the $k$-$\varepsilon$ EVM and the $k$-$\varepsilon$-$f_P$ EVM using case 1 (Wieringermeer, see Table 4.2). The discretization error and its first order, second order and third order contributions are plotted in Figure 4.7 at downstream distances of 2.5D, 5D and 7.5D. The $k$-$\varepsilon$ EVM shows a very small discretization error. Even for the coarsest grid size the discretization error in terms of momentum deficit is smaller than 1% at all three downstream distances. The $k$-$\varepsilon$-$f_P$ EVM, simulated with the original Rotta constant $C_R = 1.8$, is more sensitive to the grid size, although all errors are still below 1%. Note that higher values of $C_R$ (as motivated in Section 4.4.2.2) will have discretization errors closer to the ones of the $k$-$\varepsilon$ EVM, since the high gradients at the edge of the wake decrease with $C_R$. The decomposition of errors shows that the linear contribution is the dominant term in the discretization error for both turbulence models. The relative low mixed order is caused by the AD method, which is first order near the AD,[48] and it is possibly degraded by the turbulence model further downstream from the AD.

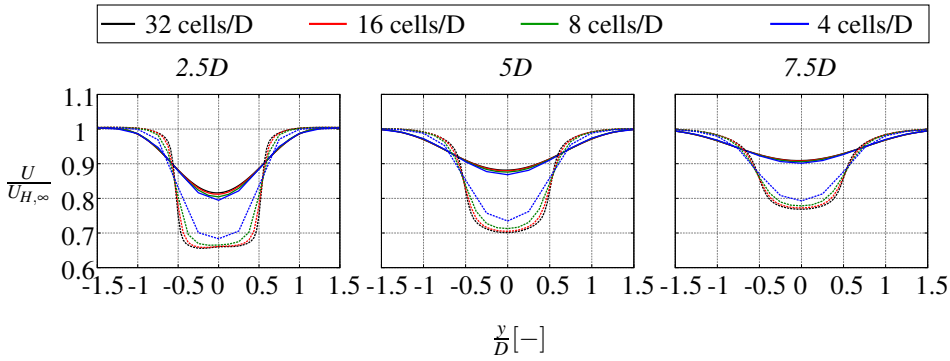


Figure 4.8: Wake deficit for different grid sizes with $D = 80$ m, $U_{H,\infty} = 10.7$ m/s, $I_{H,\infty} = 8\%$. Solid lines: $k$-$\varepsilon$ EVM. Dashed lines: $k$-$\varepsilon$-$f_P$ EVM with $C_R = 1.8$.

The velocity deficit at the same three downstream distances is shown in Figure 4.8. The deficit is extracted on a horizontal line at hub height, hence, an interpolation between the nearest cell centers is inevitable, which makes it difficult to compare in absolute numbers. Nevertheless, the trends can be compared. The wake deficit in the $k$-$\varepsilon$ EVM is not very sensitive to the used grid sizes, as observed before in mixed error analysis. However, the $k$-$\varepsilon$-$f_P$ EVM shows larger deviations between grid solutions, especially for the coarsest grid (four cells per rotor diameter in the wake domain). This is mainly caused by the fact that $k$-$\varepsilon$-$f_P$ EVM predicts higher velocity gradients at the edge of wake compared with the standard $k$-$\varepsilon$ EVM. The second coarsest grid (eight cells per rotor diameter in wake domain) shows only small deviations from the two finer grids. Therefore, it is recommended to use at least eight cells per rotor diameter in the wake domain when using the $k$-$\varepsilon$-$f_P$ EVM for wake simulations.

#### 4.4.1.2 LES

The LES simulations are employed using the same AD as used in the RANS simulations, and it is positioned in an equally sized domain. Figure 4.9 shows the grid where one in every eight nodes is plotted. The atmospheric turbulence is pre-calculated with the Mann model,[35] and the results are scaled such that the correct total turbulence intensity, averaged at a cross section of 2D $\times$ 2D located in front of the wind turbine, is obtained. In this way, the same turbulent kinetic energy is felt by the wind turbine in the LES and in the RANS simulations. The domain of the Mann turbulence box is long enough to be able to describe one hour of turbulence plus the start up time of the LES simulation (which is disregarded when average results are calculated). The cross section of the Mann turbulence box is 8D $\times$ 8D, and a uniform spacing with cell size D/8 is used in all directions. During the simulation the Mann turbulence is injected in a plane at 1.5D

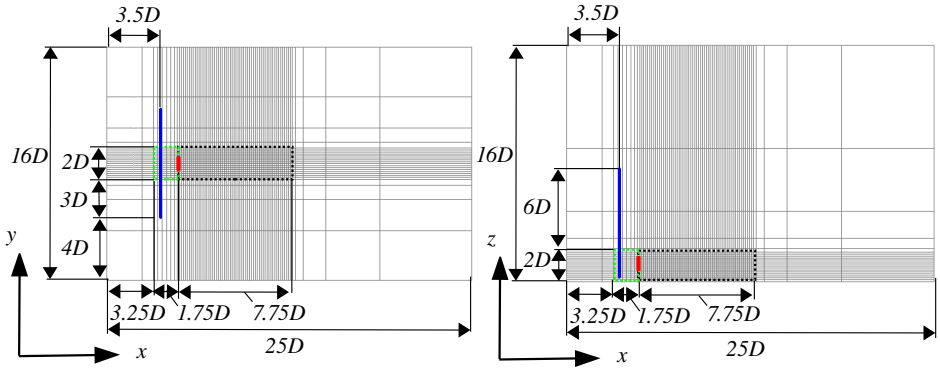


Figure 4.9: Computational domain LES. Left: top view. Right: side view. Dashed boxes: black is the wake domain and green marks the Mann turbulence domain. Actuator disk is illustrated as a red filled box. The inflow plane of Mann turbulence is shown as blue filled line. One in every eight nodes is shown.

upstream of the AD. The injection plane is $8D$ wide, centered around the AD, and it is extending $8D$ from the ground. This method is discussed in more detail in the work of Troldborg et al.[69,71] Two refined domains are defined in the flow domain: the wake domain $7.75\text{D} \times 2\text{D} \times 2\text{D}$ and the Mann turbulence domain $1.75\text{D} \times 2\text{D} \times 2\text{D}$. In order to reduce the amount of cells, the wake domain in the LES simulations is smaller compared with the RANS simulations; however, it is still large enough to capture the wake up to 7.5D downstream. The wake domain is uniformly discretized with a cell size of D/60 in all directions, which is sufficient to resolve the wake.[70] The Mann turbulence domain is discretized with a cell size of D/30 in the streamwise direction, and it inherits the grid spacing from the wake domain for the other two directions. Note that there is smooth transition of cell size between the Mann turbulence domain and the Wake domain. The total domain consists of 17.7 million cells. The bottom boundary at $z = 0$ is modeled as a slip wall, which allows a first cell height equal to the uniform grid spacing in the wake domain, which saves many cells compared with wall-resolved LES. The inlet conditions of the RANS simulations are also used in the LES simulations; however, a constant velocity of $u = u_*/\kappa \ln((z_H/10)/z_0)$ is set for $0 \leq z \leq z_H/10$ to comply with the slip wall. The rest of the boundaries are the same as used in the RANS simulations. Details of the numerical methods of the LES implementation are described in the work of Bechmann.[7]

In order to maintain the log law solution of the neutral ABL in a LES simulation without a rough wall boundary, one could add small body forces in the entire domain.[71] However, it is not expected that the log law solution decays significantly in reasonable vicinity of the AD, i.e., 7.5D downstream. In the current method the additional body forces are not included.

Even though the LES simulation is resolved in time, a constant forcing on the AD is applied. However, in terms of averaged wake deficit, a LES simulation using a constant force does not differ that much from one where time dependent forces are used.[46]

The length of LES simulation is set such that one hour of converged data is gathered. The time integration in EllipSys3D is implicit, allowing the user to set very high CFL numbers. Nevertheless, the time step $dt$ is set to a Courant-Friedrichs-Lewy number of one, i.e., $dt = dx/U_{H,\infty} = (D/60)/U_{H,\infty}$, such that the unsteady data is captured with a high resolution.

#### 4.4.1.3 Calibration of $C_R$

The $C_R$ parameter that is present in the $k$-$\varepsilon$-$f_P$ EVM determines the wake deficits completely. In order to choose the right value of $C_R$, a calibration is carried out against the LES using the eight test cases that are described in Section 4.3. The wake deficit at hub height, at the wake center (relative wind direction of 0°), at a downstream distance of 7.5D, is used to measure how well the $k$-$\varepsilon$-$f_P$ EVM performs compared with LES. The results are shown in Figure 4.10 in which the relative error $\varepsilon_U$ of the wake deficit at the center at 7.5D is calculated as follows:

$$\varepsilon_U = \frac{U_{RANS} - U_{LES}}{U_{LES}}. \tag{4.17}$$

In Figure 4.10 the error bars represent the uncertainty of the LES results, i.e., the stan-

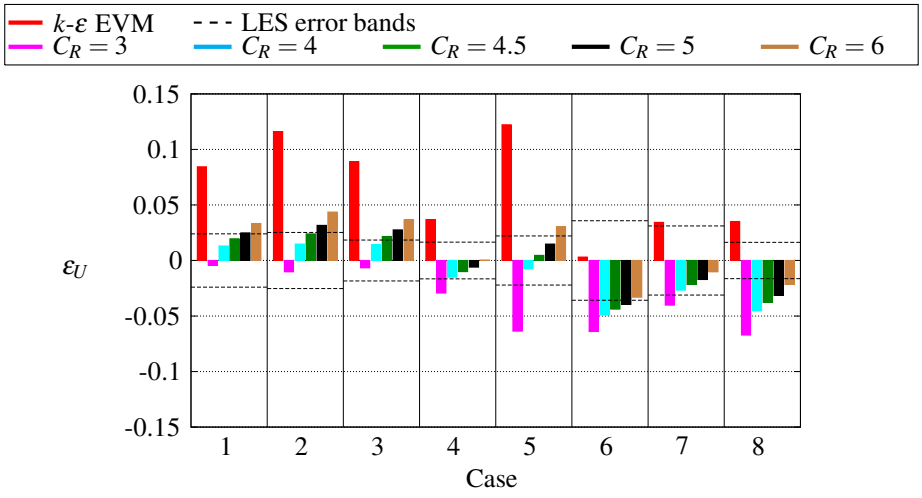


Figure 4.10: Calibration $C_R$.

dard deviations. In first seven cases, the wake center at 7.5D calculated by the $k$-$\varepsilon$-$f_P$

EVM fits well LES when using $C_R = 4.5$. In case 6, representing a case with a very high undisturbed turbulence intensity, the $k$-$\varepsilon$ EVM performs better than the $k$-$\varepsilon$-$f_P$ EVM at the far wake, although the result of the $k$-$\varepsilon$-$f_P$ EVM with $C_R = 4.5$ does not exceed the standard deviation of LES significantly. Case 8 shows that for a high thrust coefficient both the $k$-$\varepsilon$ EVM and the $k$-$\varepsilon$-$f_P$ EVM with $C_R = 4.5$ do not compare well with LES at 7.5D, however, both models have a comparable magnitude of $\varepsilon_U$.

### 4.4.2 Results and Discussion

The results of the test cases based on measurements and the results for the test cases based on LES are shown in Figures 4.11 and 4.12, respectively. The velocity wake deficit at hub height is plotted against the relative wind direction for a number of downstream locations. For the test cases based on measurements, the locations are chosen to match the measured ones. For cases 1, 2 and 4, extra downstream locations are shown for comparison of the RANS results with the ones of LES. Note that downstream locations for test case 4 are normalized with $D^* = 40$ m instead of the real rotor diameter ($D = 41$ m) to comply with the normalization distance of the measurements. The wake deficit for test cases that are not based on measurements are plotted at 2.5D, 5D and 7.5D. For two of these cases (cases 5 and 6) the turbulence intensity at hub height is given in Figure 4.13. The results are shown for the $k$-$\varepsilon$ EVM, the $k$-$\varepsilon$-$f_P$ EVM with $C_R = 4.5$, LES and measurements. If available, the measurements are presented with error bars representing one standard deviation. The 1 h LES simulations are averaged by using six bins of 10 min. The standard deviation of the six bins are shown as error bars. For each case, the results of LES are normalized with the undisturbed hub height velocity taken from another LES simulation with the same setup but without using the AD. It has been found that in the case with a high undisturbed turbulence intensity (case 6), the undisturbed hub height velocity at 7.5D deviates around 2% from the one that is imposed at the inlet. For all other cases, the difference is much less, typically below 1%. A comparison of LES with measurements is given in Sections 4.4.2.1 and 4.4.2.2, respectively.

#### 4.4.2.1 LES compared with measurements

In the Western wake case from Wieringermeer (case 1), shown in Figure 4.11, the results of LES compare well with the available field measurements at 3.5D. Note that there is a clear offset of around 5°in the measured wake center, which is probably caused by yaw error, as also discussed in the work of Schepers et al.[57] The measurement of the Eastern wake case from Wieringermeer (case 2) compares reasonably well with the wake deficit predicted by LES; however, the magnitude of the maximum wake deficit is underpredicted by LES. Possible causes for the underpredicted wake deficit are effects of atmospheric stability on the measured wake deficit or the uncertainty in the prediction

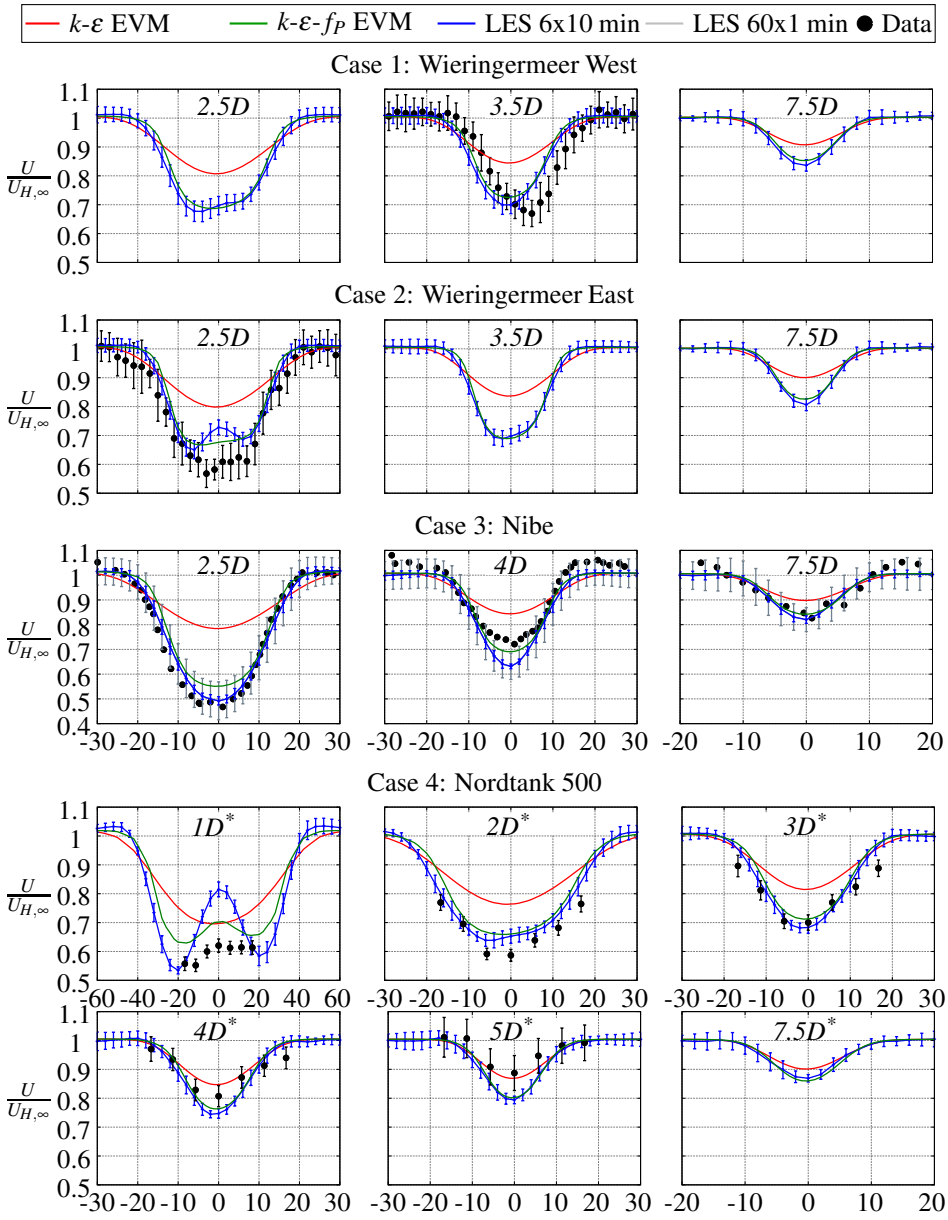


Figure 4.11: Test cases based on field measurements. The measurements and the LES results include error bars of one standard deviation. $C_R = 4.5$ in $k$-$\varepsilon$-$f_P$ EVM.

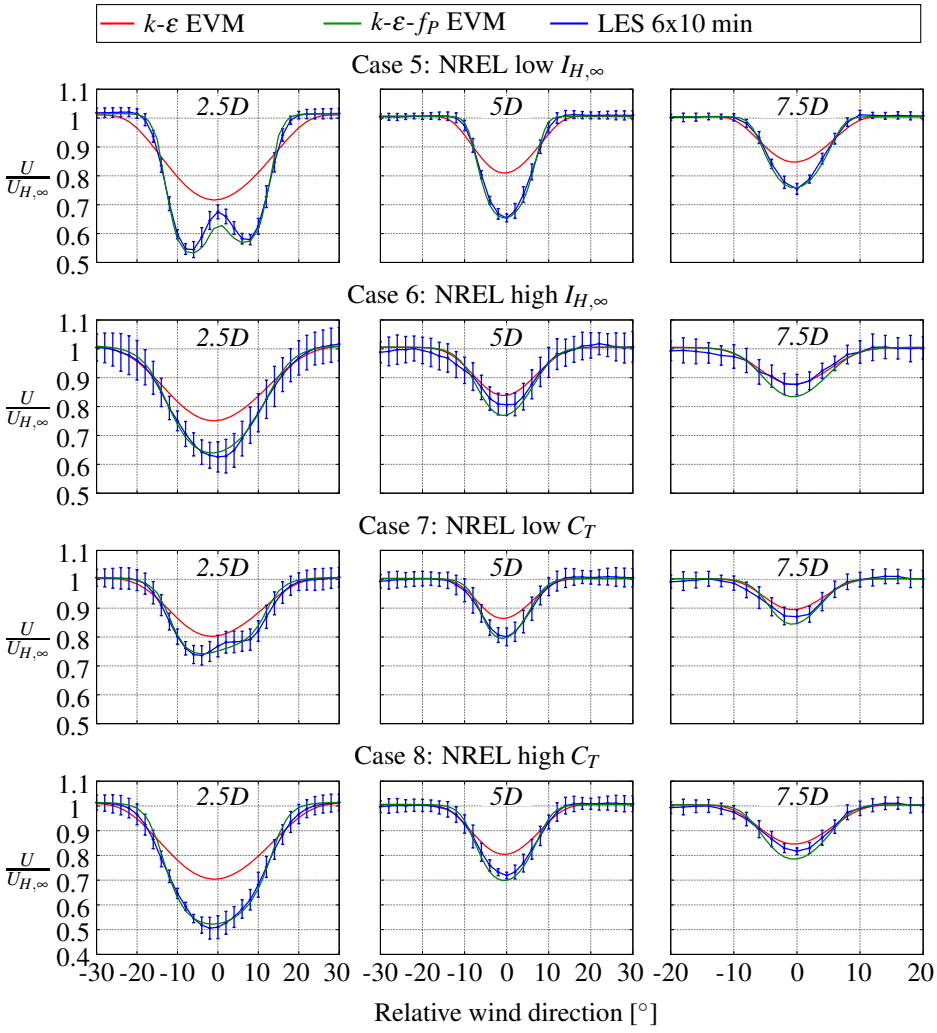


Figure 4.12: Additional test cases based on LES. The LES results include error bars of one standard deviation. $C_R = 4.5$ in $k$-$\varepsilon$-$f_P$ EVM.

of the measured undisturbed turbulence intensity due to the lack of upstream measurements. The measured and the calculated wake deficit is asymmetric in the near wake (best visible in case 2), which is caused by the interaction of wake rotation with a vertical shear, a phenomenon that is discussed in more detail in the work of Zahle and Sørensen.[81]

In the Nibe case (case 3) two different LES results are shown in Figure 4.11: one with an average taken from of six bins of 10 mins and one with an averaging take from sixty bins of 1 min. Since the measured wake deficit is processed with 1 min averages it should be compared with the averaged LES results from the same bin length. The LES results for the 10 min bins are used to compare with RANS, as discussed in Section 4.4.2.2. A clear consequence of using one min bins is the increase of the standard deviations compared with 10 min bins. This gives an idea of how large the standard deviations of the measurements can be. The measured wake deficit compares well with the results of LES at 2.5D and 7.5D. At 4D, the calculated wake deficit is slightly overpredicted compared with the measured one. However, assuming similar standard deviations for the measurements as observed in the LES results, obtained from 1 min bins, the difference falls within the error bars. In addition, since the estimate of the undisturbed turbulence intensity in the measurements is very uncertain, as explained in Section 4.3.2, it is difficult to compare the measurements with LES.

The lidar measurements of the Nordtank 500 wind turbine (case 4) shows a similar trend in the wake deficits as the ones calculated with LES. However, at $1D^*$ the measurements do not show the clear double bell-shaped wake deficit as observed in LES. The AD method is least accurate in the near vicinity of the wind turbine and can explain the difference. For example, the forces of the nacelle are not present in the force distribution of the AD, and it can lead to a smaller wake deficit at the center of wake in AD simulations compared with the measurements. In addition, the measured wake deficit at $5D^*$ is more recovered compared with the one calculated by LES, which is not fully understood. The uncertainty in the undisturbed turbulence intensity, terrain effects or large scale meandering are plausible causes for the difference in the wake recovery.

#### 4.4.2.2 RANS compared with LES

Compared to LES, the wake deficit is underpredicted by the original $k$-$\varepsilon$ EVM for all test cases at all downstream distances, as shown in Figures 4.11 and 4.12, except for cases 6 and 7 at the far wake. These cases correspond to a high undisturbed turbulence intensity and low thrust coefficient. The $k$-$\varepsilon$ EVM performs the worst for a high thrust coefficient (cases 3 and 8) and for a low turbulence intensity (cases 2 and 5), because the velocity gradients at the edge of the wake are the highest in these cases.

All cases show that the near wake deficits calculated by $k$-$\varepsilon$-$f_P$ EVM, are much closer to the ones of LES, compared with the ones of the original $k$-$\varepsilon$ EVM. The largest improvement in the near wake deficits is obtained for the cases with a low turbulence intensity and a high thrust coefficient.

In the work of Réthoré,[46] it has been found that the $k$-$\varepsilon$ EVM overestimates the turbulence intensity of the wake. A similar result for the case with a low undisturbed turbulence intensity (case 5) at 2.5D is shown in Figure 4.13. In this case, the turbulence intensity predicted by $k$-$\varepsilon$-$f_P$ EVM is more comparable with LES; however, at 7.5D

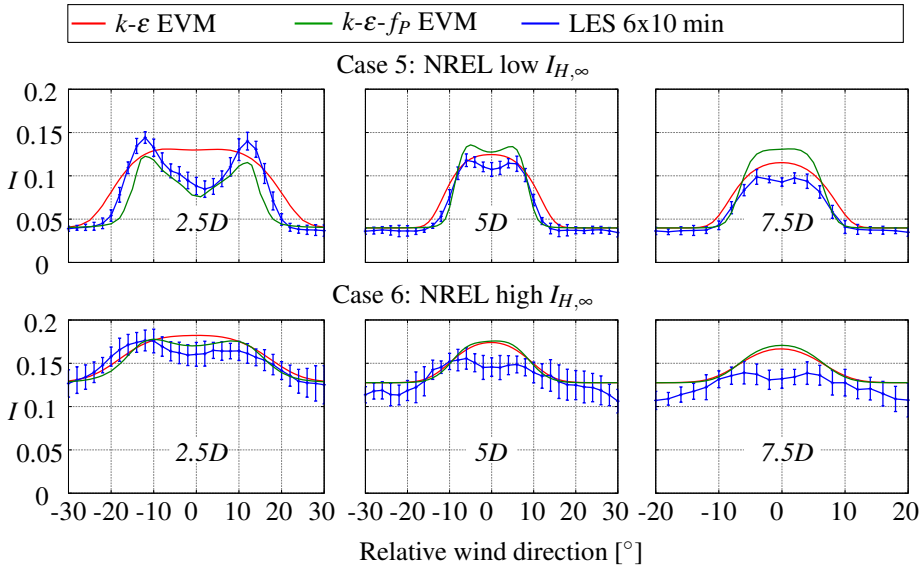


Figure 4.13: Turbulent intensity $I = \sqrt{2/3k}/U_{H,\infty}$ for test cases 5 and 6. The LES results include error bars of one standard deviation. $C_R = 4.5$ in $k$-$\varepsilon$-$f_P$ EVM.

both EVMs overpredict the turbulence intensity. In the high turbulence case (case 6), the same conclusion can be made but the difference between RANS and LES is smaller than seen in case 5 because of the high level of background turbulence. Note the calculated turbulence intensity in the LES deteriorates outside the wake domain (relative wind directions larger than $\approx \pm 10\,^{\circ}$at 7.5D) because the of increasing cell size.

#### 4.4.2.3 Computational cost

The computational effort of the simulations of all test cases are given in Table 4.4. All simulations are carried out on the same cluster; however, a different number of nodes have been used as follows: fifteen for LES and three for RANS simulations, except for case 5, which has been calculated with five nodes for the RANS simulations. Each node has two Intel Xeon X5650 processors with six cores each that have a clock frequency of 2.66 GHz. In most cases, the LES simulations are approximately $10^3$ computationally more expensive compared with the RANS simulations The RANS simulations of case 5 are computationally more expensive because the low turbulence intensity is represented by a very low roughness. Hence, more cells are necessary in the grid, and the convergence of the numerical scheme is slowed down. The large grid and the simulation time that is needed to gather enough unsteady data makes the LES very expensive, especially

Table 4.4: Computational effort in CPU hours of the single wake simulations.

| | LES | RANS $k$-$\varepsilon$ | RANS $k$-$\varepsilon$-$f_P$ ($C_R = 4.5$) |
|---|---|---|---|
| case 1 | 5360 | 4.2 | 4.6 |
| case 2 | 5341 | 3.3 | 3.5 |
| case 3 | 11036 | 3.0 | 3.9 |
| case 4 | 10559 | 3.5 | 4.1 |
| case 5 | 2749 | 25 | 28 |
| case 6 | 2743 | 5.7 | 5.6 |
| case 7 | 2747 | 3.9 | 5.2 |
| case 8 | 2784 | 4.0 | 5.4 |

when a small wind turbine is used which limits the time step (time step is proportional to the rotor diameter). The difference in computational effort between the two RANS turbulence models is negligible. Note that the comparison is only a rough estimate since a different number of nodes are employed for the LES and the RANS simulations. In addition, the cluster is also used by others, which can influence the effective computational effort.

## 4.5 Conclusions

A modified $k$-$\varepsilon$ EVM with a flow-dependent $C_\mu$ (called $C_\mu^*$) is proposed: the $k$-$\varepsilon$-$f_P$ EVM. $C_\mu^*$ decreases the eddy viscosity in regions with high velocity gradients, e.g., in a wind turbine wake. The impact of $C_\mu^*$ on the flow solution is controlled by a parameter $C_R$, which is calibrated against LES for eight different single wake cases. From the calibration, it is recommended to use $C_R = 4.5$. Four of the eight test cases are based on measurements, and their results compare reasonably well with LES. However, the comparison with measurements is limited because the uncertainty in the undisturbed turbulence intensity is large and the effects of stability are not filtered out for three of four measured wake cases.

A grid refinement study shows that the $k$-$\varepsilon$-$f_P$ EVM is more sensitive to grid size compared the original $k$-$\varepsilon$ EVM. Nevertheless, both turbulence models show discretization errors below 1% for a grid spacing of D/8 in the wake region.

Where the original $k$-$\varepsilon$ EVM underpredicts the velocity wake deficit compared with LES and measurements, the $k$-$\varepsilon$-$f_P$ EVM shows more comparable results with respect to LES, for seven of the eight wake cases. These improvements are mainly observed for the test cases in which $k$-$\varepsilon$ EVM has the worst performance, i.e., a low turbulence intensity and a high thrust coefficient. On the contrary, the test case with a high (total) turbulence intensity (12.8%) shows that the wake recovery of LES is closer to the original $k$-$\varepsilon$ EVM. However, in the near wake the $k$-$\varepsilon$-$f_P$ EVM is superior to the $k$-$\varepsilon$ EVM for all eight cases.

The fact that the $k$-$\varepsilon$-$f_P$ EVM is approximately $10^3$ computationally less expensive than LES, and it has the same numerical stability as the original $k$-$\varepsilon$ EVM, makes the $k$-$\varepsilon$-$f_P$ EVM an attractive turbulence model, which has the potential to simulate wake effects on the power production of wind farms.

## Acknowledgments

This work is supported by the Center for Computational Wind Turbine Aerodynamics and Atmospheric Turbulence funded by the Danish Council for Strategic Research, grant number 09-067216. Computational resources were provided by DCSC and the DTU central computing facility.

# 5

# PAPER II: THE $k$-$\varepsilon$-$f_P$ MODEL APPLIED TO DOUBLE WIND TURBINE WAKES USING DIFFERENT ACTUATOR DISK FORCE METHODS


## Abstract

The newly developed $k$-$\varepsilon$-$f_P$ eddy viscosity model is applied to double wind turbine wake configurations in a neutral atmospheric boundary layer, using a Reynolds averaged Navier-Stokes solver. The wind turbines are represented by actuator disks. A proposed variable actuator disk force method is employed to estimate the power production of the interacting wind turbines and the results are compared with two existing methods; a method based on tabulated airfoil data and a method based on the axial induction from 1D momentum theory. The proposed method calculates the correct power, while the other two methods overpredict it. The results of the $k$-$\varepsilon$-$f_P$ eddy viscosity model are also compared with the original $k$-$\varepsilon$ eddy viscosity model and large-eddy simulations. Compared to the large-eddy simulation-predicted velocity and power deficits, the $k$-$\varepsilon$-$f_P$ is superior to the original $k$-$\varepsilon$ model.


## 5.1 Introduction

In modern wind farms, the interaction of wind turbine wakes can cause annual energy losses of 10 to 20%.[6,24] In addition, the wake turbulence increases the loading on the wind turbine blades, which may lead to premature failure. Wind turbine wake interaction has been studied numerically by many authors, using models that range from simple engineering wake models, such as the N.O. Jensen model,[25] to high fidelity computational fluid dynamics (CFD) methods, including large-eddy simulations (LES).[13,69] Reynolds-averaged Navier-Stokes (RANS) solvers use a CFD method that is roughly three orders cheaper than the LES.[76] In contradiction to LES, in which the large scale turbulence is resolved in time and only the small turbulent scales are modeled, a RANS method

This chapter has been published as: van der Laan, M. P., Sørensen, N. N., Réthoré, P.-E., Mann, J., Kelly, M. C. and Troldborg, N. The $k$-$\varepsilon$-$f_P$ model applied to double wind turbine wakes using different actuator disk force methods. *Wind Energy*, Accepted in September, 2014.

models the averaged turbulent quantities completely, in a steady-state simulation. Many authors[10,16,45,46,76] have employed the widely used $k$-$\varepsilon$ eddy viscosity model (EVM) to model the turbulence in RANS. Their work shows that $k$-$\varepsilon$ EVM underpredicts the velocity deficit of a single wind turbine. To overcome this problem, an extended $k$-$\varepsilon$ EVM, called the $k$-$\varepsilon$-$f_P$ EVM was developed[76] based on the work of Apsley and Leschziner.[2] The $k$-$\varepsilon$-$f_P$ EVM has a variable $C_\mu$, instead of the constant $C_\mu$, used in the original $k$-$\varepsilon$ EVM. The varying part of $C_\mu$ is defined by the scalar function $f_P$, which is only dependent on local velocity gradients. The variable $C_\mu$ has lower values compared to the constant $C_\mu$ in regions where the velocity gradients are high, e.g. the edge of a wind turbine wake. As a result, the turbulent eddy viscosity in the wake is much lower in $k$-$\varepsilon$-$f_P$ EVM compared to the original $k$-$\varepsilon$ EVM. Therefore, the $k$-$\varepsilon$-$f_P$ EVM predicts a larger velocity deficit than the $k$-$\varepsilon$ EVM. The $k$-$\varepsilon$-$f_P$ EVM includes a parameter $C_R$ that controls the velocity deficit completely, so $C_R$ should be chosen with care. In previous work,[76] $C_R$ is calibrated with the velocity deficit predicted by LES, for eight different single wind turbine wake cases. It should be noted that the $k$-$\varepsilon$-$f_P$ EVM can only model isotropic turbulence, and thus cannot predict the anisotropic Reynolds-stresses present in LES and field measurements.

In the present paper, the $k$-$\varepsilon$-$f_P$ EVM is applied to two closely spaced wind turbines for different orientations. The wind turbine geometry is not physically modeled; instead, the rotor forces are represented by an actuator disk (AD).[37,46,48] The AD acts as a momentum source term in the Navier-Stokes equations. Troldborg et al.[72,73] showed that as long as the AD is subjected to ambient atmospheric turbulence, the averaged velocity deficit calculated by the AD is similar to that from a CFD simulation in which the full rotor geometry is represented. When multiple ADs are used to simulate wake interaction in wind farms, the force on each AD is not known prior to the simulation. Therefore, it is necessary to have a method for prescribing AD forces that vary during the simulation. In the literature, several variable AD force methods are used;[11,16,45,48,79] however, it is not clear how these methods compare with each other. The AD forces strongly influence the flow solution, hence it is important to correctly model them. The main aim of the present paper is to find the best setup for simulations of interacting ADs in RANS, which can be used for wind farm simulations in future work. To reach this goal, one new variable AD force method is proposed in Section 5.2.2 and it is compared with two existing variable AD force methods, for a single and a double wind turbine setup, in Sections 5.4.2.1 and 5.4.2.2, respectively. The velocity deficit calculated by the $k$-$\varepsilon$-$f_P$ EVM applied to two wind turbines, is compared with results of the standard $k$-$\varepsilon$ EVM and LES, in Section 5.4.2.3. In this exercise, the AD forces are kept constant, such that only the turbulence models are compared. In Section 5.4.2.4, one variable AD force method is used to compare the $k$-$\varepsilon$-$f_P$ EVM with the standard $k$-$\varepsilon$ EVM and LES, in terms of the power deficit. An overview of the comparisons is given in Table 5.1. The three variable AD force methods (Methods I-III) are discussed in Section 5.2 and the individual test cases (cases 1-7) are described in Section 5.3.

Table 5.1: Overview of comparisons.

| Section | Wake(s) | Test case(s) | Variable AD force method(s) | Turbulence model(s) |
|---|---|---|---|---|
| 5.4.2.1 | single | 1 | Methods I-III | $k$-$\varepsilon$-$f_P$ EVM |
| 5.4.2.2 | double | 6-7 | Methods I-III | $k$-$\varepsilon$-$f_P$ EVM |
| 5.4.2.3 | double | 2-5 | None | $k$-$\varepsilon$ EVM, $k$-$\varepsilon$-$f_P$ EVM and LES |
| 5.4.2.4 | double | 6-7 | Method I | $k$-$\varepsilon$ EVM, $k$-$\varepsilon$-$f_P$ EVM and LES |

## 5.2 Force treatment for multiple actuator disks

The wind turbine geometry is not present in the flow simulations. Instead, the rotor forces are modeled with an AD.[37,46,48] The AD acts as a momentum sink in the Navier-Stokes equations. The force loading of AD determines the amount of momentum that is extracted from the flow and is therefore very important in wind turbine wake simulations, that are modeled with ADs. Different types of AD loading are proposed in the literature. The most simple approach is a uniformly distributed loading, in which only the total amount of the normal force $F_N$ is modeled, and it is kept constant during the simulations:[10,46]

$$F_N = \frac{1}{2}\rho C_T A U_{H,\infty}^2, \tag{5.1}$$

with $\rho$ as the air density, $C_T$ as the thrust coefficient, $A = \pi R^2$ as the rotor area with $R$ as the blade radius and $U_{H,\infty}$ as the free-stream velocity at hub height. In addition, one could add a uniformly distributed tangential force component, in which the total magnitude is determined by the torque $\tau$:

$$\tau = \frac{P}{\Omega} = \frac{\frac{1}{2}\rho C_P A U_{H,\infty}^3}{\Omega}, \tag{5.2}$$

where $P$ is the wind turbine power, $\Omega$ is the rotational speed in radians per second and $C_P$ is the power coefficient. Instead of using a uniformly distributed normal and tangential force distribution, it is also possible to scale a reference blade force distribution with the parameters defined in equations (5.1) and (5.2). In previous work,[76] this method is used to scale the normal blade force distribution $q_N(r)$ and the tangential blade force distribution $q_T(r)$ of the NREL 5-MW reference wind turbine,[26] to represent rotor forces of different wind turbines. Note that $r$ is the radial coordinate of the blade. The normalized $q_N(r)$ and $q_T(r)$ of the NREL 5-MW reference wind turbine are plotted in Figure 5.1.

The scaling of the reference distribution is as defined in van der Laan et al.:[76]

$$q_N^{AD}(r) = \hat{q}_N(r)\frac{1}{n}\frac{1}{2}\rho U_{H,\infty}^2 \pi R^2 C_T, \qquad \hat{q}_N(r) = \frac{q_N(r)}{\int_0^R q_N(r)dr}, \tag{5.3}$$

$$q_T^{AD}(r) = \hat{q}_T(r)\frac{1}{n}\frac{\frac{1}{2}\rho U_{H,\infty}^3 \pi R^2 C_P}{\Omega}, \qquad \hat{q}_T(r) = \frac{q_T(r)}{\int_0^R q_T(r)rdr},$$

where the superscript AD denotes the scaled AD blade force distribution, $\hat{q}$ is a normalized blade force distribution and $n$ is the number of blades. The use of a reference blade force distribution implies that the shape of the blade force distribution (normalized by $0.5\rho R U_{H,\infty}^2$) should not change much with different free-stream velocities and different blades. The assumption might be violated for a wind turbine blade that is very different in geometry compared to the reference blade or if the simulated turbine operates at conditions far from those in which the reference loading was obtained. However, a similar assumption is made when tabulated airfoil data is used for the AD forces, to represent a wind turbine rotor from which the actual blade geometry and corresponding aerodynamics are unknown. This assumption is used by Porté-Agel et al.[44] and Churchfield et al.[13] In their work the AD forces of the Siemens SWT-2.3-93 wind turbine are modeled by using a newly designed wind turbine that mimics the known power production.

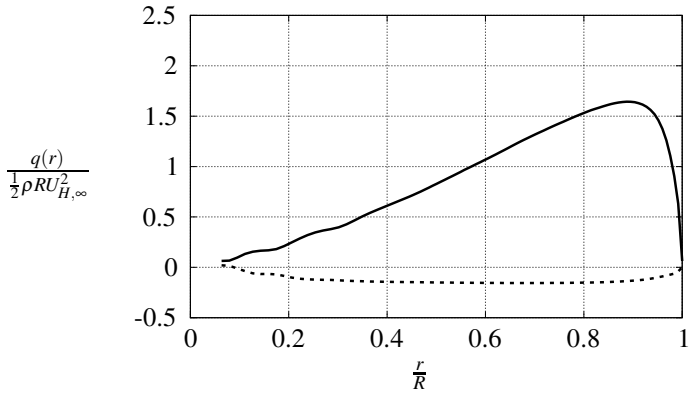


Figure 5.1: Calculated tangential $q_T(r)$ (dashed line) and normal force $q_N(r)$ (solid line) distributions.

The determination of the actuactor disk forces in multiple wake configurations is not trivial. In the cases where downstream ADs feel the velocity deficit of upstream ADs, the total force cannot be constant for all ADs. Instead, the downstream ADs that are positioned in the full wake of others should experience lower normal and tangential forces compared to those that are subject to the undisturbed flow.

When the AD loading is based on uniformly distributed forces, equations (5.1) and (5.2), or a scaled reference distribution, equation (5.3), information of the force scaling coefficients $C_T$, $C_P$, $\Omega$ and the free-stream velocity $U_{H,\infty}$ is necessary to obtain the correct total forces. $C_T$, $C_P$, $\Omega$ are often defined as function of $U_{H,\infty}$, hence, when $U_{H,\infty}$ is known for a particular AD, the corresponding AD forces can be determined. However, $U_{H,\infty}$ is not known for an AD that is in the lee of another. This problem is approached by a simple existing method and an alternative proposed method in Sections 5.2.1 and 5.2.2, respectively. In addition, another existing variable force method, in which tabulated airfoil data is used instead of a reference force distribution of Figure 5.1, is described in Section 5.2.3.

### 5.2.1 Method I: AD Induction Method

One could consider to estimate the free-stream velocity $U_{H,\infty}$ by the axial induction factor $a_x$ from 1D momentum theory, as performed in the work of Prospathopoulos et al.,[45] Calaf et al.[11] and used by Wu and Porté-Agel[79] for an AD model that does not include rotation (ADM-NR):

$$a_x = 0.5\left(1-\sqrt{1-C_T}\right), \tag{5.4}$$
$$U_{H,\infty} = \frac{\langle U_{AD}\rangle}{1-a_x},$$

with $\langle U_{AD}\rangle$ as the local velocity at the AD, averaged over the whole AD area $A$, which can be extracted from the flow field. Prior to the first iteration in CFD, $U_{H,\infty}$ is guessed based on the free-stream wind speed, which provides the scaling coefficients $C_T$, $C_P$ and $\Omega$, that determine the AD forces. After the first iteration, $\langle U_{AD}\rangle$ is probed at the AD, and a new $U_{H,\infty}$ is calculated with equation (5.4). Subsequently, the scaling coefficients and AD forces are updated. The iteration process is repeated until the forces are converged to a satisfactory level. Prospathopoulos et al.[45] proposed an extra empirical relation for $C_T(a_x)$ for large induction factors, $a_x > 0.4$, but in the current work, it is observed that the converged induction factor is never larger than 0.4. Note that Prospathopoulos et al. only used a uniformly distributed normal force, as defined by equation (5.1).

### 5.2.2 Method II: AD Variable Scaling Method

In the present research, an alternative variable force method is proposed. Using a calibration procedure of single wind turbine wake simulations, it is possible to calculate alternative scaling coefficients $C_T^*$, $C_P^*$ and $\Omega^*$ that represent $C_T$, $C_P$ and $\Omega$ as function of a local velocity average around the AD: $\langle U_{AD}\rangle$. The alternative scaling coefficients can be used to scale the AD forces dynamically during the simulation by probing $\langle U_{AD}\rangle$ at

the AD. In Method II, the scaled AD forces of equation (5.3) are defined as:

$$q_N^{AD}(r) = \hat{q}_N(r)\frac{1}{n}\frac{1}{2}\rho\langle U_{AD}\rangle^2 AC_T^*, \qquad (5.5)$$
$$q_T^{AD}(r) = \hat{q}_T(r)\frac{1}{n}\frac{\frac{1}{2}\rho\langle U_{AD}\rangle^3 AC_P^*}{\Omega^*},$$

Hence:

$$C_T^* = C_T\left(\frac{U_{H,\infty}}{\langle U_{AD}\rangle}\right)^2, \qquad C_P^* = C_P\left(\frac{U_{H,\infty}}{\langle U_{AD}\rangle}\right)^3 \qquad (5.6)$$

In the calibration procedure, 22 single wind turbine simulations for $4 \leq U_{H,\infty} \leq 25$ with equidistant intervals of 1 m/s are performed to determine $C_T^*$, $C_P^*$ and $\Omega^*$ as function of $\langle U_{AD}\rangle$. The numerical setup for the single wind turbine simulations is described in detail in the work of van der Laan et al.[76] and a summary is given in Section 5.4.1.1. In addition, a new calibration is carried out whenever the turbulence model or the ambient turbulence intensity is changed. The calibration of the NREL 5-MW wind turbine from Section 5.3 is shown in Figure 5.2. The calibrated scaling coefficients $C_T^*$, $C_P^*$ and $\Omega^*$ are plotted as a function of the averaged AD velocity $\langle U_{AD}\rangle$. Four different calibrations are given that differ in turbulence model and ambient turbulence intensity. The dependence of turbulence intensity on the calibration is very small, whereas the calibration is sensitive to the turbulence model. This sensitivity is caused by the difference in the predicted $\langle U_{AD}\rangle$, which is most visible in $C_T^*$ and $C_P^*$ in the low wind speed range. The effect is small for $\Omega^*$.

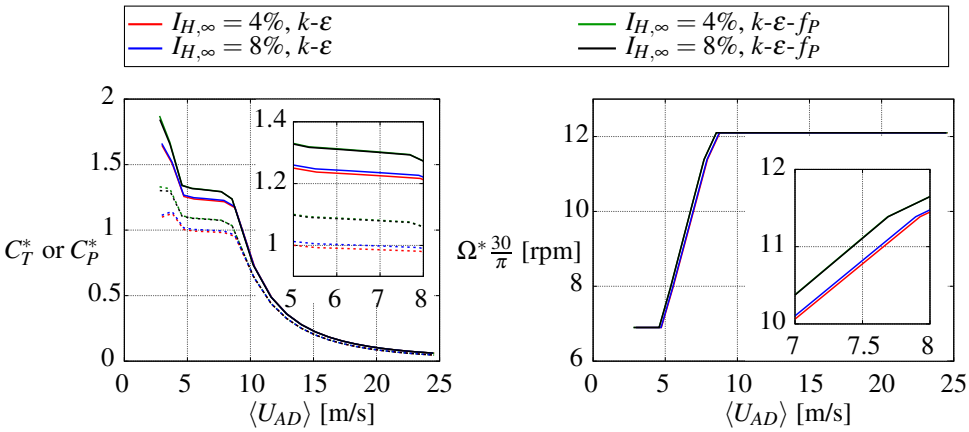


Figure 5.2: Calibration of NREL 5-MW wind turbine. Left: $C_T^*$ (solid line) and $C_P^*$ (dashed line). Right: rotational speed $\Omega^*$ in rpm.

The variable force method has been checked to assure that the correct power, thrust force and rotational speed are obtained, when the calibrated $C_T^*$, $C_P^*$ and $\Omega^*$ are used. The error in the power, thrust force and rotational speed are negligible, if the grid of the calibration procedure is the same as the one that is used to verification simulation. If the AD is moved in the grid of the verification simulation, with respect to the AD that was used for the calibration, the error in power is larger but still below 1%. These good results are achieved when the AD is placed in the cell centers.

### 5.2.3 Method III: AD Airfoil Method (with torque calibration)

A common method to represent the rotor forces on an AD is the use of tabulated airfoil data. This method is based on blade element momentum theory and it is introduced by Sørensen and Shen[61] for the actuator line technique. In later work, the method is used for AD simulations by El Kasmi and Masson,[16] Réthoré et al.,[48] Wu and Porté-Agel[79] and others. In the present work, the implementation of Réthoré et al.[48] is used, which can be summarized as:

$$
\begin{aligned}
&\text{Force vector:} && \mathbf{f} = \mathbf{L} + \mathbf{D} = \tfrac{1}{2}\rho U_{rel}^2 \tfrac{nc}{2\pi r} F (c_l \mathbf{e}_l + c_d \mathbf{e}_d),\\
&\text{Relative velocity:} && U_{rel} = \sqrt{U_x^2 + (\Omega r - U_\theta)^2},\\
&\text{Angle between } U_{rel} \text{ and rotor plane:} && \varphi = \tan^{-1}\left(\tfrac{U_x}{\Omega r - U_\theta}\right),\\
&\text{Angle of attack:} && \alpha = \varphi - \gamma,\\
&\text{Tip correction factor of Shen et al.:} && F = \tfrac{2}{\pi}\arccos\left(\exp\left[-gf\right]\right),\\
&\text{(with modified } c_2\text{)} && g = \exp\left(-c_1\left(n\lambda - c_2\right)\right) + c_3,\\
& && f = \tfrac{n}{2}\tfrac{R-r}{r\sin\varphi},\\
& && c_1 = 0.125, c_2 = 27, c_3 = 0.1.
\end{aligned}
\tag{5.7}
$$

The variables are defined on a cross sectional element at a radial blade coordinate $r$ in the $\theta$-$x$ plane, as shown in Figure 5.3. Note that $\theta$ is the azimuthal coordinate and $x$ is the axial coordinate. In equation (5.7), the force vector per unit area $\mathbf{f}$ is the sum of the lift force $\mathbf{L}$ and the drag force $\mathbf{D}$. The orientation of the lift and drag force is defined by the corresponding unit vectors $\mathbf{e}_l$ and $\mathbf{e}_d$, respectively. The force vector $\mathbf{f}$ depends on the density $\rho$, the relative velocity $U_{rel}$, the number of blades $n$, the chord length $c$, the radial location on the blade $r$ and the sectional lift and drag coefficients $c_l$ and $c_d$, respectively, taken from the tabulated airfoil data. The relative velocity $U_{rel}$ is defined from the velocity triangle, as sketched in Figure 5.3, which is a function of the axial velocity $U_x$, the rotational velocity $U_\theta$, the angular rotational speed $\Omega$ in radians per second and the radial coordinate $r$. $\varphi$ is the angle between $U_{rel}$ and the rotor plane that, together with the local pitch angle $\gamma$ (sum of the blade pitch angle and local twist), defines the local angle of attack $\alpha$. To account for a finite number of the blades, the tip correction of Shen et al.[58,59] used, in which $\lambda$ is the tip speed ratio, $R$ is the blade radius

and $c_i$ are empirical constants. Shen et al. determined the constants $c_i$ from a calibration with two small experimental wind turbine rotors that have a relatively blunt tip, leading to $c_2 = 21$. Troldborg[68] found that for modern large wind turbines with a sharp tip, $c_2$ should be set to 27, which will be adopted in the present research.

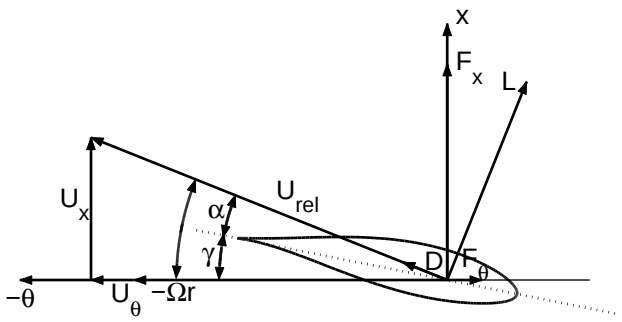


Figure 5.3: Sectional airfoil element with velocity and force vectors. Source: Réthoré et al.[48]

Réthoré et al.[48] validated the AD with tabulated airfoil data with full rotor computations of a single NREL 5-MW reference wind turbine. Reasonable agreement was found; however, the AD with tabulated airfoil data overpredicted the tangential forces, which resulted into an overpredicted power. In the present work, the AD with tabulated airfoil data is applied to wind turbines in wake conditions. Since the free-stream velocity is not known for wind turbine that is the lee of another, the rotational speed and the pitch are not known prior to the simulation, unless they are constant with wind speed. Unfortunately, any form of wind turbine control, e.g., a torque-controller or pitch controller, is not available for the present research. Instead, a relationship of the torque $\tau$ and the rotational speed $\Omega$ is derived, through a calibration of a number of single wind turbine simulations with different free-stream velocities, as performed in the work of Wu and Porté-Agel.[80] The calibration setup is similar to the one that used for Method II from Section 5.2.2. The $\tau$-$\Omega$ relationship can be used to calculate $\Omega$ during the simulation, in an iterative manner. At the first time step, $\Omega$ is guessed, which gives a value for $\tau$. Subsequently, a new $\Omega$ is obtained from the $\tau$-$\Omega$ relationship and it is used for the second time step. The process is repeated until a satisfactory level of convergence is reached. Although not mentioned by Wu and Porté-Agel, the use of a $\tau$-$\Omega$ relationship without a pitch controller only makes sense for the wind speed region in which the blade pitch $\theta_p$ is zero. If the blade pitch is not zero, one still needs to know the free-stream velocity in order to obtain the pitch from the pitch curve, such that the correct forces are obtained. Alternatively, if one could define two seperate regions, in which either rotational speed

control or pitch control is applied, it is possible to derive a corresponding $\tau$-$\Omega$ and a $\tau$-$\theta_p$ relation, through calibration. During the simulation, the wind turbine determines which relation it should use by a switch that is based on the torque. In the present work, only a $\tau$-$\Omega$ relationship is used for simplicity, by setting the zero pitch, which is true for the NREL 5-MW wind turbine operating at free-stream wind speeds between 5-11 m/s.

Four results of the $\tau$-$\Omega$ relationship are plotted in Figure 5.4, representing ambient turbulence intensities of 4% and 8% using two RANS turbulence models: the $k$-$\varepsilon$ EVM and $k$-$\varepsilon$-$f_P$ EVM. Figure 5.4 shows that the calibration is only sensitive to the turbulence model, as found for Method II from Section 5.2.2. The use of a $\tau$-$\Omega$ relationship has the advantage that the power is no longer overpredicted, since it is calibrated with the desired power curve.

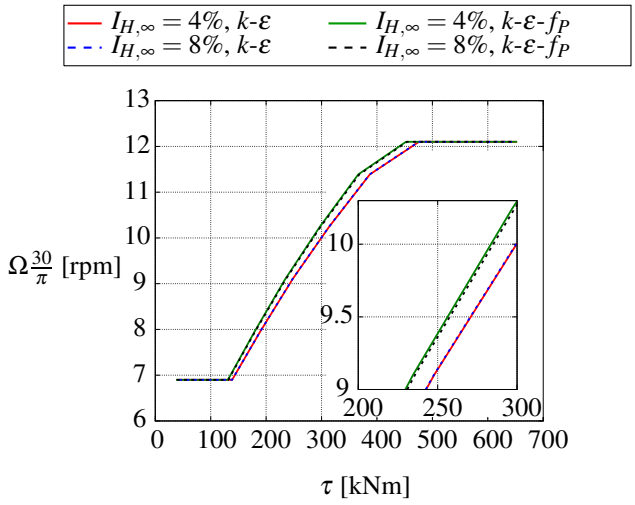


Figure 5.4: $\tau - \Omega$ relationship for the NREL 5-MW wind turbine.

## 5.3 Test cases

The variable AD force methods of Section 5.2 and three different turbulence models presented in Section 5.4.1 are tested with seven test cases, as shown in Table 5.2. All test cases are based on the NREL 5-MW reference wind turbine,[26] which has a rotor diameter $D$ of 126 m and a hub height $z_H$ of 90 m. The thrust coefficient $C_T$, the power coefficient $C_P$, the rotational speed $\Omega$ and the blade pitch angle $\theta_p$ are calculated with the aeroelastic code HAWCStab2,[23] and the results are plotted in Figure 5.5. HAWCStab2 couples the blade element momentum method with finite beam elements. The first test

case is a single wind turbine, and it is used to compare the variable AD force methods in terms of power production and thrust force, for a range of free-stream velocities at hub height $U_{H,\infty}$. The first four double wake cases are meant to compare the velocity deficit predicted by the $k$-$\varepsilon$-$f_P$ EVM and $k$-$\varepsilon$ EVM, with the one calculated by LES for double wake configurations, using constant AD forces. It is chosen to use constant forces, such that only the turbulence models are compared with respect to the flow around the same obstacles. Since everything is known about the LES, e.g., ambient turbulence levels and forces of the wind turbine, these four test cases are ideal to investigate the performance of the $k$-$\varepsilon$ EVM and the $k$-$\varepsilon$-$f_P$ EVM for double wake configurations. The last double wake cases are used to compare the three turbulence models in terms of power deficit. In these cases, one variable AD force method is used.

Table 5.2: Summary of cases and corresponding input parameters for numerical computations.

| Case | Description | $I_{H,\infty}$ [-] | $U_{H,\infty}$ [m/s] | spacing [m/D] |
|---|---|---|---|---|
| Single wake, variable forces | | | | |
| 1 | NREL 5-MW | 8% | 4-25 | - |
| Double wake, constant forces, one wind direction | | | | |
| 2 | NREL 5-MW aligned, low $I_{H,\infty}$ | 4% | 8 | 5 |
| 3 | NREL 5-MW aligned, high $I_{H,\infty}$ | 8% | 8 | 5 |
| 4 | NREL 5-MW staggered, low $I_{H,\infty}$ | 4% | 8 | 5 |
| 5 | NREL 5-MW staggered, high $I_{H,\infty}$ | 8% | 8 | 5 |
| Double wake, variable forces, relative wind direction range: -24°,24° | | | | |
| 6 | NREL 5-MW low $I_{H,\infty}$ | 4% | 8 | 5 |
| 7 | NREL 5-MW high $I_{H,\infty}$ | 8% | 8 | 5 |

All double wake cases are simulated with $U_{H,\infty} = 8$ m/s and have a spacing of five rotor diameters. The wind turbine spacing could represent the first two wind turbine in the Lillgrund off-shore wind farm, located in Sweden, for northern wind directions.[15] The influence of the ambient turbulence intensity $I_{H,\infty}$ is investigated by using 8% for the odd cases and 4% for the even cases. Note that $I_{H,\infty} \equiv \sqrt{2/3k}/U_{H,\infty}$ represents the total turbulence intensity, with $k$ as the turbulent kinetic energy. In addition, the position of the wind turbines in the double wake cases is investigated. In the double wake cases with constant AD forces, two orientations are chosen with a spacing of 5D: an aligned and a staggered layout, as sketched in Figure 5.6. The position in the last two double wake cases is changed for a number of simulations, representing relative wind directions between 0°and 24°.

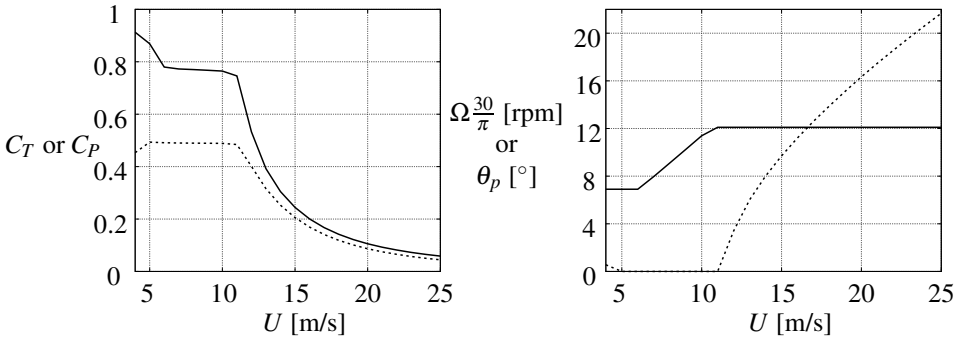


Figure 5.5: NREL 5-MW wind turbine. Left: $C_T$ (solid line) and $C_P$ (dashed line). Right: rotational speed $\Omega\frac{30}{\pi}$ in rpm (solid line) and blade pitch angle $\theta_p$ (dotted line).

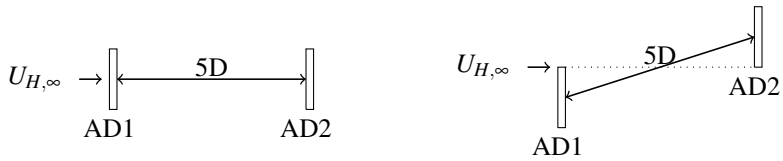


Figure 5.6: Sketch of double wake cases 2-5. Left: aligned and right: staggered.

## 5.4 Simulations

The test cases from Table 5.2 are simulated in the present section. The simulation methods and results are discussed in Sections 5.4.1 and 5.4.2, respectively.

### 5.4.1 Method

The RANS and LES are computed with EllipSys3D,[36,62] the in-house incompressible finite volume code of DTU Wind Energy. EllipSys3D solves the Navier-Stokes equations with the SIMPLE algorithm[41], and the convective terms are treated by the QUICK scheme.[32] The flow variables are stored in the cell centers, which can cause decoupling of the pressure with body forces. A modified Rhie-Chow algorithm[47,49] is used to avoid this decoupling. The setup for the RANS and LES is discussed separately in Sections 5.4.1.1 and 5.4.1.2, respectively.

#### 5.4.1.1 RANS

The flow domain definition of all seven test cases, as defined in Table 5.2, is the same for all RANS simulations, although the sizes are different. In Figure 5.7, the grid of

test cases 6 and 7 is shown, including the general flow domain definitions that apply for all test cases. In these test cases, the position of the upstream AD is kept constant, while the downstream AD is moved on an arc to model the relative wind directions. To illustrate this, three positions of the downstream AD are sketched in Figure 5.7, namely at 0°, 12°and 24°. Around the two ADs, a wake domain is specified in which the cells are uniformly distributed in all directions with a spacing of $D/10$. The cell size of $D/10$ is based on a detailed grid refinement study, performed in previous work.[76] In the $y$ direction, the wake domain is positioned in the middle of the flow domain. Outside the wake domain, stretching is performed with a maximum cell-edge growth factor of 1.2. The size of the flow domain, the wake domain and the grid sizes are listed in Table 5.3, for all seven test cases. The boundaries at $x = 0$ and $z = L_z$ are inlets at which the log law solution is specified:

$$U(z) = \frac{u_*}{\kappa} \ln\left(\frac{z}{z_0}\right), \qquad k = \frac{u_*^2}{\sqrt{C_\mu}}, \qquad \varepsilon = \frac{u_*^3}{\kappa z}, \tag{5.8}$$

with $u^*$ as the friction velocity, $z_0$ as the wall roughness, $k$ as the turbulent kinetic energy and $\kappa = 0.4$ as the Von Kármán constant. The ambient turbulence intensity $I_{H,\infty}$ is set by $z_0$ while keeping $C_\mu = 0.03$ constant:

$$I_{H,\infty} \equiv \frac{\sqrt{\frac{2}{3}k}}{U_{H,\infty}} = \frac{\kappa\sqrt{\frac{2}{3}}}{\ln\left(\frac{z_H}{z_0}\right)\sqrt[4]{C_\mu}}, \tag{5.9}$$

and $u_*$ is set such that the desired free-stream velocity $U_{H,\infty}$ at hub height $z_H$ is obtained. The side boundaries at $y = 0$ and $y = L_y$ are slip walls at which a Neumann condition is applied. Note that one could also use periodic boundary conditions, although the difference between the use of periodic or slip boundaries is not significantly noticeable in the wake solution because the boundaries are sufficiently far away. The bottom wall at $z = 0$ is a rough wall at which the turbulent dissipation and the wall stress are specified at the first cell and a Neumann boundary condition is used for the turbulent kinetic energy. To keep the total number of cells low (1.2 million for test cases 6 and 7), the height of the first cell is set to 0.5 m. An outlet is used at the end of the domain, at $x = L_x$, assuming fully developed flow.

Two RANS turbulence models are investigated; the standard $k$-$\varepsilon$ EVM, first introduced by Launder and Spalding,[31] and the $k$-$\varepsilon$-$f_P$ EVM that is developed in previous work.[76] Both turbulence models use the Boussinesq approximation[9] for the Reynolds-stresses $\overline{u_i' u_j'}$:

$$\overline{u_i' u_j'} = \frac{2}{3}k\delta_{ij} - \nu_T\left(U_{i,j} + U_{j,i}\right), \tag{5.10}$$

Table 5.3: RANS flow domain definition of all test cases. Domain sizes and AD coordinates are normalized by the rotor diameter $D$.

| | | Flow domain | | | Wake domain | | | | Upstream AD | | Downstream AD | |
|---|---|---|---|---|---|---|---|---|---|---|---|---|
| Case | Description | $L_x$ | $L_y$ | $L_z$ | $l_x$ | $l_y$ | $l_z$ | $l_{x,up}$ | $AD_x$ | $AD_y$ | $AD_x$ | $AD_y$ |
| Single wake, variable forces | | | | | | | | | | | | |
| 1 | - | 25 | 16 | 16 | 12 | 3 | 3 | 2 | 5 | 8 | - | - |
| Double wake, constant forces, one wind direction | | | | | | | | | | | | |
| 2-3 | aligned | 25 | 20 | 16 | 16 | 6 | 3 | 2 | 5 | 8 | 10 | 8 |
| 4-5 | staggered | 25 | 20 | 16 | 16 | 6 | 3 | 2 | 5 | 7.5 | 10 | 8.5 |
| Double wake, variable forces, relative wind direction range: -24°,24° | | | | | | | | | | | | |
| 6-7 | - | 25 | 20 | 16 | 14 | 6 | 3 | 2 | 5 | 8.5 | variable | variable |

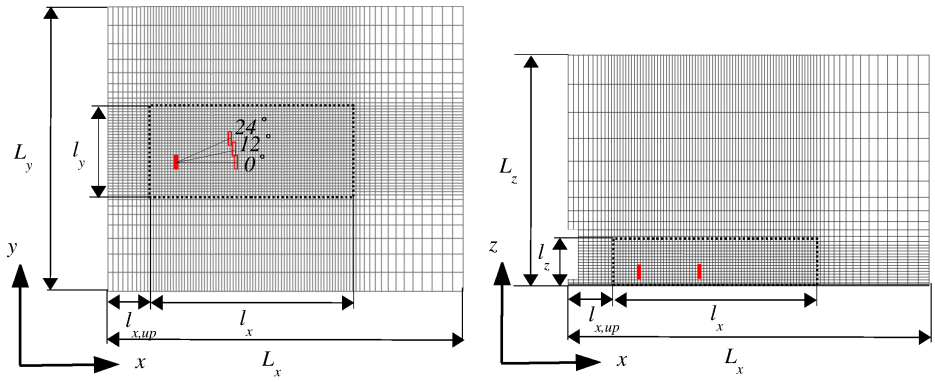


Figure 5.7: General computational domain in RANS simulations. Left: top view. Right: side view. Dashed black box marks the wake domain. ADs are illustrated as red boxes, upstream AD is filled, downstream is not. AD setup shown corresponds to test cases 6 and 7. One in every two nodes is shown.

where $\delta_{ij}$ is the Kronecker delta, $U_{i,j}$ are the mean velocity gradients and $\nu_T$ is the turbulent eddy viscosity:

$$\nu_T = C_\mu f_P \frac{k^2}{\varepsilon}, \tag{5.11}$$

with $C_\mu$ as a constant and $\varepsilon$ as the turbulent dissipation. In the standard $k$-$\varepsilon$ EVM $f_P = 1$ and in $k$-$\varepsilon$-$f_P$ EVM $f_P$ is a scalar function that is dependent on the local shear parameter: $\sigma \equiv \frac{k}{\varepsilon}\sqrt{(U_{i,j})^2}$. Effectively, the $k$-$\varepsilon$-$f_P$ EVM has a variable $C_\mu$, which is the

only difference with the standard $k$-$\varepsilon$ EVM. The scalar function $f_P$ of the $k$-$\varepsilon$-$f_P$ EVM is defined as:[2]

$$f_P\left(\sigma/\tilde{\sigma}\right) = \frac{2f_0}{1+\sqrt{1+4f_0\left(f_0-1\right)\left(\frac{\sigma}{\tilde{\sigma}}\right)^2}},\ f_0 = \frac{C_R}{C_R-1}, \tag{5.12}$$

with $\tilde{\sigma}$ as the shear parameter in a log law of the atmospheric boundary layer and $C_R$ is a calibration parameter. In the log law solution ($\sigma = \tilde{\sigma}$), $f_P = 1$ and for a high shear parameter ($\sigma > \tilde{\sigma}$) $f_P < 1$. High velocity gradients are present in the wake region, which results into a lower turbulent eddy viscosity in the wake predicted by the $k$-$\varepsilon$-$f_P$ EVM compared to the one predicted by the $k$-$\varepsilon$ EVM. Hence, the $k$-$\varepsilon$-$f_P$ EVM delays the wake recovery. $C_R$ controls the magnitude of the delayed wake recovery and it is therefore a very important parameter. In previous work,[76] the constant $C_R$ is calibrated against LES for eight different single wind turbine cases. Both the standard $k$-$\varepsilon$ EVM and the $k$-$\varepsilon$-$f_P$ EVM use the same transport equations for $k$ and $\varepsilon$:

$$\begin{aligned}\frac{Dk}{Dt} &= \nabla\cdot\left[\left(\nu+\frac{\nu_T}{\sigma_k}\right)\nabla k\right] + \mathscr{P} - \varepsilon, \\ \frac{D\varepsilon}{Dt} &= \nabla\cdot\left[\left(\nu+\frac{\nu_T}{\sigma_\varepsilon}\right)\nabla \varepsilon\right] + \left(C_{\varepsilon,1}\mathscr{P} - C_{\varepsilon,2}\varepsilon\right)\frac{\varepsilon}{k},\end{aligned} \tag{5.13}$$

where $\mathscr{P}$ is the turbulent production, $\nu$ is the kinematic molecular viscosity and $C_{\varepsilon,1}, C_{\varepsilon,2}$, $\sigma_k$, $\sigma_\varepsilon$ are constants. The values of the constants are listed in Table 5.4.

Table 5.4: Model constants.

| $C_R$ | $C_\mu$ | $C_{\varepsilon,1}$ | $C_{\varepsilon,2}$ | $\sigma_k$ | $\sigma_\varepsilon$ | $\kappa$ |
|---|---|---|---|---|---|---|
| 4.5 | 0.03 | 1.21 | 1.92 | 1.00 | 1.30 | 0.40 |

#### 5.4.1.2 LES

The general flow domain of the LES is shown in Figure 5.8 and the corresponding dimensions are listed in Table 5.5 for each test case. Around the two ADs, a wake domain is defined where the cell spacing is uniformly set in all directions such that the cell size is D/30. 1.5D upstream of the first AD, synthetic atmospheric turbulence is injected on to a plane that is 8D wide and extents 8D from the bottom. This inflow turbulence is calculated prior to the simulation with the Mann model,[35] using a box of with a cross section that is similar to the injection plane. The length of the Mann turbulence box is set to 256D, such that 1 h of turbulence plus start up time are generated. The spacing in the Mann turbulence box is D/8 in all directions. Details of the application of Mann turbulence in wind turbine wake simulations can be found in the work of Troldborg et

al.[69,71] It should be noted that the cell spacings in the wake domain are twice as large as used in previous work;[76] hence, a large reduction in computational effort is achieved. A recent grid dependence study of single wind turbine wakes has shown that using a cell size of D/30 in the wake domain is sufficient to resolve the Mann turbulence and wind turbine wake.[77] The total grid size of the grid presented in Figure 5.8 is 12 million cells.

Table 5.5: LES flow domain definition of all test cases. Domain sizes and AD coordinates are normalized by the rotor diameter $D$.

| | | Flow domain | | | Wake domain | | | | Plane | Upstream AD | | Downstream AD | |
|---|---|---|---|---|---|---|---|---|---|---|---|---|---|
| Case | Description | $L_x$ | $L_y$ | $L_z$ | $l_x$ | $l_y$ | $l_z$ | $l_{x,up}$ | $t_x$ | $AD_x$ | $AD_y$ | $AD_x$ | $AD_y$ |
| Double wake, constant forces, one wind direction | | | | | | | | | | | | | |
| 2-3 | aligned | 25 | 20 | 16 | 14.5 | 4.4 | 2 | 3.25 | 3.5 | 5 | 8 | 10 | 8 |
| 4-5 | staggered | 25 | 20 | 16 | 14.5 | 6.9 | 2 | 3.25 | 3.5 | 5 | 7.5 | 9.9 | 8.5 |
| Double wake, variable forces, relative wind direction range: -24°,24° | | | | | | | | | | | | | |
| 6-7 | - | 25 | 20 | 16 | 14.3 | 6 | 2 | 3.25 | 3.5 | 5 | 8.5 | variable | variable |

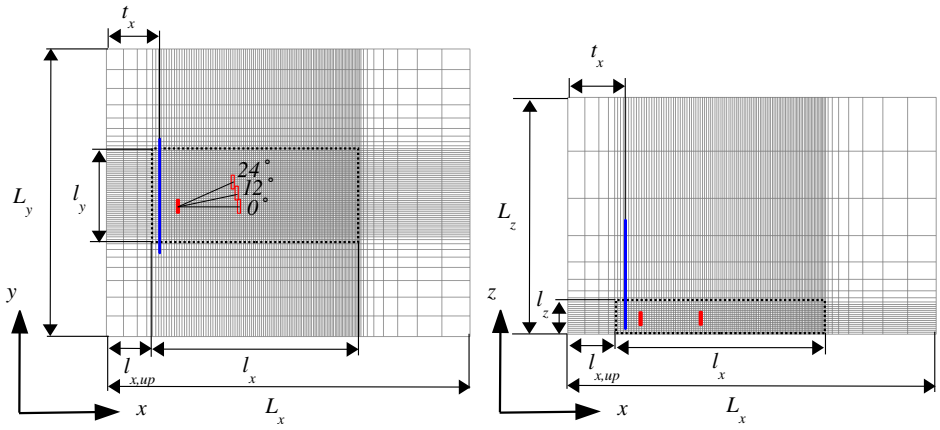


Figure 5.8: General computational domain in LES. Left: top view. Right: side view. Dashed black marks the wake domain. ADs are illustrated as a red box, upstream AD is filled, downstream is not. AD setup shown corresponds to test cases 6 and 7. The blue line is the injection plane where the Mann turbulence is imposed. One in every four nodes is shown.

The boundaries at $x = 0$ and $z = L_z$ are all inlet boundaries, at which the inlet profiles of equation (5.8) are imposed. The bottom wall at $z = 0$ is not resolved by the LES and

therefore, a slip wall is specified here. The side boundaries at $y = 0$ and $y = L_y$ are also slip walls and an outlet boundary is set at $x = L_x$.

The time step is not restricted since the time integration in EllipSys3D is implicit. Although the time step is set to 0.24 s to assure that the unsteady LES data is captured with a high sample frequency.

Details of the LES implementation can be found in the work of Bechmann.[7]

## 5.4.2 Results and Discussion

Table 5.1 shows an overview of the comparisons. The results of the three variable AD force methods, for single and double wake simulations, are discussed in Sections 5.4.2.1 and 5.4.2.2, respectively. In these sections, the turbulence is modeled by the $k$-$\varepsilon$-$f_P$ EVM. The influence of the turbulence model on the velocity deficit, using constant AD forces, is presented in Section 5.4.2.3. A similar exercise is conducted in Section 5.4.2.4, where a variable AD force method is employed to estimate the power deficit.

The results of the LES are made from an average of six 10 min bins, and the error bars represent the corresponding standard deviations of the six bins. In addition, all power deficit plots are made from simulations with relative wind directions that range from $0^\circ$ to $24^\circ$. Since the AD is always placed in the cell centers, the simulated wind direction can deviate from the one that is set. Therefore, the simulated wind directions are used in the power deficit plots. The influence of wake rotation on the power deficit is assumed to be small; hence, the results of the negative range of the relative wind directions is simply a mirror image of the simulated positive range.

### 5.4.2.1 Comparison of variable AD force methods for a single wind turbine

The three variable AD force methods of Section 5.2 are applied to a single wind turbine for 22 undisturbed hub height velocities between 4 m/s and 25 m/s, with a uniform spacing of 1 m/s. The single wind turbine corresponds to test case 1 from Table 5.2. Note that Method III is applied without the $\tau$-$\Omega$ calibration procedure, since $\Omega$ is known for single wind turbine simulations. The results of the power curve and the thrust force are compared with the results of two HAWCStab2[23] aeroelastic computations, as shown in Figure 5.9. One HAWCStab2 computation is carried out without the blade deflections. Note that the HAWCStab2 computations are not coupled with EllipSys3D. The difference in power and normal force between Method III and the HAWCStab2 simulation with blade deflections is large above rated wind speeds. However, the power and normal force of the HAWCStab2 computation without blade bending compares reasonably well with the CFD, which shows that the effect of the blade deflection is significant above rated wind speeds. In the wind speed range below rated, Method III overpredicts the power compared to HAWCStab2 by 10% to 20%, however, the difference is not caused by the blade deflection because both HAWCStab2 computations show similar results. Réthoré et al.[48] also found that Method III overpredicts the power for a wind speed of

8 m/s. In Method III the local blade force is scaled with the local velocity. Since the velocity gradients are high at the AD location, the sensitivity of location where the local velocity is extracted is high. Réthoré et al. argued that the overprediction in power might be related to the position at which the local velocity is extracted. Method I does not suffer from the severe overprediction in power and normal force above rated wind speeds because it adjusts the forces dynamically, using the local induction. For the wind speeds below rated, Method I still overpredicts the power and the thrust force. The difference is caused by an overprediction of the free-stream velocity by 2-3% when equation (5.4) is applied, which translates to an average error in thrust force and power of $(1.025^2-1)\times 100\% \approx 5\%$ and $(1.025^3-1)\times 100\% \approx 8\%$, respectively. Method I gives unstable results at a free-stream velocity of 11 m/s, at which the solution is alternating between two equilibrium points during simulation. This phenomenon is not observed in the other two variable AD force methods. Unlike Method III and Method I, Method II predicts the exact same power and normal force as the HAWCStab2 computation with deflection, since it was calibrated to do so.

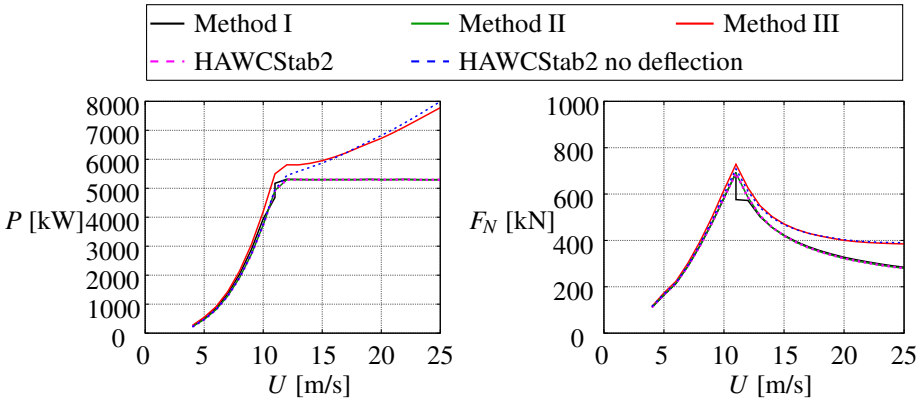


Figure 5.9: Power curve and normal force of the NREL 5-MW wind turbine. Case 1: a single wind turbine with $I_{H,\infty} = 8\%$.

#### 5.4.2.2 Comparison of variable AD force methods for double wakes

Test cases 6 and 7 of Table 5.2 are used to compare the variable AD force methods for the power prediction of double wakes. In this exercise, only the $k$-$\varepsilon$-$f_P$ EVM is employed. In the simulations using Method I (Section 5.2.1) and Method II (Section 5.2.2), the power curve and the normal force calculated by Method III are used as an input, instead of the power curve and normal force calculated by HAWCStab2. By doing so, it can be shown that Method III and Method II show the same results in terms of power deficit. In

addition, only wind speeds in the zero pitch region are considered, to avoid the necessity of a pitch controller in Method III. Prior to the double wake simulations, a calibration of the alternative scaling coefficients $C_T^*$, $C_P^*$ and $\Omega^*$ for Method II is made, as discussed in Section 5.2.2. In addition, the $\tau - \Omega$ relation is derived for Method III, which is explained in Section 5.2.3.

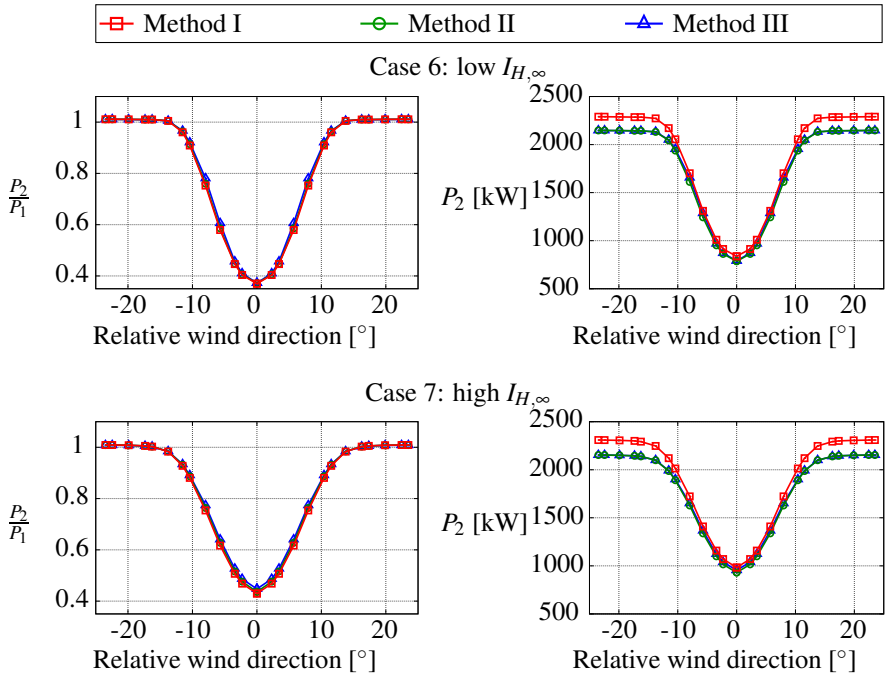


Figure 5.10: Power deficit of the downstream wind turbine. Cases 6 and 7: a double wake with a range of relative wind directions for $I_{H,\infty} = 4\%$ and $I_{H,\infty} = 8\%$, respectively.

The power of the downstream wind turbine $P_2$ and the power ratio of the downstream and upstream $P_2/P_1$ are plotted in Figure 5.10. For each variable AD force method, 13 positive relative wind directions are simulated per test case. The power production of the downstream wind turbine, calculated with Method III and Method II, compares very well. Hence, if airfoil data is not available but $C_T$, $C_P$ and $\Omega$ is, Method II is good alternative. Method I overpredicts the power of the downstream wind turbine compared to the other variable AD force methods because the free-stream velocity of the second wind turbine is overpredicted. This result is also observed in the single wind turbine simulations of Section 5.4.2.1. Surprisingly, all variable AD force methods compare well with respect to the power ratio of the downstream and upstream wind turbine. Since Method I also overpredicts the power of the upstream wind turbine, the resulting power

ratio is comparable with one calculated by the other two variable AD force methods.

As expected, the test case with the lower ambient turbulence intensity shows a larger power deficit compared to the test case with the high ambient turbulence intensity. However, the effect of turbulence intensity on the comparison of the variable AD force methods is negligible.

#### 5.4.2.3 Comparison of turbulence models for double wakes using constant forces

The $k$-$\varepsilon$ EVM and $k$-$\varepsilon$-$f_P$ EVM are compared with LES for double wake configurations using constant forcing. Even though constant AD forces are not realistic for real wind turbines that are operating in wakes of upstream wind turbines, this setup is of interest when testing the RANS-based turbulence models. In total, four cases are simulated with all three turbulence models: an aligned and a staggered configuration with a low and a high ambient turbulence intensity. The cases are further described in Section 5.3. The velocity deficit, the $f_P$ function and the turbulence intensity are shown in Figures 5.11, 5.12 and 5.13, respectively. The results are extracted over a straight line in the $y$-direction, at 2.5D, 5D, 7.5D, 10D and 12.5D downstream from the first AD. Note that the second AD is located at 5D downstream from the first AD.

In the aligned cases (cases 2 and 3) from Figure 5.11, the $k$-$\varepsilon$ EVM underpredicts the velocity deficit at 2.5D with respect to LES, whereas the $k$-$\varepsilon$-$f_P$ EVM compares very well with LES. This result is expected since the $k$-$\varepsilon$-$f_P$ EVM is calibrated with LES for single wakes. The performance of the $k$-$\varepsilon$ EVM is still poor at 5D. Hence, if a variable AD force method would be used that is based on the local AD velocity, the forcing of the second AD would be much larger in the $k$-$\varepsilon$ EVM compared to the one in the $k$-$\varepsilon$-$f_P$ EVM and LES. At 7.5D (2.5D downstream from the second AD), the $k$-$\varepsilon$-$f_P$ EVM compares less well with LES, especially for the case with low ambient turbulence (case 2). However, the $k$-$\varepsilon$-$f_P$ EVM is still performing better than the standard $k$-$\varepsilon$ EVM. At 10D and 12.5D, the difference between all turbulence models is negligible.

The staggered cases (cases 4 and 5) show similar results as the aligned case at 2.5D. At 5D, a complex velocity profile is visible in which the wake of the first AD is merging with the newly created wake of the second AD. Since the second AD is not in the full wake of the first AD, the velocity deficit of the second AD computed by the $k$-$\varepsilon$ EVM is not much different from the one that is predicted by the $k$-$\varepsilon$-$f_P$ EVM and LES. In contradiction to the aligned cases (cases 2 and 3), the $k$-$\varepsilon$ EVM would not underpredict the AD force significantly when a variable AD force method is used. Note that the wake of the first AD at 5D is still underpredicted by the $k$-$\varepsilon$ EVM. At 7.5D, the skewed velocity deficit calculated by LES is more complex compared to the RANS-based turbulence models; however, the $k$-$\varepsilon$-$f_P$ EVM is still able to approximate it, especially for the high ambient turbulence case. Further downstream in the low ambient turbulence case, at 10D and 12.5D, there are small differences in the predicted velocity deficit of the $k$-$\varepsilon$-$f_P$ EVM and LES. These difference are negligible for the high ambient turbulence case.

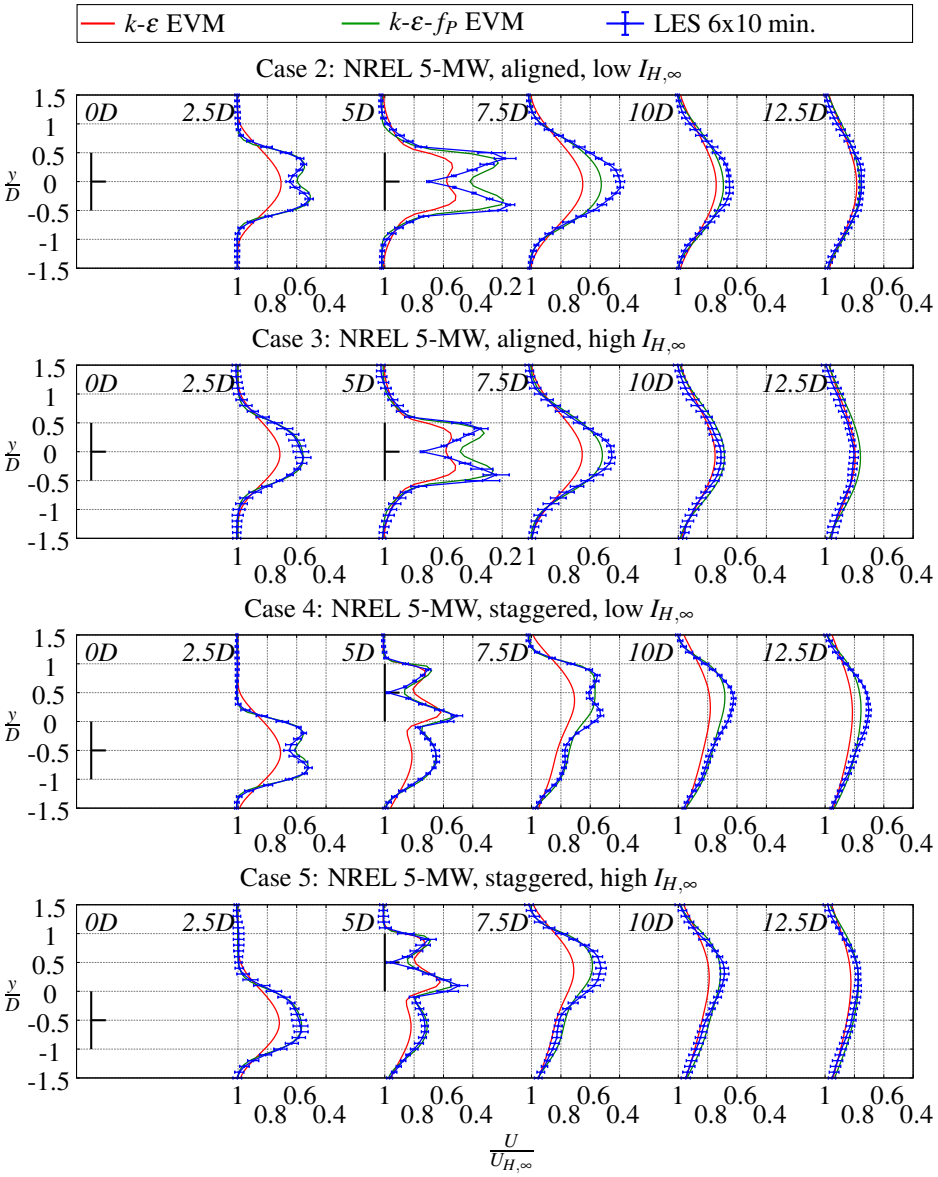


Figure 5.11: Velocity deficit for cases 2-5, a double wake in an aligned and a staggered layout, for $I_{H,\infty} = 4\%$ and $I_{H,\infty} = 8\%$. The LES results include error bars of one standard deviation.

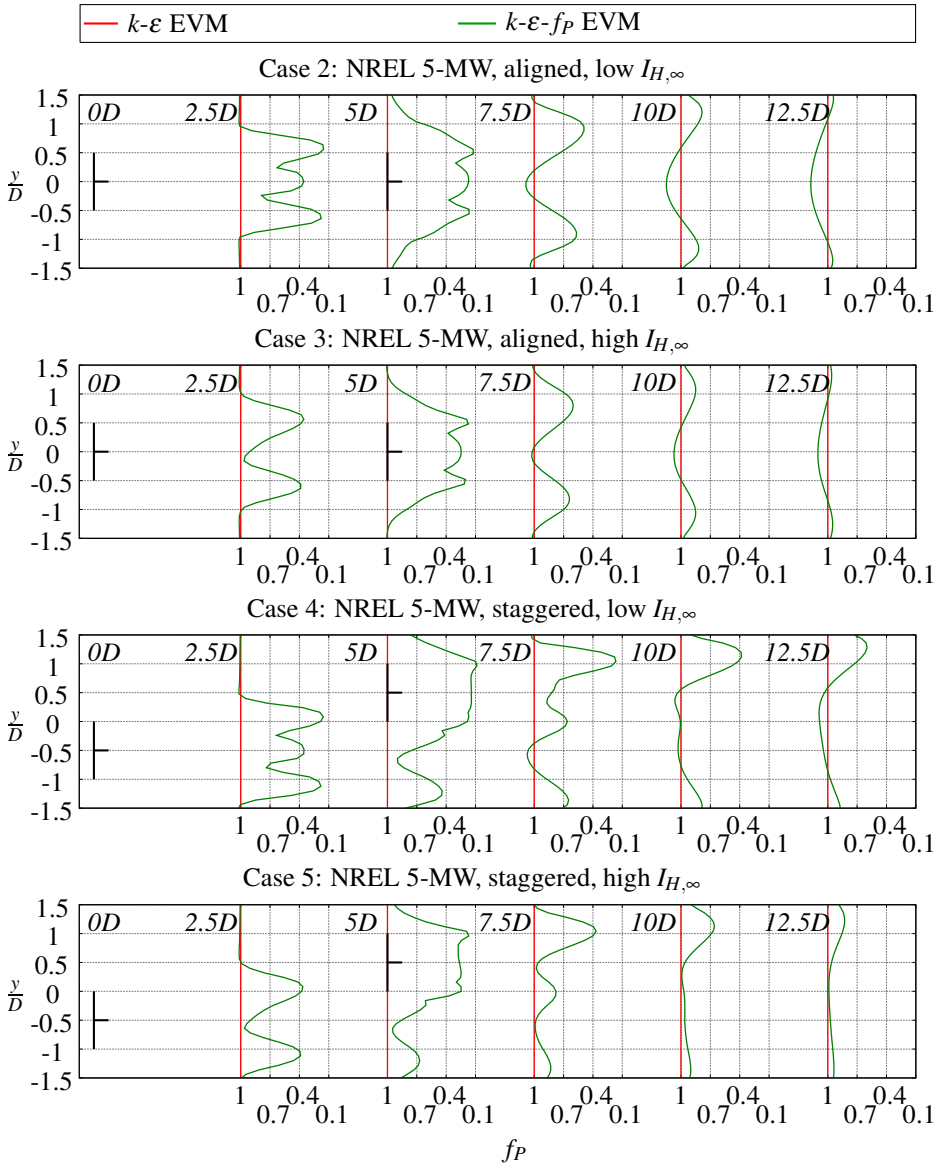


Figure 5.12: $f_P$ function for cases 2-5, a double wake in an aligned and a staggered layout, for $I_{H,\infty} = 4\%$ and $I_{H,\infty} = 8\%$.

The function $f_P$, that represents the varying part of the effective eddy viscosity coefficient in $k$-$\varepsilon$-$f_P$ EVM, as defined in equation (5.11), is plotted in Figure 5.12. The results are compared with the $k$-$\varepsilon$ EVM, in which $f_P$ is equal to one by definition. In the near wake, the value of $f_P$ is smaller than one, because the velocity gradients are high, especially at the edge of wake. Hence, the eddy viscosity is decreased and the wake recovery is delayed, as observed in Figure 5.11. The value of $f_P$ in the near wake is the smallest in the low ambient turbulence cases, because the velocity gradients in the wake are higher when the ambient turbulence intensity is lowered. This explains why the difference in velocity deficit between the $k$-$\varepsilon$-$f_P$ EVM and the $k$-$\varepsilon$ EVM is the largest in the low ambient turbulence intensity cases (cases 2 and 4). Further downstream, the $f_P$ function shows values higher than one, which means that, at these locations, the wake is recovering faster in the $k$-$\varepsilon$-$f_P$ EVM than the $k$-$\varepsilon$ EVM. This behavior of the $f_P$ function is the cause of the difference in the velocity deficit between the $k$-$\varepsilon$-$f_P$ EVM and LES, in the aligned cases, at 2.5D from the second AD, as seen in Figure 5.11. The trend in the far wake shows that the $f_P$ function goes back to one, which explains why the velocity deficit of the $k$-$\varepsilon$-$f_P$ EVM approaches the one of the $k$-$\varepsilon$ EVM, at this downstream location.

The turbulence intensity at hub height $I_H = \sqrt{2/3k}/U_{H,\infty}$ is shown in Figure 5.13. The standard $k$-$\varepsilon$ EVM overpredicts the turbulence intensity in the wake center at 2.5D in all cases, compared to LES. This overprediction is also observed for single wake simulations performed in previous work,[76,77] which is caused by the fact that the $k$-$\varepsilon$ EVM produces a non-physical increase in turbulence intensity at 0D, whereas the $k$-$\varepsilon$-$f_P$ EVM and LES do not show any added wake turbulence yet. This non-physical increase in turbulence intensity of the $k$-$\varepsilon$ EVM at 0D, for single wake simulations, is also visible in the staggered double wake cases at 5D (between $y/D = 0.5$ and $y/D = 1$), especially for the case with a low ambient turbulence intensity. Both RANS models overpredict the turbulence intensity in the far wake compared to LES. One should keep in mind that the RANS models can only model isotropic turbulence, which is a plausible cause for the overprediction of turbulence intensity of a wake that is characterized by anisotropic turbulence.

#### 5.4.2.4 Comparison of turbulence models for double wake using variable forces

The double wake test cases, 6 and 7 from Table 5.2, are used to compare the $k$-$\varepsilon$-$f_P$ EVM with the standard $k$-$\varepsilon$ EVM and LES, for one variable AD force method. To avoid the need of expensive calibrations in the LES for Method II and Method III, the simple AD Induction Method (Method I) is employed. In Figure 5.14, the power production of the downstream wind turbine and the power ratio of the downstream and the upstream wind turbine are plotted against the simulated relative wind directions. In terms of absolute power of the downstream wind turbine, the $k$-$\varepsilon$-$f_P$ EVM compares well with LES, also outside the wake of the downstream wind turbine. On the contrary, the $k$-$\varepsilon$ EVM shows

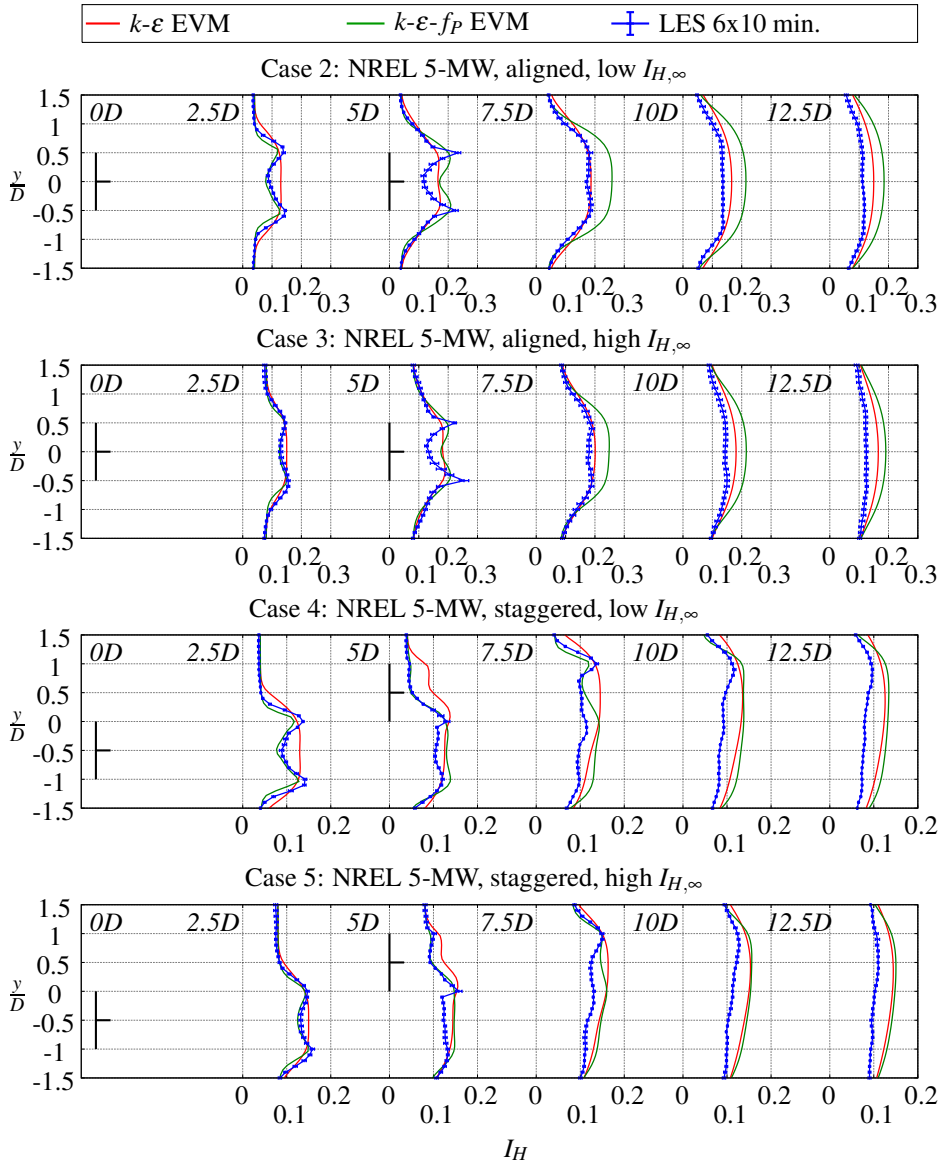


Figure 5.13: Turbulence intensity for cases 2-5, a double wake in an aligned and a staggered layout, for $I_{H,\infty} = 4\%$ and $I_{H,\infty} = 8\%$, respectively. The LES results include error bars of one standard deviation.

a larger power of the downstream wind turbine outside the wake region, which is caused by an overpredicted $\langle U_{AD} \rangle$. This indicates that the axial induction, predicted by the $k$-$\varepsilon$ EVM, does not compare well with the one of the $k$-$\varepsilon$-$f_P$ EVM and LES. The power deficit of the downstream wind turbine is underpredicted by the $k$-$\varepsilon$ EVM, which is best visible in the plots of the power ratio. In the comparison of the turbulence models with constant AD forces (Section 5.4.2.3), it is observed that the velocity deficit is underpredicted by the $k$-$\varepsilon$ EVM. This translates into an underprediction of the power deficit in Figure 5.14. The $k$-$\varepsilon$ EVM performs the worst for the low ambient turbulence case, which is also seen in the comparison with the constant AD forces from Section 5.4.2.3. The power deficit of the $k$-$\varepsilon$-$f_P$ EVM compares very well with the one of LES, especially for the low ambient turbulence case. The variable $C_\mu$, which is present in the $k$-$\varepsilon$-$f_P$ EVM, establishes the improvement by lowering the eddy viscosity in the near wake region.

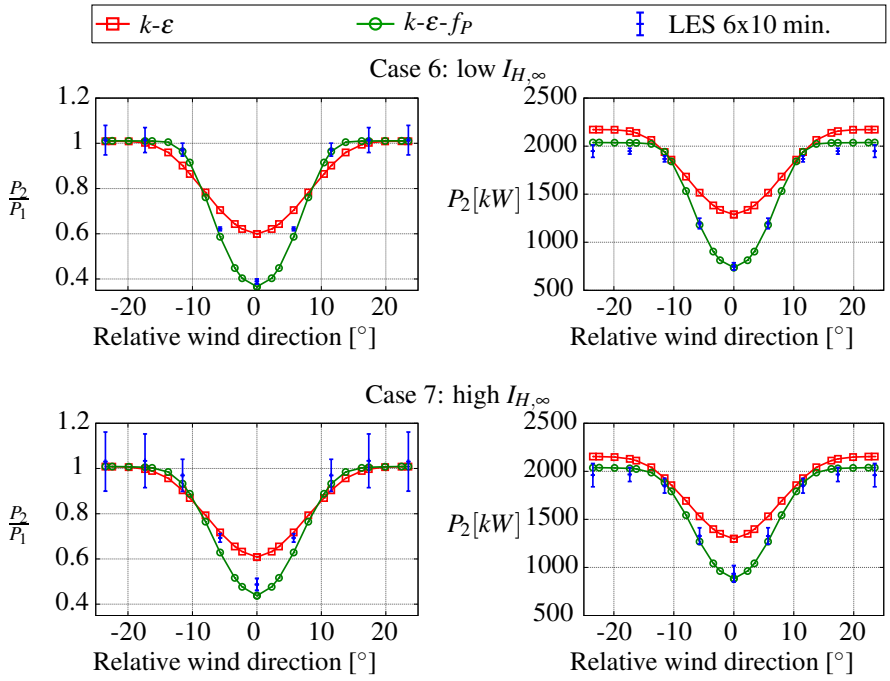


Figure 5.14: Power deficit of the downstream wind turbine. Cases 6 and 7: a double wake with a range of relative wind directions for $I_{H,\infty} = 4\%$ and $I_{H,\infty} = 8\%$, respectively. The LES results include error bars of one standard deviation.

## 5.5 Conclusions

Two existing variable AD methods, the AD Induction Method (Method I) and the AD Airfoil Method (Method III), are compared with the proposed AD Variable Scaling Method (Method II), for single and double wake simulations, employing the $k$-$\varepsilon$-$f_P$ EVM. Compared with the aeroelastic code HAWCStab2, Method III without torque calibration overpredicts the power and the thrust force of a single wind turbine, for wind speeds above rated, because blade deflections are not included. For wind speeds below rated, Method III calculates the correct total thrust force but still overpredicts the power by 10-20%. Method I overpredicts the power and the thrust force below rated wind speeds, because the dynamically predicted undisturbed velocity at hub height is overpredicted by 2-3%. On the contrary, the proposed Method II produces exactly same results as HAWCStab2 because the method relies on calibration. This exercise shows that Method II is flexible because it can be used to fit any reference $C_T$, $C_P$ and $\Omega$.

When the power and the thrust force, predicted by Method III for a single wind turbine, are used as an input for Method I and Method II, the results of Method III and Method II compare very well for double wake simulations. This shows that when airfoil data is not available but information about $C_T$, $C_P$ and $\Omega$ is, Method II is a good alternative. In the double wake configuration, the power ratio predicted by Method I compares well with Method III and Method II, because Method I overpredicts the power of both the upstream and the downstream wind turbines by a similar factor. Therefore, if only the power ratio of the upstream and downstream wind turbine is desired, the simple Method I is an acceptable method. On the contrary, if accurate absolute power is needed, only the proposed Method II can be used. It should be noted that numerically unstable behavior is observed for one of the simulations employing Method I, because the solution of local velocity at the AD oscillated between two converged values. In other words, the solution of the local velocity at the AD is not unique. This behavior has not been seen in the other two variable AD force methods.

The performance of the $k$-$\varepsilon$ EVM and the $k$-$\varepsilon$-$f_P$ EVM is tested against LES for six double wake cases with different wind turbine positions and ambient turbulence intensities. Four cases are simulated with constant AD forces, and two cases are carried out with variable AD forces, using Method I. The cases with constant forces show that the $k$-$\varepsilon$ EVM underpredicts the velocity deficit in the near wake and at the location of the downstream wind turbine compared with LES, especially for low ambient turbulence and in full wake conditions. On the contrary, the $k$-$\varepsilon$-$f_P$ EVM shows comparable velocity deficits with LES. When the wind turbines are staggered, the velocity deficit at the downstream wind turbine, calculated with the $k$-$\varepsilon$ EVM is similar to the one of the $k$-$\varepsilon$-$f_P$ EVM and LES, because the downstream wind turbine is not operating in full wake conditions. In addition, at 7.5D downstream of the second wind turbine the difference between $k$-$\varepsilon$ EVM and the $k$-$\varepsilon$-$f_P$ EVM is small and both models show similar velocity deficits. The turbulence intensity in the wake is overpredicted by both RANS models;

however, the $k$-$\varepsilon$-$f_P$ shows a comparable turbulence intensity with LES in the near wake.

The underpredicted velocity deficit at location of the downstream wind turbine, calculated by the $k$-$\varepsilon$ EVM in full wake conditions, translates into an underpredicted power deficit in the test cases with variable AD forces. In addition, the $k$-$\varepsilon$ EVM overpredicts the absolute power outside the wake region compared with results of the $k$-$\varepsilon$-$f_P$ EVM and LES. This is caused by the fact that Method I uses the axial induction to predict the power and that the axial induction predicted by the $k$-$\varepsilon$ EVM does not correspond to one calculated by $k$-$\varepsilon$-$f_P$ EVM and LES.

From the present work, it can be concluded that the best setup for double wake RANS simulations is the use of the proposed Method II together with the $k$-$\varepsilon$-$f_P$ EVM. Hence, the correct thrust force and power is calculated inside and outside the wake region.

## Acknowledgments

This work is supported by the Center for Computational Wind Turbine Aerodynamics and Atmospheric Turbulence funded by the Danish Council for Strategic Research, grant number 09-067216. Computational resources were provided by DCSC and the DTU central computing facility.

# 6

# PAPER III: THE $k$-$\varepsilon$-$f_P$ MODEL APPLIED TO WIND FARMS


## Abstract

The recently developed $k$-$\varepsilon$-$f_P$ eddy viscosity model is applied to one on-shore and two off-shore wind farms. The results are compared with power measurements and results of the standard $k$-$\varepsilon$ eddy viscosity model. In addition, the wind direction uncertainty of the measurements is used to correct the model results with a Gaussian filter. The standard $k$-$\varepsilon$ eddy viscosity model underpredicts the power deficit of the first downstream wind turbines, whereas the $k$-$\varepsilon$-$f_P$ eddy viscosity model shows a good agreement with the measurements. However, the difference in the power deficit predicted by the turbulence models becomes smaller for wind turbines that are a located further downstream. Moreover, the difference between the capability of the turbulence models to estimate the wind farm efficiency reduces with increasing wind farm size and wind turbine spacing.


## 6.1 Introduction

Wind turbine wakes have a high impact on wind energy production because wake deficits can cause 10% to 20% losses in the annual energy of wind farms[6,24] and the wake turbulence can decrease the lifetime of wind turbine blades. It is therefore important to be able to predict the wake effects in wind farms during the design phase. Hence, reliable and relatively fast methods are necessary that can predict wake deficits and wake turbulence. Engineering wake models have shown to be fast, i.e. the N.O. Jensen model;[25] however, their accuracy is not always guaranteed.[21] Fuga[39] is a fast linearized computational fluid dynamics (CFD) method that shows good agreement with measurements of wind farms, which is mainly applicable to power predictions but not for wind turbine loads. High fidelity nonlinear CFD methods, as large-eddy simulation (LES), have proven to produce reliable results in terms of loads and power, which compare well with field measurements.[69] However, LES is an expensive method that is not suited to

This chapter has been published as: van der Laan, M. P., Sørensen, N. N., Réthoré, P.-E., Mann, J., Kelly, M. C., Troldborg, N., Hansen, K. S. and Murcia, J. P. The $k$-$\varepsilon$-$f_P$ model applied to wind farms. *Wind Energy*, Published online, 2014.

predict wake effects in large wind farms for the purpose of wind farm design. Reynolds-averaged Navier Stokes (RANS), is a nonlinear CFD method that is roughly three orders of magnitude less expensive in computational effort than LES.[76] The reduction in computational effort is achieved by two properties of RANS. First of all, RANS is a steady state calculation, whereas LES is transient. Secondly, RANS requires smaller grid sizes than LES. If the rotor geometry is represented by an actuator disk method,[37] one could use a grid around the wind turbine that is uniformly spaced in all directions. In this setup, a RANS grid typically needs 10 cells to cover a rotor diameter,[76] whereas a LES grid can require 30,[77] to resolve the wake accurately. Hence, the RANS grid becomes 27 times smaller than the LES grid. Unfortunately, RANS methods utilize a high level of turbulence modeling, which has proven to dominate the flow solution.[46] A commonly used turbulence model is the $k$-$\varepsilon$ eddy viscosity model (EVM), which is known to underpredict the wake deficit and overpredict the turbulence intensity in the near wake.[10,16,45,46,76] The problem of the $k$-$\varepsilon$ EVM is related to the fact that the eddy viscosity coefficient $C_\mu$ is a constant. In previous work, the $k$-$\varepsilon$ EVM was extended with a scalar relation for $C_\mu$.[76] The scalar relation, called $f_P$, is a function of the local shear, which reduces the eddy viscosity for a high shear. Since the near wake is characterized by a high local shear, $f_P$ decreases the eddy viscosity in the near wake and delays the wake recovery. The extended $k$-$\varepsilon$ EVM, hereafter labeled as $k$-$\varepsilon$-$f_P$ EVM, has been shown to compare well with LES in terms of the velocity deficit of a single wakes[76,77] and double wakes.[75] In addition, the $k$-$\varepsilon$-$f_P$ EVM does not overpredict the turbulence intensity in the near wake.

In the current work, the performance of the $k$-$\varepsilon$-$f_P$ EVM is tested for wind farm simulations. Power measurements from one on-shore and two off-shore wind farms are used to compare with the predicted power of the $k$-$\varepsilon$-$f_P$ EVM and the original $k$-$\varepsilon$ EVM. The three test cases are described in Section 6.2. The methodology and the results of the simulations are discussed in Section 6.3.

## 6.2 Test cases

The $k$-$\varepsilon$-$f_P$ EVM and the standard $k$-$\varepsilon$ EVM are applied to three wind farms: the on-shore Wieringermeer wind farm and two off-shore wind farms, Lillgrund and Horns Rev. In total, seven test cases are defined and are listed in Table 6.1. The test cases differ in the total ambient turbulence intensity at hub height $I_{H,\infty} \equiv \sqrt{2/3k}/U_{H,\infty}$ (with $k$ as the turbulent kinetic energy), free-stream velocity $U_{H,\infty}$ at hub height $z_{H,\infty}$, rotor diameter $D$ and wind turbine spacing. Note that the total ambient turbulence intensity is derived from the streamwise ambient turbulence intensity $I_{H,\infty,u} \equiv \sigma_u/U_{H,\infty}$ that is known from the measurements. By using the ratios of the standard deviations of three

velocity components that have been summarized by Panofsky and Dutton:[40]

$$\frac{\sigma_v}{\sigma_u} = 0.8, \qquad \frac{\sigma_w}{\sigma_u} = 0.5, \tag{6.1}$$

the total ambient turbulence intensity can be written as follows:

$$I_{H,\infty} = I_{u,H,\infty}\sqrt{\frac{1}{3}\left(1 + 0.8^2 + 0.5^2\right)} \approx 0.8 I_{u,H,\infty}. \tag{6.2}$$

The first two test cases are derived from the Wieringermeer wind farm that correspond to a low and a high ambient turbulence intensity. Test cases 3 to 6 are based on the Lillgrund wind farm. The Lillgrund test cases differ in wind direction and wind turbine spacing. Cases 3 and 5 correspond to the wind directions that are aligned with the rows, whereas cases 4 and 6 represent wind directions in which the rows are 15° misaligned with respect to the incoming flow. The misaligned cases are referred as the staggered cases. Only one test case is derived from the measurements of the Horns Rev wind farm. The three wind farms are further described in the sections below.

Table 6.1: Summary of cases and corresponding input parameters for numerical computations. wd = wind direction.

| Case | Description | Measurement data | $I_{H,\infty}$ ($I_{u,H,\infty}$) [%] | $U_{H,\infty}$ [m/s] | $D$ [m] | $z_H$ [m] | Spacing [m/D] |
|---|---|---|---|---|---|---|---|
| | | On-shore wind farm Wieringermeer | | | | | |
| 1 | low $I_{H,\infty}$ | wd=275°±15° | 2.4 (3) | 6.59 | 80 | 80 | 3.8 |
| 2 | high $I_{H,\infty}$ | wd=275°±15° | 9.6 (12) | 8.35 | 80 | 80 | 3.8 |
| | | Off-shore wind farm Lillgrund | | | | | |
| 3 | South-west, aligned | wd=222°±2.5°, rows B, D | 4.8 (6) | 9 | 92.6 | 65 | 4.3 |
| 4 | South-west, staggered | wd=207°±2.5°, rows B, D | 4.8 (6) | 9 | 92.6 | 65 | |
| 5 | South-east, aligned | wd=120°±2.5°, rows 4, 6 | 4.8 (6) | 9 | 92.6 | 65 | 3.2 |
| 6 | South-east, staggered | wd=105°±2.5°, rows 4, 6 | 4.8 (6) | 9 | 92.6 | 65 | |
| | | Off-shore wind farm Horns Rev | | | | | |
| 7 | West, aligned | wd=270°±2.5°, rows 1-8 | 5.6 (7) | 8 | 80.0 | 70 | 7.0 |

### 6.2.1 On-shore wind farm: Wieringermeer

A row of five wind turbines is located in Wieringermeer, a farmland area in the north west of the Netherlands. The wind turbine row is part of the Wind Turbine Test Site, owned and maintained by ECN. The layout of the five 2.5 MW Nordex N80 wind turbines is sketched in Figure 6.1. The row is orientated along the 275°wind direction and

the spacing between the wind turbines is around 3.8D. The wind turbines have a rotor diameter and hub height of 80 m. Schepers[57] et al. published the results of nearly 5 years of measurements and the 10 min averaged data is available for the present research. From these measurements, a data set is derived with wind directions of $275^\circ \pm 15^\circ$. A meteorological mast is located south of the wind turbine row and it is used to derive the undisturbed conditions.

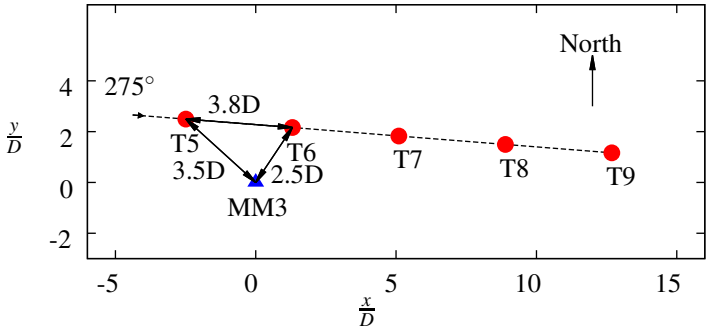


Figure 6.1: Sketch of wind turbines (red dots) and meteorological mast (blue triangle) at ECN Wind Turbine Test Site Wieringermeer.

The power curve and the power coefficient $C_P$ provided by the wind turbine manufacturer are used. The thrust coefficient $C_T$ is not given by Nordex; however, measurements of $C_T$ derived from the tower bending moment and PHATAS[33] calculations of $C_T$ are available from Schepers.[56] The two methods agree well, except for the low wind speeds where the uncertainty in the measured tower bending moment is high. Therefore, the calculated $C_T$ will be used. $C_T$ and $C_P$ are plotted in Figure 6.2. Only the range of the rotational speed is known, $\Omega = 10.9 - 19.1$ rpm, not the full curve. In order to simulate the wind turbine row in CFD with rotational forces, the full rotations per minute curve as function of the ambient velocity at hub height is necessary. Since the $C_P$ region is relatively flat for wind speeds between 7 and 11 m/s (as indicated by the gray area in Figure 6.2), it is assumed that the wind turbine starts rotating at the maximum of 19.1 rpm at the end of the flat $C_P$ region (11 m/s), and that the rotational speed is constant up to the cut-out wind speed of 25 m/s. The rotational speed below wind speeds of 11 m/s is derived by assuming a constant Tip Speed Ratio ($TSR$): $TSR \equiv \Omega(\pi/60)D/U = 7.27$, until the minimum rotational speed of 10.9 rpm is reached at a wind speed of 6.28 m/s. The estimated rotational speed curve is shown in Figure 6.2.

The meteorological mast is used to calculate the stability from the Monin-Obukhov length $L$, that is derived from the bulk Richardson number. This method is described in more detail in the work of Hansen et al.[22] While bulk Richardson numbers cannot be reliably used to model the wind field,[27,55] they allow useful classification of stability

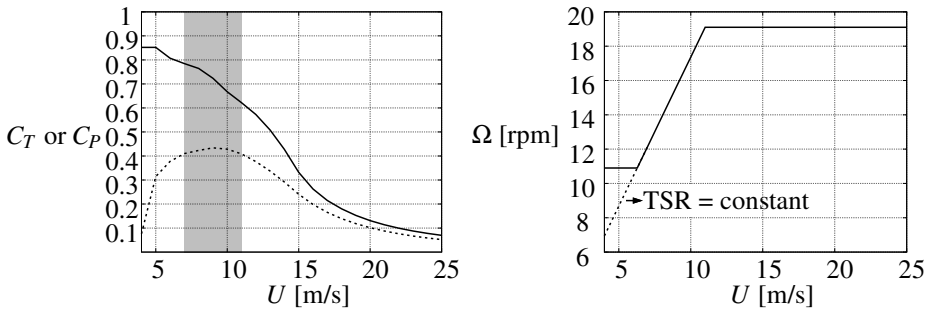


Figure 6.2: Nordex N80 wind turbine. Left: $C_T$ (solid line) and $C_P$ (dashed line). Gray area indicates the flat $C_P$ region. Right: estimated rotational speed Ω using constant TSR (dashed line).

regimes. Seven stability classes are defined in Table 6.2 and the probability of each class is plotted in Figure 6.3, for cases 1 and 2. In the low ambient turbulence case (case 1), the atmospheric boundary layer (ABL) is stable to very stable, whereas the high ambient turbulence case (case 2) corresponds to near unstable ABL. The present CFD simulations can only model a neutral ABL; hence, it should not be expected that the CFD simulations can predict the wake effects in the row of wind turbines for case 1. Nevertheless, case 1 is interesting to investigate how large the disagreement between measurements and simulations is, that is associated with not modeling atmospheric stability. Since case 2 is close to neutral, a better agreement between the CFD and the measurements should be expected compared with case 1.

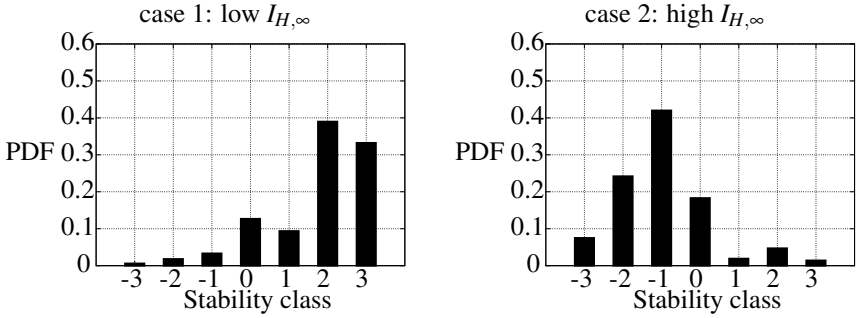


Figure 6.3: Probability of stability classes for the on-shore wind farm Wieringermeer.

Table 6.2: Definition of stability classes.

| Class | Range of $L$ [m] | Description |
|---|---|---|
| -3 | $-100 \leq L < -50$ | Very unstable |
| -2 | $-200 \leq L < -100$ | Unstable |
| -1 | $-500 \leq L < -200$ | Near unstable |
| 0 | $\|L\| > 500$ | Neutral |
| 1 | $200 \leq L \leq 500$ | Near stable |
| 2 | $50 \leq L < 200$ | Stable |
| 3 | $10 \leq L < 50$ | Very stable |

### 6.2.2 Off-shore wind farm: Lillgrund

Lillgrund is an off-shore wind farm, located south of the Øresund bridge that connects Copenhagen (Denmark) with Malmö (Sweden). Figure 6.4 shows the layout of the off-shore wind farm, which is unique because of the missing wind turbines in the middle of the wind farm. In addition, the wind turbine spacing of 3.2D and 4.3D for the wind direction of 120° and 222°, respectively, is much smaller than the typical spacing of off-shore wind farms that are built today. Note that a spacing of 3.3D is often reported in literature,[13,15,20,21] however, a spacing of 300 m is reported in the official drawing of the wind farm layout, which corresponds to a spacing of 3.24D. The narrow spacing is the result of a design change towards maximum power instead of wind farm efficiency, in which larger wind turbines were selected than initially planned, without changing the original layout of the wind farm.[15] Hence, wind turbine wake effects are relatively large in the wind farm (around 30% loss in terms of the annual energy production[15]), which makes it an interesting case to simulate with CFD.

The wind farm includes 48 Siemens SWT-2.3-93 wind turbines that have a rated power of 2.3 MW, a rotor diameter of 92.6 m and a hub height of 65 m. The $C_T$, $C_P$ and $\Omega$ curves are provided by Hansen[20] and are shown in Figure 6.5. Dahlberg[15] and Hansen[21] derived a measurement set from the SCADA data of Lillgrund. The results of Dahlberg[15] correspond to a data set that is gathered over a period of 2 years using 1 min bins, in which the yaw positions are not known. Dahlberg assumed zero yaw errors and used the nacelle positions to estimate the wind direction. More recently, Hansen extracted a data set of 3 years using 10 min bins, in which the yaw sensors are calibrated against the power deficit peak of a nearby wind turbine, a method that is further described in the work of Barthelmie et al.[5] Subsequently, the wind direction is derived from the calibrated yaw sensors. The reference wind turbines that are used for determining the wind direction are A5 and C1 for the wind directions 120° and 222°, respectively. The data set of Hansen is chosen in the current research. Unfortunately, the meteorological mast shown in Figure 6.4 was not available for the period that Hansen used to process

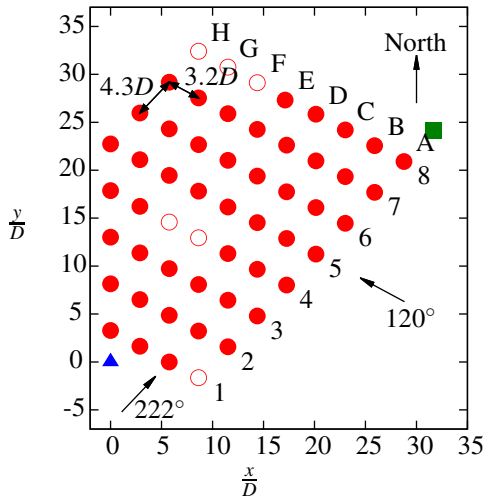


Figure 6.4: Wind farm layout: wind turbines (red dots), grid position without a wind turbine (red circles), transformer station (green square) and meteorological mast (blue triangle). Distances are normalized with the rotor diameter of the Siemens SWT-2.3-93 wind turbine: $D = 92.6$ m.

the measurements. Therefore, Hansen derived the undisturbed wind speed from the power curve, shown in Figure 6.5. With this method, Hansen selected power data that corresponds to an estimated undisturbed wind speed of $9 \pm 0.5$ m/s. It should be noted that a group of wind turbines is used to determine the free-stream wind speed, which consists of row 1 and row A for the south-westerly and south-easterly wind directions, respectively. The meteorological mast was erected prior to the wind farm installation, which provides a data set of more than 2 years. From these measurements, Bergström[8] estimated the streamwise turbulence intensity to be around 6%. The lack of an upstream meteorological mast makes it impossible to investigate the atmospheric stability.

### 6.2.3 Off-shore wind farm: Horns Rev

Horns Rev is an off-shore wind farm located 14 km from the West coast of Denmark. The wind farm has a rated power of 160 MW, and it consists of $10 \times 8$ Vestas V80 wind turbines. The rectangular layout is shown in Figure 6.6. The wind turbine spacing is 7D in the aligned wind directions of 90°-270° and 174°-354°. With a rotor diameter of 80 m, the wind farm fits into a square of dimensions $5.5 \times 4$ km$^2$. The power coefficient, thrust coefficient and the rotational speed of the V80 wind turbine are provided by Vestas and are shown in Figure 6.7.

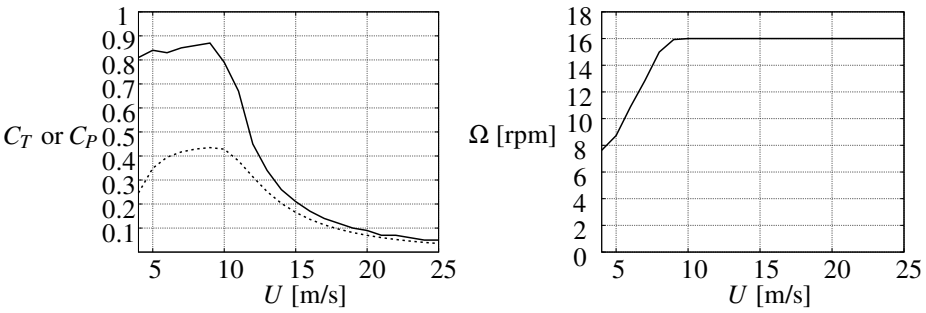


Figure 6.5: Siemens SWT-2.3-93 wind turbine. Left: $C_T$ (solid line) and $C_P$ (dashed line). Right: rotational speed $\Omega$.

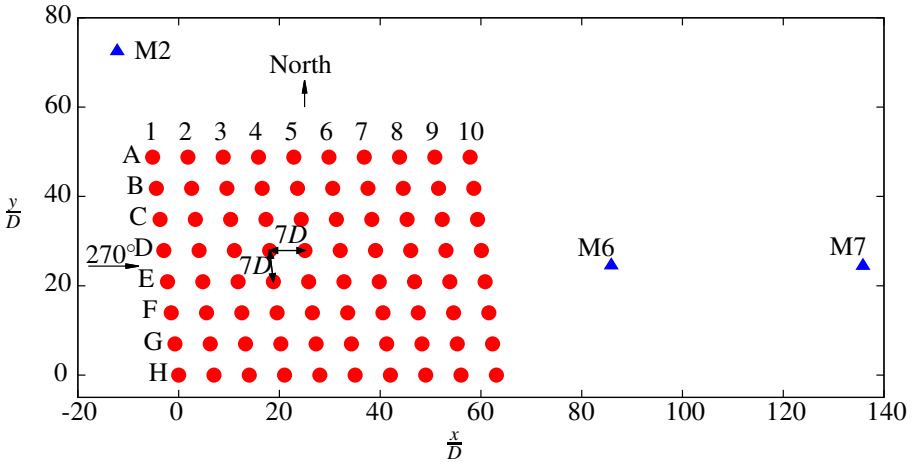


Figure 6.6: Wind farm layout: wind turbines (red dots) and meteorological masts M2, M6 and M7 (blue triangles). Distances are normalized with the rotor diameter of the Vestas V80 wind turbine: $D = 80$ m.

The power measurements for a wind direction of $270° \pm 2.5°$ and a period between 2005 and 2009 are made available by Hansen and the results are presented in Hansen et al.[22] Non-neutral atmospheric stability data has been filtered out using the same method as discussed in Section 6.2.1. Three stability classes are present in the filtered set: near unstable, neutral and near stable. It is found that further reducing the data set, i.e. only allow the neutral class, leads to too few observations.

Unfortunately, the quality of the measurements from meteorological mast M2 shown in Figure 6.6, is low. Therefore, the free-stream conditions are estimated from wind

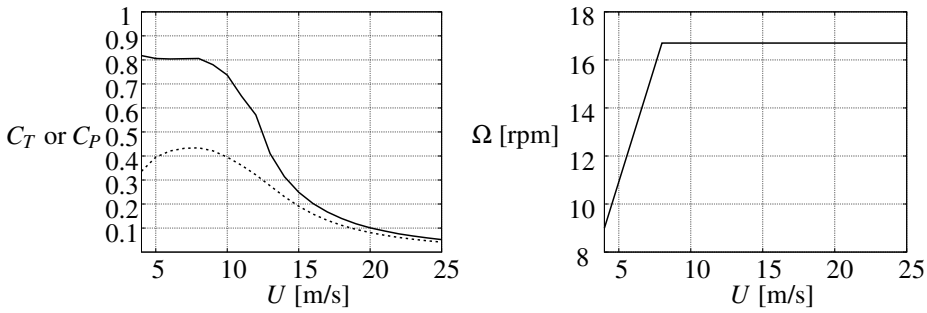


Figure 6.7: Vestas V80 wind turbine. Left: $C_T$ (solid line) and $C_P$ (dashed line). Right: rotational speed.

turbine G1. The wind direction is obtained from the yaw sensor of wind turbine G1, which is calibrated with the power ratio of G2/G1. The free-stream velocity is obtained from power measurements of wind turbine G1 and the power curve from Figure 6.7.

## 6.3 Simulations

The simulations of the test cases from Table 6.1 are discussed in Sections 6.3.1 and 6.3.2, in which the method and the results are discussed, respectively.

### 6.3.1 Method

The flow is solved by EllipSys3D, the CFD code of DTU Wind Energy, which is originally developed by Sørensen[62] and Michelsen.[36] The SIMPLE algorithm[41] is chosen to solve the RANS equations. A QUICK scheme[32] is used to discretize convective terms. Since the flow variables are stored in a co-located manner, decoupling of the pressure and body forces can occur. This problem is solved with a modified Rhie-Chow algorithm.[47,49]

The flow domain of the Wieringermeer cases is shown in Figure 6.8, however, the flow domain definition applies for all cases. A region with a uniform spacing of D/10 in all direction is defined, which is labeled as the wake domain. The cell spacing is based on a grid dependency study of single wind turbine simulations.[76] The wake domain is placed in the center of the flow domain with respect to the $xy$-plane. Near the wall, at $z = 0$, the cells are refined in the $z$-direction, towards a first-cell height of 0.5 m. The cells are stretched outside the wake domain with a maximum growth ratio of 1.2. The dimensions of the flow domain and the wake domain are listed in Table 6.3. The horizontal dimensions of the flow domain that are used for the relatively large wind farms (Lillgrund and Horns Rev), are set to a 1000D, to avoid the influence of the symmetric

boundaries at $y = 0$, $y = L_y$ and outlet boundary at $x = L_x$, at which a fully developed flow is assumed. The neutral log law solution is set at the inlet boundaries, located at $x = 0$ and $z = L_z$:

$$U(z) = \frac{u_*}{\kappa} \ln\left(\frac{z}{z_0}\right), \qquad k = \frac{u_*^2}{\sqrt{C_\mu}}, \qquad \varepsilon = \frac{u_*^3}{\kappa z}, \tag{6.3}$$

where $U$ is the streamwise velocity, $u_*$ is the friction velocity, $\kappa = 0.4$ is the Von Kármán constant, $z_0$ is the roughness height, $k$ is the turbulent kinetic energy and $\varepsilon$ is the turbulent dissipation. The log law solution is retained throughout the domain by setting a rough wall condition at $z = 0$. At the rough wall, the wall stress and the turbulent dissipation are prescribed, while a Neumann condition is used for the turbulent kinetic energy.[63]

It is common to set the ambient turbulence intensity at hub height $I_{H,\infty}$ by changing $C_\mu$ in:

$$I_{H,\infty} \equiv \frac{\sqrt{\frac{2}{3}k}}{U_{H,\infty}} = \frac{\kappa\sqrt{\frac{2}{3}}}{\ln\left(\frac{z_H}{z_0}\right)\sqrt[4]{C_\mu}}. \tag{6.4}$$

However, the $f_P$ function in the $k$-$\varepsilon$-$f_P$ EVM also changes because it is a function of $C_\mu$, i.e. $f_P = f_P(\sigma/\tilde{\sigma})$ and $\tilde{\sigma} = 1/\sqrt{C_\mu}$, with $\sigma$ as the shear parameter: $\sigma \equiv \frac{k}{\varepsilon}\sqrt{(U_{i,j})^2}$ and $\tilde{\sigma}$ as the shear parameter present in the log law solution. In previous work,[74] it has been found that the $f_P$ function enhances the wake recovery for higher values of $C_\mu$ (corresponding to a lower $I_{H,\infty}$), which is unphysical. To avoid this problem, $z_0$ is set to obtain the desired $I_{H,\infty}$ through equation (6.4), while leaving $C_\mu$ constant.[76] Subsequently, the friction velocity is adapted to set the free-stream velocity at hub height $U_{H,\infty}$, using equation (6.3). Hence, $z_0$ and $u_*$ are not based on the field measurements, and the resulting simulated velocity profile deviates from the measured velocity profile; however, the differences in the rotor area are small. The maximum difference in velocity in the rotor area between the present method and in a method where the standard offshore roughness height of $10^{-4}$ m is used, is less than 0.2% and 2% for the Horns Rev and the Lillgrund cases, respectively. In the Wieringermeer case with low ambient turbulence (case 1), the maximum difference in velocity in the rotor area is 7%, using a field roughness height of 5 cm. This indicates that the low turbulence intensity in case 1 is not caused by the rough wall because the turbulent adapted roughness height $z_0$ is much smaller than one that is based on the location of the field measurements. It is most likely that the ambient turbulence intensity in case 1 is dominated by the stable atmospheric conditions, as also discussed in Section 6.2.1 and shown in Figure 6.3.

#### 6.3.1.1 Turbulence models

The standard $k$-$\varepsilon$ EVM from Launder and Spalding[31] and the $k$-$\varepsilon$-$f_P$ EVM from van der Laan et al.[76] are applied to the wind farm simulations. The turbulence models can only

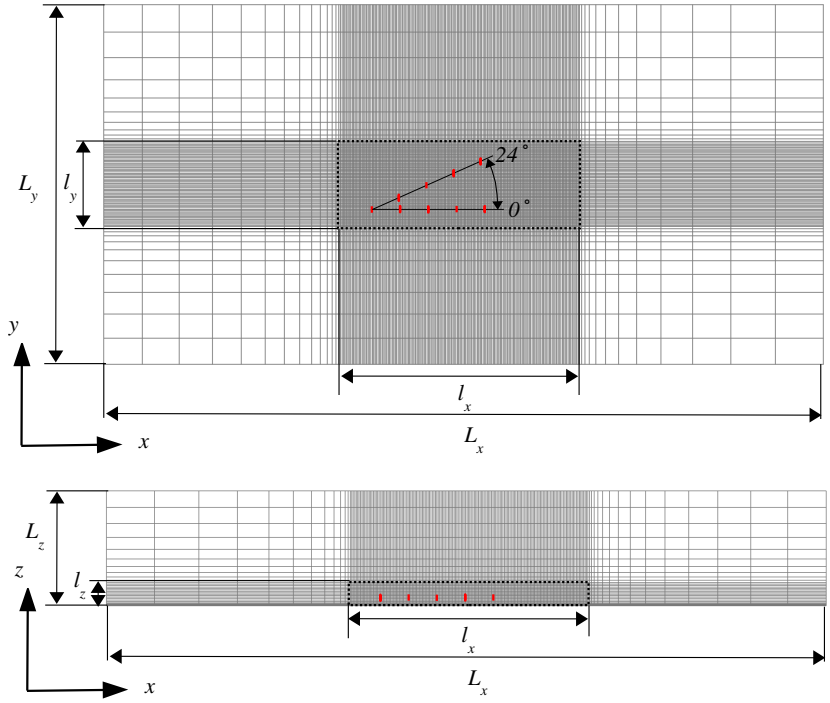


Figure 6.8: General computational domain. Top: top view. Bottom: side view. Dashed black box marks the wake domain. ADs are illustrated as red boxes. AD setup shown corresponds to test cases 1 and 2. One in every two nodes is shown.

Table 6.3: RANS flow domain definition of all test cases. Domain sizes are normalized by the rotor diameter $D$.

| | | Flow domain | | | Wake domain | | | Total number of cells |
|---|---|---|---|---|---|---|---|---|
| Case | Description | $L_x$ | $L_y$ | $L_z$ | $l_x$ | $l_y$ | $l_z$ | - |
| 1-2 | Wieringermeer | 100 | 50 | 16 | 33 | 11.5 | 3 | $3.9 \times 10^6$ |
| 3-6 | Lillgrund | 1000 | 1000 | 10 | 55 | 50 | 4 | $2.4 \times 10^7$ |
| 7 | Horns Rev | 1000 | 1000 | 10 | 108 | 102 | 4 | $8.5 \times 10^7$ |

predict isotropic Reynolds-stresses $\overline{u_i' u_j'}$ because the Boussinesq approximation[9] is used:

$$\overline{u_i' u_j'} = \frac{2}{3} k \delta_{ij} - \nu_T \left( U_{i,j} + U_{j,i} \right), \tag{6.5}$$

where $\delta_{ij}$ is the Kronecker delta, $U_{i,j}$ are the mean velocity gradients and $\nu_T$ is the turbulent eddy viscosity:

$$\nu_T = C_\mu f_P \frac{k^2}{\varepsilon}, \tag{6.6}$$

with $C_\mu$ as a constant and $\varepsilon$ as the turbulent dissipation. In the standard $k$-$\varepsilon$ EVM $f_P = 1$ and the effective eddy viscosity coefficient $C_\mu f_P$ is a constant. In the $k$-$\varepsilon$-$f_P$ EVM, $f_P$ is a scalar function that depends on the local shear parameter: $\sigma \equiv \frac{k}{\varepsilon}\sqrt{(U_{i,j})^2}$. The effective eddy viscosity coefficient, $C_\mu f_P$ is variable, instead of a constant, which is the only difference with the standard $k$-$\varepsilon$ EVM. The scalar function $f_P$ in the $k$-$\varepsilon$-$f_P$ EVM is defined as follows:

$$f_P(\sigma/\tilde{\sigma}) = \frac{2f_0}{1+\sqrt{1+4f_0(f_0-1)\left(\frac{\sigma}{\tilde{\sigma}}\right)^2}},\ f_0 = \frac{C_R}{C_R-1}, \tag{6.7}$$

with $\tilde{\sigma}$ as the shear parameter in an idealized (logarithmic) neutral atmospheric surface layer and $C_R$ is a calibration parameter. In the neutral log law solution, $f_P = 1$ because $\sigma = \tilde{\sigma}$. In regions with a high shear parameter, i.e. $\sigma > \tilde{\sigma}$, $f_P < 1$ and the turbulent eddy viscosity from equation (6.6) is decreased. The near wind turbine wake is characterized by high velocity gradients, where $\sigma \gg \tilde{\sigma}$. As a result, the $k$-$\varepsilon$-$f_P$ EVM delays the wake recovery compared with the standard $k$-$\varepsilon$ EVM. It should be noted that $C_R$ controls the magnitude of the delayed wake recovery. The constant $C_R$ is calibrated against LES for eight different single wind turbine cases, in previous work.[76] The same transport equations for $k$ and $\varepsilon$ are used in both turbulence models:

$$\begin{aligned}\frac{Dk}{Dt} &= \nabla\cdot\left[\left(\nu+\frac{\nu_T}{\sigma_k}\right)\nabla k\right] + \mathscr{P} - \varepsilon,\\ \frac{D\varepsilon}{Dt} &= \nabla\cdot\left[\left(\nu+\frac{\nu_T}{\sigma_\varepsilon}\right)\nabla \varepsilon\right] + \left(C_{\varepsilon,1}\mathscr{P} - C_{\varepsilon,2}\varepsilon\right)\frac{\varepsilon}{k},\end{aligned} \tag{6.8}$$

where $\mathscr{P}$ is the turbulent production, $\nu$ is the kinematic molecular viscosity and $C_{\varepsilon,1}, C_{\varepsilon,2}$, $\sigma_k$, $\sigma_\varepsilon$ are constants. The values of the constants are listed in Table 6.4. Note that $C_\mu$ is based on atmospheric measurements of Panofsky and Dutton,[40] as proposed by Richards and Hoxey [50] and $C_{\varepsilon,1}$ is adapted to maintain the log law solution: $\sqrt{C_\mu}\sigma_\varepsilon(C_{\varepsilon,1} - C_{\varepsilon,2}) + \kappa^2 = 0$.

Table 6.4: Model constants.

| $C_R$ | $C_\mu$ | $C_{\varepsilon,1}$ | $C_{\varepsilon,2}$ | $\sigma_k$ | $\sigma_\varepsilon$ | $\kappa$ |
|---|---|---|---|---|---|---|
| 4.5 | 0.03 | 1.21 | 1.92 | 1.00 | 1.30 | 0.40 |

#### 6.3.1.2 Wind turbine modeling

The wind turbine geometry is not modeled in the grid. Instead, the actuator disk (AD) method[37,46,48] is employed to model wind turbine forces. The AD extracts momentum from the Navier-Stokes equations by the addition of a momentum sink. Troldborg et al.[73] showed that the difference in wake flow between a full rotor simulation and an AD simulation is negligible, as long as inflow turbulence is present. In the current work, the AD forces are modeled with the AD Variable Scaling Method, as described in van der Laan et al.[75] The AD Variable Scaling Method is suited to model the AD forces of interacting wind turbines because the AD forces are a function of local AD velocity. The method uses reference blade force distributions, which are statically scaled with the rotor diameter. In addition, the reference blade force distributions are dynamically scaled during the simulation, with the local AD velocity averaged over the rotor disk $\langle U_{AD} \rangle$, and with calibrated scaling coefficients $C_T^*$, $C_P^*$ and $\Omega^*$. These scaling coefficients correspond to the thrust coefficient $C_T$, the power coefficient $C_P$ and the rotational speed $\Omega$, respectively, as function of $\langle U_{AD} \rangle$. The relationship of $C_T^*$, $C_P^*$ and $\Omega^*$ with $\langle U_{AD} \rangle$ is derived from a calibration procedure, in which a number of single AD simulations are carried out, which corresponds to a range of free-stream velocities, e.g. between 4-25 m/s with a uniform spacing of 1 m/s. Assuming that $C_T$, $C_P$ and $\Omega$ are known as function of the free-stream velocity, the total AD forces in each single wind turbine simulation is prescribed and $\langle U_{AD} \rangle$ can be extracted from the converged solution.

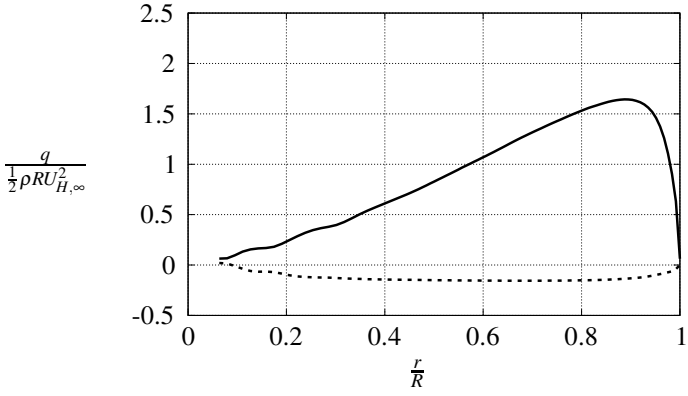


Figure 6.9: Calculated tangential $q_T$ (dashed line) and normal force $q_N$ (solid line) distributions [n/m].

In the present work, the calibration procedure is carried out for the following wind turbines: N80, SWT-2.3-93 and V80. The blade force distributions from a full rotor detached-eddy simulation of the NREL-5 MW wind turbine are used as the reference blade force distributions, that are scaled as mentioned previously. The results for the

normal and the tangential force distribution are plotted in Figure 6.9. The numerical setup for the single wind turbine simulations is described in detail in the work of van der Laan et al.[76] The calibration procedure is repeated whenever the turbulence model or the ambient turbulence intensity is changed. The calibration of the Nordex N80 wind turbine from Section 6.2.1 is shown in Figure 6.10. The calibrated scaling coefficients $C_T^*$, $C_P^*$ and $\Omega^*$ are plotted as function of the averaged AD velocity $\langle U_{AD} \rangle$. Four different calibrations are given that differ in turbulence model and ambient turbulence intensity. $C_T^*$ and $C_P^*$ show sensitivity to the turbulence model and ambient turbulent intensity, in the low wind speed range, as also observed in previous work.[75] The sensitivity in turbulence model is caused by the fact that the $k$-$\varepsilon$ EVM underpredicts the induction compared with LES, whereas the $k$-$\varepsilon$-$f_P$ EVM predicts a correct induction. Therefore, it is important to redo the calibration if the turbulence model or the ambient turbulence intensity is changed. The calibration results of the other wind turbines are not given in the paper.

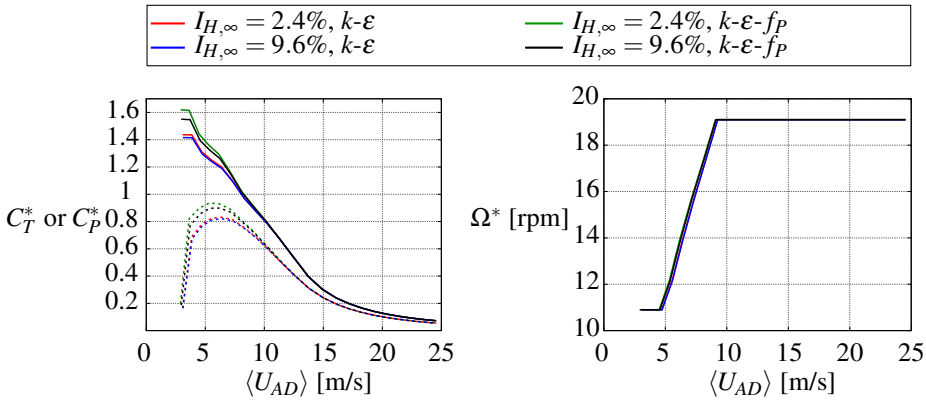


Figure 6.10: Nordex N80 wind turbine. Left: $C_T^*$ (solid line) and $C_P^*$ (dashed line). Right: rotational speed $\Omega^*$ in rpm.

#### 6.3.1.3 Post-processing for measurement uncertainty of the wind direction

Gaumond et al.[18] showed that the wind direction uncertainty is large in measurements that are processed with narrow wind direction bins. As a result, the measured power deficit decreases for a narrow wind direction bin that is aligned with the wind turbine rows, because power measurements outside the wind direction bin, which corresponds to partial or no wake conditions, are also included. Gaumond et al. argued to correct model results for wind direction uncertainty, such that a fair comparison with measurements can be made. Three sources of the wind direction uncertainty are identified by Gaumond et

al.:

1. The use of a yaw sensor to obtain the wind direction, instead of a direct measurement, i.e. a wind vane.

2. The spatial de-correlation of the reference wind direction measurement with respect to the undisturbed wind direction that is present far away from the reference location.

3. The change in wind direction due to large scale turbulence that is statistically not well represented within 10 min averages.

In the present work, the first two sources of wind direction uncertainty are estimated for the Horns Rev wind farm by investigating the standard deviation of the difference in the wind direction that is measured with a wind vane at the meteorological mast M2 $\theta_{\mathrm{M2,i}}$ with the wind direction that is computed from the yaw sensors $\theta_{\mathrm{yaw,i}}$:

$$\Delta\theta_{\mathrm{i}} = \theta_{\mathrm{yaw,i}} - \theta_{\mathrm{M2,i}} \tag{6.9}$$

Note that the meteorological mast M2 is located 2 km north from the Horns Rev wind farm, as shown in Figure 6.6, and was only partly available during the period of the power measurements. In Figure 6.11, the standard deviation of $\Delta\theta_{\mathrm{i}}$ is plotted against the distance between M2 and the individual wind turbines $\Delta L$. The data collapses to a linear curve:

$$\sigma_{\Delta\theta} = 3.5 \times 10^{-4}\Delta L + 2.1. \tag{6.10}$$

Figure 6.11 indicates that the wind direction uncertainty increases linearly with the distance from the reference location. In addition, even if M2 was placed at the location of the yaw sensor, still a difference in standard deviation of $2.1^\circ$ is predicted. In other words, the standard deviation of the wind direction is increased by $2.1^\circ$ because a yaw sensor is used to measure the wind direction, instead of a wind vane.

Ott and Nielsen[39] argued that the wind direction uncertainty, associated with the large scale turbulence that is statistically not well represented within the 10 min averages: $\sigma_{\mathrm{lst}}$, can be estimated from the difference in consecutive 10 min averaged wind direction measurements. This idea is adapted in the present work, using all three meteorological masts at Horns Rev: M2, M6 and M7, as shown in Figure 6.6. For M2, $\sigma_{\mathrm{lst}}$ is obtained from a Gaussian fit of the distribution $\Delta\theta_{\mathrm{M2,i}}$:

$$\Delta\theta_{\mathrm{M2,i}} = \theta_{\mathrm{M2,i+1}} - \theta_{\mathrm{M2,i}}, \tag{6.11}$$

using the consecutive wind direction measurements $\theta_{\mathrm{M2,i}}$ and $\theta_{\mathrm{M2,i+1}}$. The data is filtered for outliers before the Gaussian fit is performed. The final results of the unfiltered distribution and the Gaussian fit for M2 is plotted in Figure 6.12. The exercise is repeated for M6 and M7 and the results for $\sigma_{\mathrm{lst}}$ are listed in Table 6.5.

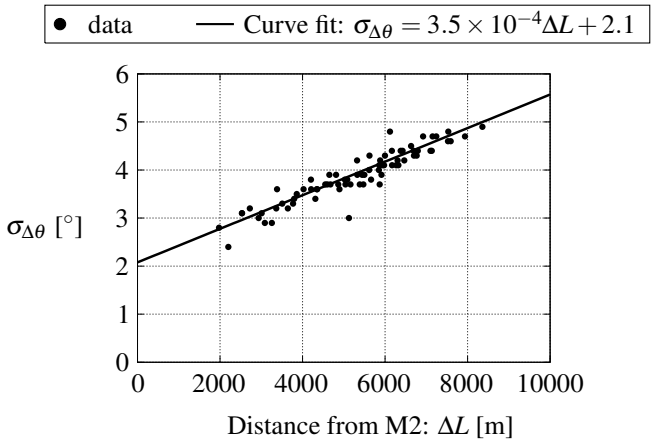


Figure 6.11: Difference in standard deviation beteen meteorological mast M2 and the yaw sensors of the wind turbines in Horns Rev.

We assume that all three sources of wind direction uncertainty can be written as a single standard deviation $\sigma_{\text{total}}$:

$$\sigma_{\text{total}} = \sqrt{\sigma_{\Delta\theta}^2 + \sigma_{\text{lst}}^2}. \tag{6.12}$$

The average result for $\sigma_{\text{lst}}$ is used (2.5°), as listed in Table 6.5.

Table 6.5: Estimation of $\sigma_{\text{lst}}$ for three different meteorological mast at Horns Rev.

| Meteorological mast | M2 | M6 | M7 | Average |
|---|---|---|---|---|
| $\sigma_{\text{lst}}$ [°] | 2.6 | 2.5 | 2.5 | 2.5 |

It is believed that the wind direction uncertainty in the Lillgrund and Wieringermeer wind farms is lower than the Horns Rev wind farm because both the Lillgrund and Wieringermeer wind farms are much smaller than Horns Rev. Since the wind direction in the Lillgrund wind farm is still based on yaw sensors, it is assumed that the standard deviation in wind direction due to using yaw sensors is 2.1°, i.e. substituting $\Delta L = 0$ in equation (6.10). The effect of de-correlation is neglected because the reference wind turbine that is used to obtain the wind direction is always the first wind turbine in a neighboring row with respect to the rows of the Lillgrund test cases (i.e A5 for rows 4 and 6, and C1 for rows B and D). In other words, the distance of the measured power deficits and the reference wind turbine is small. The Wieringermeer wind farm uses wind vanes that are positioned at a nearby meteorological mast; hence the wind direction uncertainty

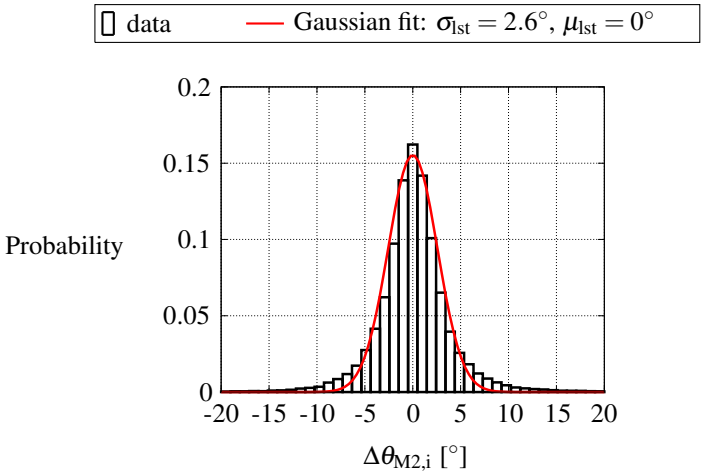


Figure 6.12: The difference of consecutive 10 min wind direction averages measured at meteorological mast M2.

due to using a yaw sensor can be neglected. The estimated wind direction uncertainty per wind farm is summarized in Table 6.6. The three sources of wind direction uncer-

Table 6.6: Estimated wind direction uncertainty of the measurements.

| | | Wind direction uncertainty in terms of $\sigma$ [°] | | | |
|---|---|---|---|---|---|
| Case | Description | De-correlation | Yaw | Turbulence | Total |
| 1-2 | Wieringermeer | - | - | 2.5 | 2.5 |
| 3-6 | Lillgrund | - | 2.1 | 2.5 | 3.3 |
| 7 | Horns Rev | $3.5 \times 10^{-4}\Delta L + 2.1$ | | 2.5 | $\sqrt{(3.5 \times 10^{-4}\Delta L + 2.1)^2 + 2.5^2}$ |

tainty are taken into account by averaging the simulated wind directions with a Gaussian filter,[18] in which the standard deviation is based on the total standard deviation listed in Table 6.6. The Gaussian averaging is performed over an interval of $\pm 3\sigma_{total}$ such that 99.7% of the Gaussian filter is applied.

### 6.3.2 Results and Discussion

The results of the on-shore Wieringermeer wind farm and the two off-shore wind farms Lillgrund and Horns Rev, are discussed separately in the proceeding sections. In all power deficit plots, two results for each RANS turbulence model are shown; the solid line represents the result of each single wind direction, and the dashed line is the post-

processed result of a Gaussian average using an interval of $\pm 3\sigma_{\text{total}}$. This Gaussian averaging represents the wind direction uncertainty that is typically observed in measurements that are processed with narrow wind direction bins, as explained in Section 6.3.1.3. The wind farm efficiency of all test cases is evaluated in Section 6.3.2.4.

#### 6.3.2.1 Wieringermeer

In Figure 6.13, the power deficit is plotted as function of westerly wind directions for each of the four downstream wind turbines (T6, T7, T8 and T9) separately, for low and high ambient turbulence intensities (cases 1 and 2 of Table 6.1). The power deficit of each wind turbine is normalized by the first turbine in the row (T5). The numerical computations using the standard $k$-$\varepsilon$ EVM and $k$-$\varepsilon$-$f_P$ EVM are carried out for relative wind directions between 0°and 24°, with a constant interval of 3°. The results of the negative relative wind direction range (-24°to 0°) is the mirror image of the results of the positive relative wind directions. Hence, the effect of rotation on the power deficit is assumed to be negligible. This assumption is tested at the end of the present section. The Gaussian-averaged results, indicated with the dashed lines, are computed using an interval of $\pm 3\sigma_{\text{total}}$ with a standard deviation $\sigma_{\text{total}}$ of 2.5°, as motivated in Section 6.3.1.3. The power deficits are compared with measurements from Wieringermeer,[57] as described Section 6.2. In case 1, the measured power deficit of the second wind turbine (T6) is very large because of the low ambient turbulence of 2.4%. The calculated power deficit predicted by the $k$-$\varepsilon$-$f_P$ EVM is even larger than the measured one; however, the power deficit becomes more comparable when the wind direction uncertainty is taken into account. Further downstream, the $k$-$\varepsilon$-$f_P$ EVM underpredicts the power deficit compared with the measurements. In addition, the measured width of the power deficit is larger than the calculated one. Figure 6.3 from Section 6.2.1 shows that the low ambient turbulence in the measurements is caused by very stable atmospheric conditions, which are not modeled in the current RANS simulations. A stable ABL suppresses the generation of wake turbulence and it delays wake recovery, which increases the power deficit. Hence, the stability is a plausible cause for the difference between the measured and the calculated power deficit.

The standard $k$-$\varepsilon$ EVM is known to underpredict the velocity deficit in the near wake.[10,16,45,46,76] The underpredicted velocity wake deficit translates to an overprediction of the power of the second wind turbine in case 1 by 40%, at a relative wind direction of 0°. The difference between the standard $k$-$\varepsilon$ EVM and the $k$-$\varepsilon$-$f_P$ EVM becomes smaller at the third wind turbine (T7) and further downstream, the turbulence models predict similar power deficits. This effect is caused by the increasing turbulence intensity in the (merged) wakes because the single wake simulations have shown that the difference between the RANS turbulence models is small, when a high ambient turbulence intensity is set at the inlet.[76] In addition, an other mechanism minimizes the difference between the turbulence models in terms of the power deficit of the wind

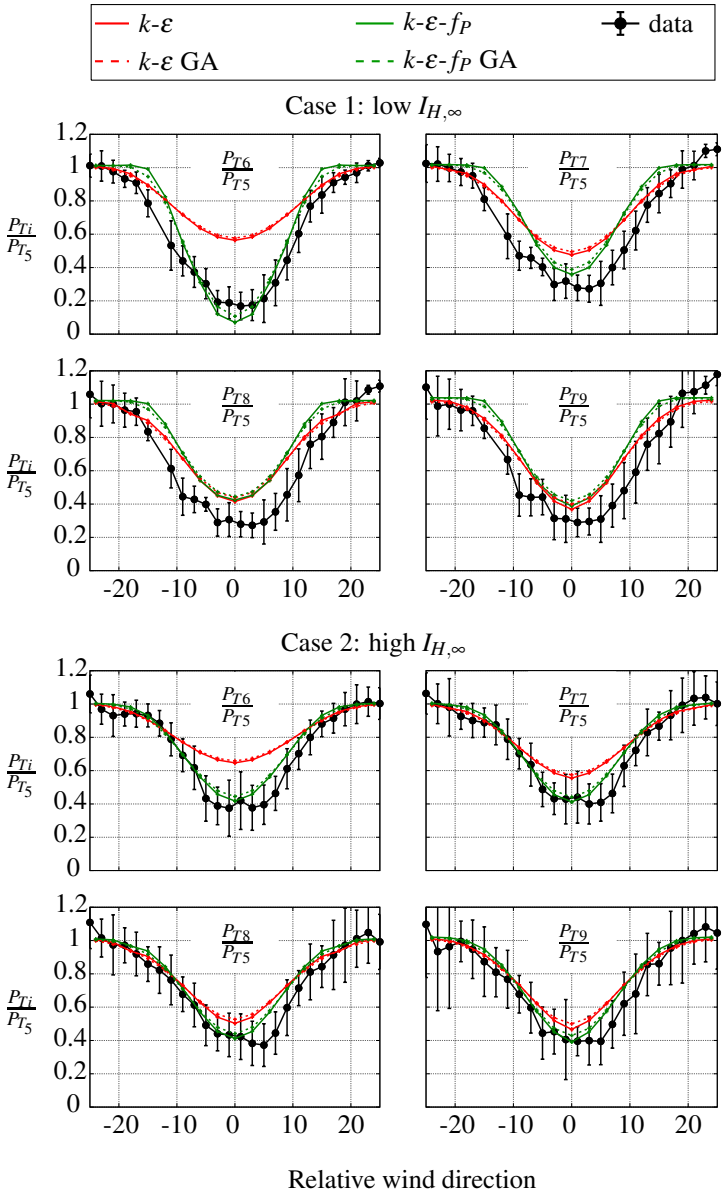


Figure 6.13: Power deficit in the Wieringermeer wind farm as function of wind direction. Measurements include error bars of one standard deviation. Solid and dashed lines: solution without and with Gaussian averaging (GA), respectively.

turbines further downstream in the row. Since the $k$-$\varepsilon$ EVM is overpredicting the wake recovery of the first wind turbine wake, the second wind turbine experiences larger forces and its corresponding wake deficit is compensated. Hence, the difference in forcing of the second wind turbine results in a smaller difference between the turbulence models, in terms of power deficit of the third wind turbine in the row.

In case 2, the ambient turbulence intensity is four times higher than in case 1. The power deficits predicted by the $k$-$\varepsilon$-$f_P$ EVM is in reasonable agreement with the measurements. The influence of the Gaussian averaging is small because the wind direction uncertainty is estimated to be low. In addition, the difference between the standard $k$-$\varepsilon$ EVM and the $k$-$\varepsilon$-$f_P$ EVM, in terms of the power deficit of the second wind turbine, is smaller than observed in case 1 because of the higher ambient turbulence intensity.

A linear averaged power deficit is shown in Figure 6.14 for the low and high ambient turbulence cases. The measured average consists of three bins between relative wind directions of -3° and 3°, and the average from the simulations represents three simulations corresponding to relative wind directions of -3°, 0° and 3°. Figure 6.14 emphasizes the statements that the standard $k$-$\varepsilon$ EVM significantly underpredicts the power deficit at the second wind turbine, the $k$-$\varepsilon$-$f_P$ EVM compares much better with the measurements and both turbulence models show an underpredicted power deficit for the further downstream wind turbines for case 1. Figure 6.14 also shows that the measured power deficit in case 2 has almost already reached its asymptotic value at the second wind turbine, since the power deficit does not change much at the other downstream wind turbines. In other

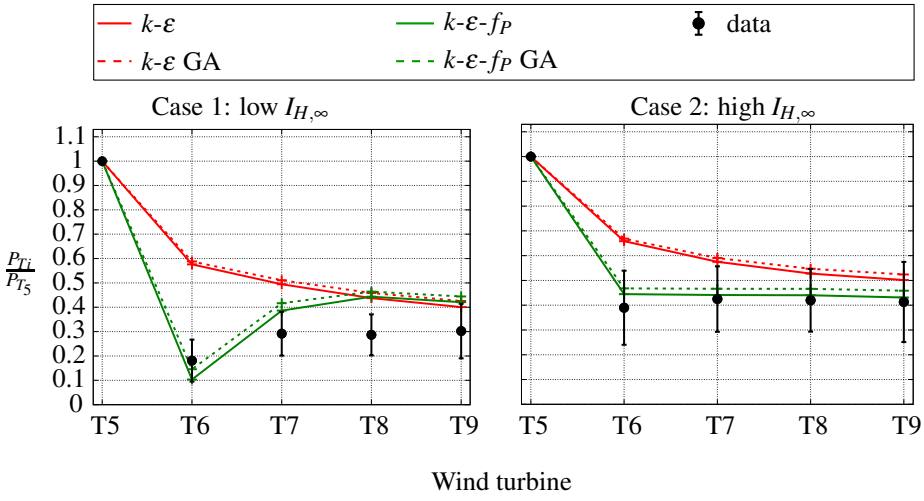


Figure 6.14: Power deficit in the Wieringermeer wind farm for a wind direction of 275°±3°. Measurements include error bars of one standard deviation. Solid and dashed lines: solution without and with Gaussian averaging (GA), respectively.

words, the momentum loss caused by wake effects, is not further increased when going downstream in the row, because it is in equilibrium with the transport of fresh momentum coming from the undisturbed flow.

The effect of the rotational forces is shown in Figure 6.15, in which the power deficit is plotted with and without rotational forces. Only the $k$-$\varepsilon$-$f_P$ EVM is used in the comparison and for the simulations without rotational forces a re-calibrated $C_T^*$ is used to scale the reference thrust force distribution. Hence, the two methods would predict the same power when they are applied to a single wind turbine simulation. Figure 6.15 shows that there is a very weak influence of the rotational force on the power deficit. This observation is in contradiction with the work of Wu and Porté-Agel,[80] who argued that the rotational forces do influence the power deficit in their LES AD computations of the Horns Rev wind farm. However, Wu and Porté-Agel used different methods to represent the variable forces in the LES simulation with [actuator-disk models (ADM)-R] and without rotation (ADM-NR), which may have led to an unfair comparison. In the ADM-R simulation, the forces were based on tabulated airfoil data, as introduced by Sørensen and Shen.[61] The ADM-NR simulations were carried out by a uniformly distributed AD, where the total force is based on a variable thrust force coefficient, using the thrust curve and a local free-stream velocity $U_{H,\infty}$, that is estimated from the local induction factor $a_x$ and an averaged velocity at the AD $\langle U_{AD} \rangle$: $U_{H,\infty} = \langle U_{AD} \rangle / (1 - a_x)$. This method leads to an overprediction of the power, because the free-stream velocity is overestimated, as shown by van der Laan et al.[75] Hence, the difference between ADM-R and ADM-NR in terms of power deficit is most likely caused by the difference in AD force method, rather than the effect of wake rotation.

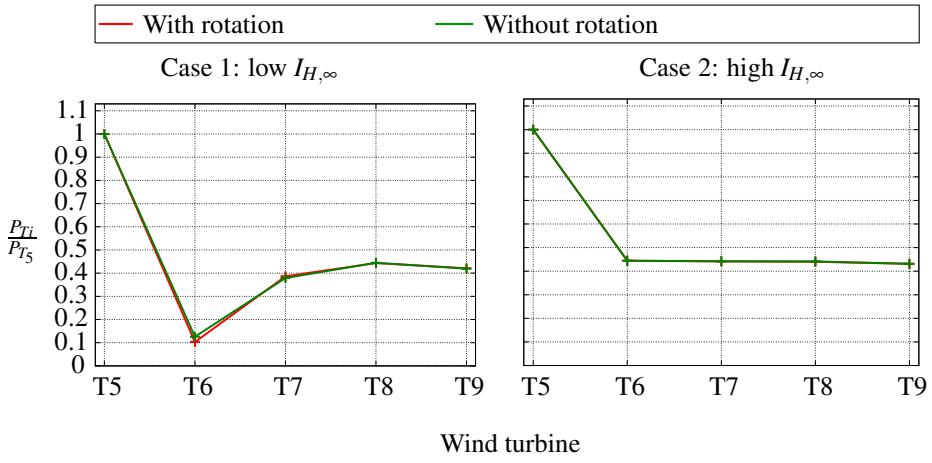


Figure 6.15: Effect of rotational forces on power deficit in the Wieringermeer wind farm for a wind direction of 275°±3°.

#### 6.3.2.2 Lillgrund

The results of four wind directions, corresponding to the four wind farm cases of Table 6.1, are shown in Figure 6.16. For each case, the power deficit of two rows are plotted; rows B and D for cases 3 and 4 and rows 6 and 4 for cases 5 and 6, respectively. Rows D and 4 are rows where one and two wind turbines are missing. Cases 3 and 5 correspond to wind directions that are aligned with the rows, whereas cases 4 and 6 represent a staggered layout in which the wind directions are 15° misaligned with the direction of the rows. All plots in Figure 6.16 include results of the standard $k$-$\varepsilon$ EVM and the $k$-$\varepsilon$-$f_P$ EVM. For both models, two results are shown: the power deficit without Gaussian averaging (solid line) and with Gaussian averaging (dashed line). The Gaussian averaging represents the wind direction uncertainty, and it is performed over an interval of $\pm 3\sigma_{\text{total}}$ with $\sigma_{\text{total}} = 3.3°$, as discussed in Section 6.3.1.3. The RANS-based models are Gaussian averaged using seven relative wind directions between -15° and 15°, with uniform interval of 5°. In addition, the LES results of Churchfield et al.[13] are included for case 3, which corresponds to a single high fidelity simulation. Note that the LES data from Churchfield et al. is re-normalized with the power of the first wind turbine, such that a comparison can be made with the results of the RANS models. The wind direction uncertainty is not taken into account in the LES data from Churchfield et al. because only one wind direction was simulated.

First, the Gaussian-averaged results are discussed. In all aligned cases (cases 3 and 5), the standard $k$-$\varepsilon$ EVM is not able to predict the measured power deficit of the second wind turbine, whereas the $k$-$\varepsilon$-$f_P$ EVM shows favorable results. In addition, all cases show that the power deficit calculated by the $k$-$\varepsilon$ EVM approaches the one of $k$-$\varepsilon$-$f_P$ EVM when going downstream. These two observations were also made in the results of the on-shore wind farm Wieringermeer, in Section 6.3.2.1. In one of the staggered cases (case 4), both the $k$-$\varepsilon$ EVM and the $k$-$\varepsilon$-$f_P$ EVM underpredict the measured power deficit, especially for row B. The two downstream wind turbines in row B do not experience large wake effects in the simulations for a wind direction of 207°, because the upstream wake does not hit the two downstream wind turbines. This effect is more pronounced in the $k$-$\varepsilon$-$f_P$ EVM because the standard $k$-$\varepsilon$ EVM has too wide wakes, as observed in single wind turbine simulation in previous work.[76] It is plausible that the uncertainty of the wind direction is larger for case 4, although further downstream in rows B and D, the simulated power deficit of the wind turbines will not be improved by a Gaussian filter with a larger standard deviation.

In general, the Gaussian averaging improves the results of the $k$-$\varepsilon$-$f_P$ EVM. However, the measured power deficit of the second wind turbine of case 5 is best predicted without Gaussian averaging.

Comparing the available LES results with the measurements and other models for case 3, shows that the LES predicts a reasonable wake deficit for row B. However, the LES underpredicts the asymptotic value of the power deficit, as also noted by Churchfield et al.[13] The LES overpredicts the power deficit in row D for the upstream turbine

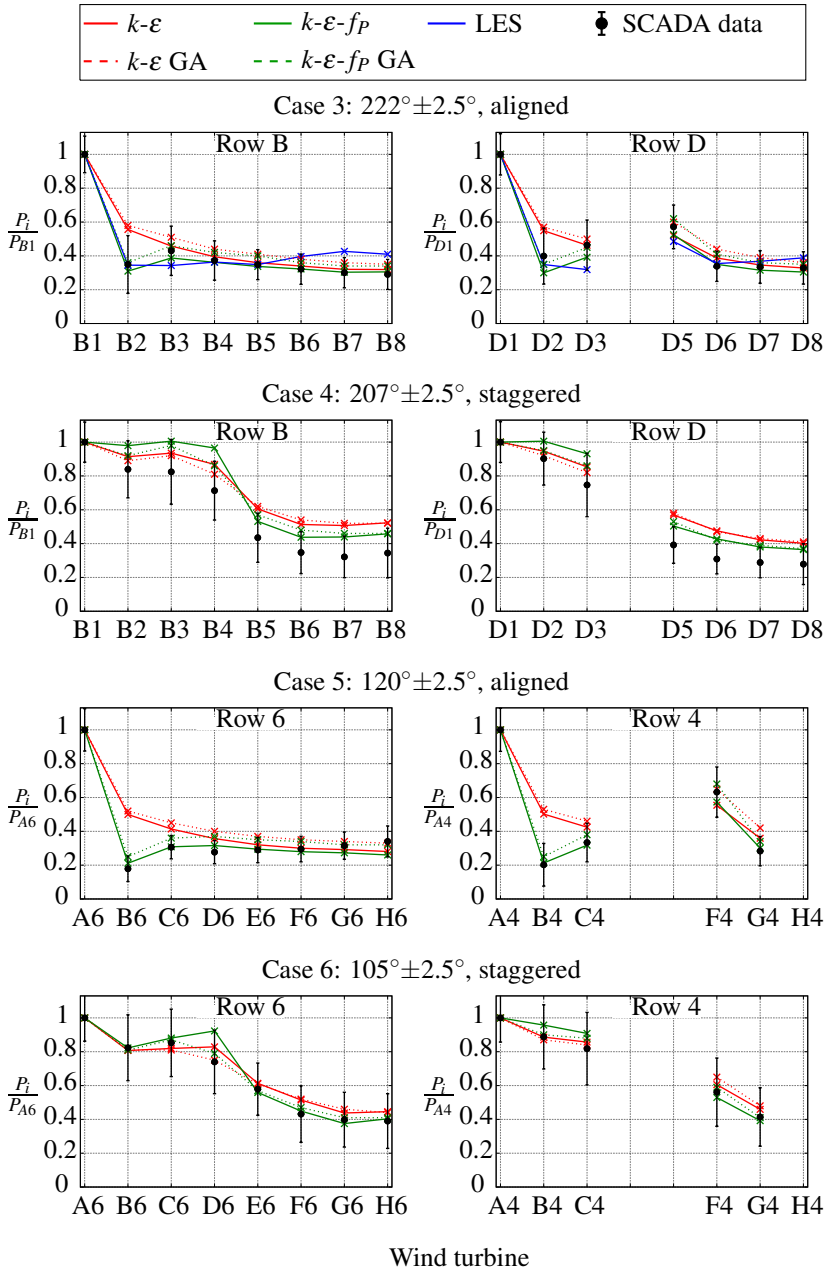


Figure 6.16: Power deficit in rows in the Lillgrund wind farm for aligned flow directions. LES from Churchfield[13]. Dashed lines include Gaussian averaging (GA).

of the gap, and the asymptotic value is again not reached. The reasons for these differences are not clear. One should keep in mind that only one LES simulation is shown (without the Gaussian averaging), which makes it difficult to compare with measurements that include wind direction uncertainty.

#### 6.3.2.3 Horns Rev

The measured power deficit in the Horns Rev wind farm is plotted in Figure 6.17 for all eight rows, for a wind direction of $270^\circ \pm 2.5^\circ$. The measured power deficit is compared with two results of the $k$-$\varepsilon$ EVM and the $k$-$\varepsilon$-$f_P$ EVM, where the dashed and solid lines represent the power deficit with and without Gaussian averaging. The Gaussian averaging is meant to include the wind direction uncertainty of the measurements in the simulations, as discussed in Section 6.3.1.3. The variable standard deviation of the wind direction uncertainty from Table 6.6 is applied. In order to perform the Gaussian averaging over an interval of $\pm 3\sigma_{\text{total}}$, nine different wind directions are simulated per turbulence model, covering a wind direction range of 250°-290°, with a uniform interval of 5°. Without the Gaussian filter, the power deficit of the second wind turbine, calculated by the $k$-$\varepsilon$-$f_P$ EVM, is overpredicted in all rows. When the results are Gaussian averaged, the measured power deficit of the second wind turbine and the one calculated by the $k$-$\varepsilon$-$f_P$ EVM compare better, but there is still an overprediction that continues to exist for the wind turbines further downstream. Possibly, the wind direction uncertainty is higher than estimated in Section 6.3.1.3. In addition, the Gaussian-averaged results would improve if the wind direction uncertainty of Gaumond et al.[18] is applied. Gaumond et al. used a row specific $\sigma_{\text{total}}$, that is obtained from fitting the power deficit of each second wind turbine in a row, predicted by Fuga,[39] to the measurements. This shows that the results are very sensitive to the estimation of the wind direction uncertainty.

It should be noted that the standard deviation of the power measurements is almost twice as high as the data set that includes all atmospheric stability classes. This is not understood because it is expected that the variability of the measurement would decrease when non-neutral atmospheric stability data is filtered out. Note that the average number of observations per wind turbine is 45, which is believed to be sufficient.

As seen in the other test cases, the $k$-$\varepsilon$ EVM predicts a lower power deficit compared the $k$-$\varepsilon$-$f_P$ EVM, for the second wind turbine in each row, although the difference is not as large as seen in the Lillgrund wind farm (Figure 6.16). This is caused by the larger wind turbine spacing in Horns Rev (7D) compared with the one in the Lillgrund wind farm (3.2D-4.3D). From the third wind turbine in the row and further downstream, the difference between the turbulence models is negligible.

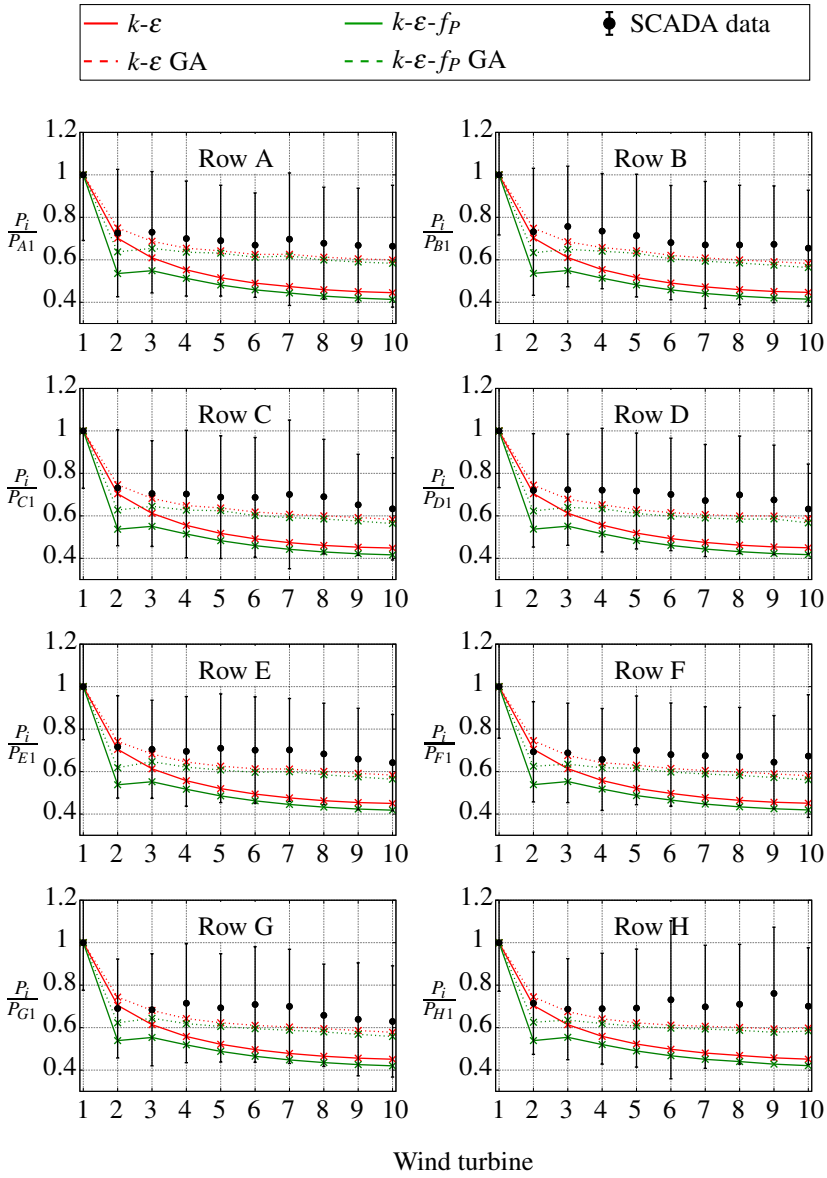


Figure 6.17: Power deficit in rows in the Horns Rev wind farm for a wind direction of $270^\circ \pm 2.5^\circ$. Dashed lines include Gaussian averaging (GA).

#### 6.3.2.4 Wind farm efficiency

The wind farm efficiency is defined as the total power of the wind farm normalized by the power of a single wind turbine without wake effects and the number of wind turbines. In Figure 6.18, the wind farm efficiency is plotted for all test cases employing the $k$-$\varepsilon$ EVM and $k$-$\varepsilon$-$f_P$ EVM, and the results are compared with the measurements. Note that the wind farm efficiency is only computed for the simulated wind directions, which does not cover the full wind rose. Results with and without Gaussian averaging are shown with the non-filled and filled symbols, respectively. In the first Wieringermeer case, the calculated wind farm efficiencies do not compare well with the measurements, because the effect of atmospheric stability is not modeled. The second Wieringermeer

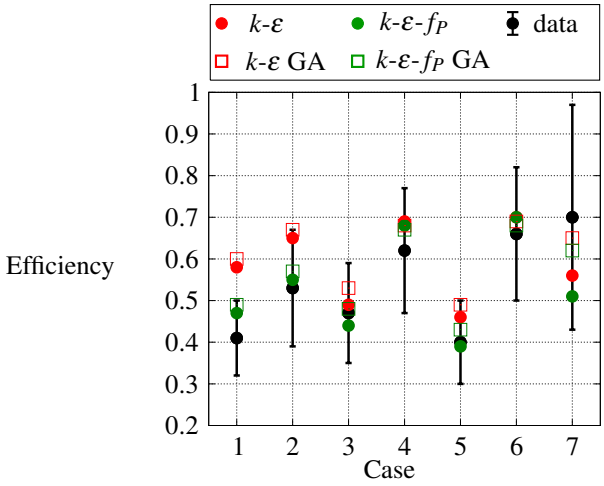


Figure 6.18: Wind farm efficiency for all test cases. Cases 1 and 2: Wieringermeer with low and high ambient turbulence intensity, cases 3 and 5: Lillgrund with aligned wind directions, with 4.3D and 3.2D spacing. Cases 4 and 6: Lillgrund with staggered wind directions, with 4.3D and 3.2D spacing. Case 7: Horns Rev. Non-filled symbols include Gaussian averaging (GA).

case corresponds to a data set that is measured in near neutral ABL conditions. The $k$-$\varepsilon$-$f_P$ EVM compares well with the measurements in this test case, whereas, the $k$-$\varepsilon$ EVM overpredicts the measured wind farm efficiency. In the Lillgrund cases (cases 3 to 6), the results of the $k$-$\varepsilon$ EVM and the $k$-$\varepsilon$-$f_P$ EVM, are reasonably close to the measured values. The effect of Gaussian averaging in the Wieringermeer and Lillgrund cases is small. However, the Gaussian averaging improves the results significantly in the Horns Rev test case (case 7). In addition, the difference between the two turbulence models is negligible. The Horns Rev test case shows that the effect of Gaussian averaging is larger

than the difference in wind farm efficiency between the two turbulence models. This indicates that the post-processing of the CFD results is just as important as the choice of turbulence model.

The difference in wind farm efficiency between the $k$-$\varepsilon$ EVM and the $k$-$\varepsilon$-$f_P$ EVM becomes smaller with increasing wind farm size and wind turbine spacing. In the Wieringermeer cases (5 wind turbines, with 3.8D spacing), the aligned Lillgrund case (48 wind turbines, with 3.2D-4.3D spacing) and the Horns Rev wind farm (80 wind turbines, with 7D spacing), the difference in wind farm efficiency without Gaussian averaging is 0.10-0.11, 0.05-0.07, 0.04, respectively. In addition, for wind directions that correspond to staggered configurations, the difference in wind farm efficiency is negligible, as observed in the staggered Lillgrund cases 4 and 6. In other words, if the annual energy of a large wind farm needs to be calculated, the standard $k$-$\varepsilon$ EVM will show a similar performance as the $k$-$\varepsilon$-$f_P$ EVM, because the complete wind rose calculation corresponds to mostly wind directions with staggered configurations and the difference in power is negligible at the third or fourth wind turbine in a row.

#### 6.3.2.5 Computational cost

Table 6.7: Average computational effort in CPU hours per wind direction.

| Case | Description | Cores | Cells | CPU $k$-$\varepsilon$ | CPU $k$-$\varepsilon$-$f_P$ |
|---|---|---|---|---|---|
| 1-2 | Wieringermeer | $1\times12$ | $3.9\times10^6$ | 14 | 15 |
| 3-6 | Lillgrund | $6\times12$ | $2.4\times10^7$ | 250 | 309 |
| 7 | Horns Rev | $9\times12$ | $8.5\times10^7$ | 1043 | 1527 |

The simulations are computed on a user-shared PC cluster that has 80 nodes with two Intel Xeon X5650 processors with six cores each. The clock frequency of a core is 2.66 GHz. The total number of CPU hours (number of CPUs $\times$ wall clock time) per wind direction is listed in Table 6.7 and it is computed as an average of all simulated wind directions. The $k$-$\varepsilon$-$f_P$ EVM needs more iterations than the $k$-$\varepsilon$ EVM, especially for the case with aligned wind directions, which causes the difference in computational cost. However, the $k$-$\varepsilon$-$f_P$ EVM is still three orders of magnitude cheaper compared with LES. For example, Churchfield et al.[13] performed LES of the Lillgrund wind farm that took approximately 1,000,000 CPU hours using 4096 cores to simulate only 10 min of realtime data for a single wind direction. It should be noted that Churchfield et al. used the actuator line technique,[61] which requires a finer cell spacing than the AD method, and the time step is limited to the tip speed (Churchfield et al. used $D/53 = 1.75$ m and 0.015 s, respectively). If ADs are used, a significant reduction in computational cost be achieved because a cell spacing of $D/30$ is required if the Reynolds-stresses in the wake need to be resolved, and even $D/15$ is enough if only the mean velocity deficit is

desired.[77] In addition, the time step in an AD-LES is not limited to the tip speed, but it can be set to a Courant-Friedrichs-Lewy condition that is based on the free-stream velocity.

## 6.4 Conclusions

The performance of the $k$-$\varepsilon$ EVM and the $k$-$\varepsilon$-$f_P$ EVM is evaluated for seven test cases corresponding to three different wind farms: Wieringermeer, Lillgrund and Horns Rev. The wind direction uncertainty of the measurements is used to correct the model results with a Gaussian filter, such that a fairer comparison can be made between the measurements and simulations. For wind directions that are aligned with the wind turbine rows, the $k$-$\varepsilon$ EVM underpredicts the power deficit at the second wind turbines in all cases, whereas the $k$-$\varepsilon$-$f_P$ EVM shows comparable results with the measurements. Further downstream, at the third or fourth wind turbine in a row, the RANS turbulence models predict similar power deficits.

The two Wieringermeer cases imply that the effect of wake rotation on the power deficit is negligible. However, it is believed that the atmospheric stability does influence the power deficit, since the $k$-$\varepsilon$-$f_P$ EVM is not able to predict the power deficit in Wieringermeer wind farm that is measured in stable atmospheric conditions.

The Horns Rev case shows that the effect of Gaussian averaging on the power deficit and wind farm efficiency is larger than the difference between $k$-$\varepsilon$ EVM with the $k$-$\varepsilon$-$f_P$ EVM. Hence, the choice of turbulence model is just as important as including the wind direction uncertainty in the post-processing. Therefore, it is important to further investigate the methods that are used to estimate the wind direction uncertainty.

The difference in wind farm efficiency predicted by the $k$-$\varepsilon$ EVM and the $k$-$\varepsilon$-$f_P$ EVM becomes smaller for increasing wind turbine spacing and wind farm size. In addition, the difference between the prediction of the two models is small for wind directions that are misaligned with respect to the wind turbine rows. Hence, it is expected that the $k$-$\varepsilon$ EVM and the $k$-$\varepsilon$-$f_P$ EVM will predict similar values of the annual energy production for large wind farms with relatively large wind turbine spacing.

## Acknowledgments

This work is supported by the Center for Computational Wind Turbine Aerodynamics and Atmospheric Turbulence funded by the Danish Council for Strategic Research, grant number 09-067216. Computational resources were provided by DCSC and the DTU central computing facility. The authors would like to acknowledge J. G. Schepers for providing the measurement data and feedback on the results of these measurements.

# 7

# CONCLUSIONS AND FUTURE PERSPECTIVES

## 7.1 Conclusions

Wind turbine wakes in wind farms can cause power losses and increased blade fatigue loads. It is therefore important to accurately and efficiently calculate the effects of wakes during the design phase of a wind farm. The characteristics of a wind turbine wake, e.g. velocity deficit and Reynolds-stresses, are driven by turbulent processes because the Reynolds number is high. Therefore, an accurate turbulence model is necessary in order to simulate wind turbine wakes in Reynolds-averaged Navier-Stokes (RANS) methods. When the widely used $k$-$\varepsilon$ eddy viscosity model (EVM) is used, the velocity deficit is underpredicted in the near wake, which results in an underpredicted power deficit for the first downstream wind turbines in a wind farm. The $k$-$\varepsilon$ EVM performs poorly for wind turbine wakes because the adverse pressure gradient in front of the wind turbine is high, which leads to a flow that is far from equilibrium: $\mathscr{P}/\varepsilon >> 1$. Simple analysis shows that the eddy viscosity coefficient $C_\mu$ must be inversely proportional to $\mathscr{P}/\varepsilon$, which means that assumption of a constant $C_\mu$, as used in the $k$-$\varepsilon$ EVM, is violated. In addition, the $k$-$\varepsilon$ EVM overpredicts the streamwise Reynolds-stress in the wake, partly because it can only model isotropic turbulence since the stress-strain relation is linear, whereas the near wake and the atmospheric boundary layer (ABL) are characterized by anisotropic turbulence. This thesis is aimed to develop an efficient turbulence model for wind turbine wake simulations that can overcome the problems of the $k$-$\varepsilon$ EVM.

Nonlinear eddy viscosity models (NLEVMs) can predict anisotropic turbulence because the stress-strain relation is nonlinear. In addition, the effective eddy viscosity coefficient $C_\mu$ is variable, which typically decreases the eddy viscosity in regions with high velocity gradients, e.g. a wake. Therefore, NLEVMs have the potential to accurately predict the velocity deficit and Reynolds-stresses. Unfortunately, NLEVMs can show numerically unstable behavior for wind turbine wake simulations and even for flows with merely uniform terrain. This behavior becomes worse when higher order NLEVMs are used or when fine cell spacing is applied, which makes it impossible to numerically verify an NLEVM with a grid refinement study. In addition, the variable $C_\mu$ relation makes it impossible to set the free-stream turbulence intensity with $C_\mu$, as performed in the standard $k$-$\varepsilon$ EVM. It is therefore, recommended to set the turbulence intensity through other parameters, e.g. the roughness height.

When the nonlinear terms of the cubic NLEVM of Apsley and Leschziner are neglected, a linear $k$-$\varepsilon$ EVM with a variable $C_\mu$ remains, which is labeled as the $k$-$\varepsilon$-$f_P$

EVM. The variable part of $C_\mu$ is described by $f_P$, which is a scalar function of local velocity gradients. The $f_P$ function contains a constant $C_R$ that is calibrated with large-eddy simulation (LES) for 8 different single wind turbine cases. The $k$-$\varepsilon$-$f_P$ EVM predicts near wake velocity deficits that are much closer to field measurements and LES, compared to the standard $k$-$\varepsilon$ EVM. In addition, the $k$-$\varepsilon$-$f_P$ EVM is as robust and numerically stable as the standard $k$-$\varepsilon$ EVM. Since the stress-strain relation of the $k$-$\varepsilon$-$f_P$ EVM is linear, only isotropic turbulence can be predicted and the individual Reynolds-stress components in the wake are not improved compared the $k$-$\varepsilon$ EVM.

When wind turbines in wind farms are represented by interacting actuator disks (AD), the variable loading is not trivial. Different variable AD force methods can produce different power deficits, and the comparison of these methods in literature have led to the wrong conclusion that wake rotation has a large influence on the power deficit. Variable AD force methods that rely on tabulated airfoil data or a simple induction relation to estimate the free-stream velocity, often overpredict the power production. This problem can be solved by using a variable AD force method that uses alternative thrust and power coefficients as a function of the local AD velocity averaged over the disk area. The alternative thrust and power coefficients are derived from a number of single wind turbine wake simulations, where the loading is known from the original thrust and power coefficients that are a function of the free-stream. The new method also shows that the effect of wake rotation on the power deficit is negligible.

Wind farms measurements that are post-processed with narrow wind direction bins often suffer from a high uncertainty in the measured reference wind direction. As a result, the observed power deficit for a wind direction that is aligned with a row of wind turbines decreases, because measurements that correspond to staggered wake configurations are also included. In order to compare such a data set with wind farm simulations, it is necessary to simulate multiple wind directions and Gaussian average the results using the measured wind direction uncertainty.

In small wind farms with narrow wind turbine spacing, the $k$-$\varepsilon$-$f_P$ EVM compares better with field measurements than the standard $k$-$\varepsilon$ EVM, especially for the second wind turbine in a row, in aligned wake configurations. However, the $k$-$\varepsilon$-$f_P$ EVM and the $k$-$\varepsilon$ EVM produce similar power deficits at the third or fourth wind turbine in row and further downstream. In fact, both turbulence models show very similar results for large wind farms, large wind turbine spacing and staggered wake configurations. Hence, where the standard $k$-$\varepsilon$ EVM is problematic for single wind turbine simulations, it may not be a bad model to estimate the annual energy production of large wind farms with large wind turbine spacing.

## 7.2 Future perspectives

The outcome of the PhD work is a simple modification of the standard $k$-$\varepsilon$ EVM, called the $k$-$\varepsilon$-$f_P$ EVM, that enables the user to simulate the effect of wind turbine wakes in

wind farms, in terms of velocity and power deficits. Unfortunately, this new model cannot improve the prediction of individual Reynolds-stress components in the wake, which means that the blade fatigue loads that are induced by wake turbulence cannot be estimated accurately. It is necessary to include at least one second order term in the stress-strain relation, such that anisotropic turbulence can be simulated, which is important in the ABL and the wake. However, this single nonlinear term can produce numerically unstable behavior, as observed in the simulations employing NLEVMs. Hence, more research is necessary to develop a robust quadratic NLEVM.

Only neutral atmospheric stability is simulated in the current work. Measurements of the power deficit in a row of wind turbines in a stable ABL do not compare well with neutral RANS simulations employing the $k$-$\varepsilon$-$f_P$ EVM, in which only the free-stream turbulence intensity is set accordingly. This implies that atmospheric stability needs to be physically modeled, such that wake turbulence is either suppressed or enhanced.

The post-processing of wind farm simulations that are compared with measurements with narrow wind direction bins, has a larger impact on the power deficit than the choice of turbulence model. Hence, the post-processing method needs to be further investigated and standardized, especially how the wind direction uncertainty is obtained from the measurements.

The simplicity of the $k$-$\varepsilon$-$f_P$ EVM opens possibilities to apply it for other flows where the standard $k$-$\varepsilon$ EVM fails. For example the flow behind a (steep) hill or forest edge modeling. In any flow where the velocity gradients are high and the flow is locally far from equilibrium, i.e., $\mathscr{P}/\varepsilon >> 1$, the $k$-$\varepsilon$-$f_P$ EVM has the potential to improve the accuracy.

# Appendix A

## SUMMARY OF NLEVMS

The derived NLEVMs are written as:

$$\mathbf{a} = \sum_{\lambda=1}^{10} G^{(\lambda)}(\eta_i)\,\mathbf{T}^{(\lambda)}(\mathbf{s},\boldsymbol{\omega}), \tag{A.1}$$

with tensor groups $\mathbf{T}^{(\lambda)}$ as defined by Apsley and Leschziner:[2]

$$\begin{array}{lcllcl}
\mathbf{T}^{(1)} &=& \mathbf{s}, & \mathbf{T}^{(6)} &=& \boldsymbol{\omega}^2\mathbf{s}+\mathbf{s}\boldsymbol{\omega}^2-\{\boldsymbol{\omega}\}\mathbf{s}-\frac{2}{3}\{\mathbf{s}\boldsymbol{\omega}^2\}\mathbf{I},\\
\mathbf{T}^{(2)} &=& \boldsymbol{\omega}\mathbf{s}-\mathbf{s}\boldsymbol{\omega}, & \mathbf{T}^{(7)} &=& \boldsymbol{\omega}\mathbf{s}\boldsymbol{\omega}^2-\boldsymbol{\omega}^2\mathbf{s}\boldsymbol{\omega},\\
\mathbf{T}^{(3)} &=& \mathbf{s}^2-\frac{1}{3}\{\mathbf{s}^2\}\mathbf{I}, & \mathbf{T}^{(8)} &=& \mathbf{s}\boldsymbol{\omega}\mathbf{s}^2-\mathbf{s}^2\boldsymbol{\omega}\mathbf{s},\\
\mathbf{T}^{(4)} &=& \boldsymbol{\omega}^2-\frac{1}{3}\{\boldsymbol{\omega}^2\}\mathbf{I}, & \mathbf{T}^{(9)} &=& \boldsymbol{\omega}^2\mathbf{s}^2+\mathbf{s}^2\boldsymbol{\omega}^2-\frac{2}{3}\{\boldsymbol{\omega}^2\mathbf{s}^2\}\mathbf{I},\\
\mathbf{T}^{(5)} &=& \boldsymbol{\omega}\mathbf{s}^2-\mathbf{s}^2\boldsymbol{\omega}, & \mathbf{T}^{(10)} &=& \boldsymbol{\omega}\mathbf{s}^2\boldsymbol{\omega}^2-\boldsymbol{\omega}^2\mathbf{s}^2\boldsymbol{\omega},
\end{array} \tag{A.2}$$

and the scalar functions $G^{(\lambda)}$ for each NLEVM are summarized in the Tables A.1 and A.2, using different derivation methods. The denominators $Q$ and $R$ from Table A.2

Table A.1: Definition of $G^{(\lambda)}$ for NLEVMs, that are based on the derivation method of Apsley and Leschziner.[2]

| $G^{(\lambda)}$ | $n=1$ | $n=2$ | $n=3$ | $n=4$ |
|---|---|---|---|---|
| $G^{(1)}$ | $-\alpha$ | $-\alpha$ | $-\alpha\left(1+\frac{2}{3}\beta^2\eta_1+2\gamma^2\eta_2\right)$ | $-\alpha\left(1+\frac{2}{3}\beta^2\eta_1+2\gamma^2\eta_2-2\beta\gamma^2\eta_4\right)$ |
| $G^{(2)}$ | 0 | $\alpha\gamma$ | $\alpha\gamma$ | $\alpha\gamma\left(1+\frac{13}{6}\beta^2\eta_1+\frac{1}{2}\gamma^2\eta_2\right)$ |
| $G^{(3)}$ | 0 | $2\alpha\beta$ | $2\alpha\beta$ | $2\alpha\beta\left(1+\frac{2}{3}\beta^2\eta_1+\frac{1}{2}\gamma^2\eta_2\right)$ |
| $G^{(4)}$ | 0 | 0 | 0 | $-3\alpha\beta\gamma^2\eta_1$ |
| $G^{(5)}$ | 0 | 0 | $-3\alpha\beta\gamma$ | $-3\alpha\beta\gamma$ |
| $G^{(6)}$ | 0 | 0 | $-3\alpha\gamma^2$ | $-3\alpha\gamma^2$ |
| $G^{(7)}$ | 0 | 0 | 0 | $3\alpha\gamma^3$ |
| $G^{(8)}$ | 0 | 0 | 0 | $3\alpha\beta^2\gamma$ |
| $G^{(9)}$ | 0 | 0 | 0 | $6\alpha\beta\gamma^2$ |
| $G^{(10)}$ | 0 | 0 | 0 | 0 |

Table A.2: Definition of $G^{(\lambda)}$ for NLEVMs, that are based on the derivation method of Pope.[42]

| | $\beta = 0$ (NLEVM Taulbee,[65] simplified) | Full NLEVM of Gatski and Speziale[17] |
|---|---|---|
| $G^{(1)}$ | $-\alpha\left(1-\frac{1}{2}\eta_2\gamma^2\right)Q$ | $-\alpha\left(1-\frac{1}{2}\beta^2\eta_1-\frac{1}{2}\gamma^2\eta_2-\frac{1}{3}\beta^3\eta_3+5\beta\gamma^2\eta_4\right)R$ |
| $G^{(2)}$ | $\alpha\gamma\left(1-2\eta_2\gamma^2\right)Q$ | $\alpha\gamma\left(1+\beta^2\eta_1-2\gamma^2\eta_2+\frac{2}{3}\beta^3\eta_3+2\beta\gamma^2\eta_4\right)R$ |
| $G^{(3)}$ | $0$ | $2\alpha\beta\left(1-\frac{1}{2}\beta^2\eta_1-2\gamma^2\eta_2-\frac{1}{3}\beta^3\eta_3-\beta\gamma^2\eta_4\right)R$ |
| $G^{(4)}$ | $-6\alpha\gamma^4\eta_4 Q$ | $-\alpha\gamma^2\left(3\beta\eta_1+2\beta^2\eta_3+6\gamma^2\eta_4\right)R$ |
| $G^{(5)}$ | $0$ | $-3\alpha\beta\gamma R$ |
| $G^{(6)}$ | $-3\alpha\gamma^2 Q$ | $-3\alpha\gamma^2 R$ |
| $G^{(7)}$ | $3\alpha\gamma^3 Q$ | $3\alpha\gamma^3 R$ |
| $G^{(8)}$ | $0$ | $3\alpha\beta^2\gamma R$ |
| $G^{(9)}$ | $0$ | $6\alpha\beta\gamma^2 R$ |
| $G^{(10)}$ | $0$ | $0$ |

are defined as:

$$Q \equiv \left(\left(1-2\eta_2\gamma^2\right)\left(1-\frac{1}{2}\eta_2\gamma^2\right)\right)^{-1}, \tag{A.3}$$

$$R \equiv \left(1-\frac{7}{6}\beta^2\eta_1+\frac{1}{3}\beta^4\eta_1^2-\frac{5}{2}\gamma^2\eta_2-\frac{8}{3}\beta^2\gamma^2\eta_1\eta_2+\gamma^4\eta_2^2-\frac{1}{3}\beta^3\eta_3 \right. \tag{A.4}$$
$$\left.+\frac{2}{9}\beta^5\eta_1\eta_3-\frac{2}{3}\beta^3\gamma^2\eta_2\eta_3+7\beta\gamma^2\eta_4+8\beta^2\gamma^2\eta_5+\frac{2}{3}\beta^3\gamma^2\eta_1\eta_4-2\beta\gamma^4\eta_2\eta_4\right)^{-1},$$

where the five linear invariants are defined as:

$$\eta_1 = \{\mathbf{s}^2\},\ \eta_2 = \{\boldsymbol{\omega}^2\},\ \eta_3 = \{\mathbf{s}^3\},\ \eta_4 = \{\mathbf{s}\boldsymbol{\omega}^2\},\ \eta_5 = \{\mathbf{s}^2\boldsymbol{\omega}^2\}. \tag{A.5}$$

The coefficients $\alpha, \beta$ and $\gamma$ are used to calibrate the NLEVMs with a simple shear flow, that is characterized by the shear parameter: $\tilde{\sigma} = 1/\sqrt{C_\mu}$, and the anisotropic Reynolds-stresses: $\tilde{a}_{13} = -\sqrt{C_\mu}$, $\tilde{a}_{11}$ and $\tilde{a}_{33}$. For convenience, $\alpha, \beta$ and $\gamma$ are multiplied with the shear parameter $\tilde{\sigma}$ to obtain a new set of coefficents $\bar{\alpha}, \bar{\beta}$ and $\bar{\gamma}$:

$$\bar{\alpha} = \alpha\tilde{\sigma}, \quad \bar{\beta} = \beta\tilde{\sigma}, \quad \bar{\gamma} = \gamma\tilde{\sigma}. \tag{A.6}$$

The results of the calibration are listed in Tables A.3 and A.4. Note that these tables use $A_1$ and $A_2$, which are defined as:

$$A_1 \equiv \frac{\tilde{a}_{11}+\tilde{a}_{33}}{\tilde{a}_{13}}, \quad A_2 \equiv \frac{\tilde{a}_{11}-\tilde{a}_{33}}{\tilde{a}_{13}}. \tag{A.7}$$

Table A.3: Calibration of NLEVMs, that are based on the derivation method of Apsley and Leschziner.[2]

| | $n=1$ | $n=2$ | $n=3$ | $n=4$ |
|---|---|---|---|---|
| $\frac{\bar{\alpha}}{\tilde{a}_{13}}$ | $-2$ | $-2$ | $-\left(1+\sqrt{1-3A_1^2+A_2^2}\right)$ | $-2\left(1+\frac{3}{4}A_1^2-\frac{1}{4}A_2^2\right)^{-1}$ |
| $\bar{\beta}$ | - | $-\frac{3}{2}A_1$ | $-3A_1\left(1+\sqrt{1-3A_1^2+A_2^2}\right)^{-1}$ | $-\frac{3}{2}A_1$ |
| $\bar{\gamma}$ | - | $-\frac{1}{2}A_2$ | $-A_2\left(1+\sqrt{1-3A_1^2+A_2^2}\right)^{-1}$ | $-\frac{1}{2}A_2$ |

Table A.4: Calibration of NLEVMs, that are based on the derivation method of Pope.[42]

| | $\beta=0$ (NLEVM Taulbee,[65] simplified) | Full NLEVM of Gatski and Speziale[17] |
|---|---|---|
| $\frac{\bar{\alpha}}{\tilde{a}_{13}}$ | $-2\left(1+\frac{1}{4}A_2^2\right)$ | $-2\left(1-\frac{3}{4}A_1^2+\frac{1}{4}A_2^2\right)$ |
| $\bar{\beta}$ | 0 | $-\frac{3}{2}A_1$ |
| $\bar{\gamma}$ | $-\frac{1}{2}A_2$ | $-\frac{1}{2}A_2$ |

The calibrated coefficients $\alpha$, $\beta$ and $\gamma$ from the NLEVMs that are based on the iterative method of Apsley and Leschziner, are mulitplied with $f_P$:

$$\alpha' = f_P\alpha, \qquad \beta' = f_P\beta, \qquad \gamma' = f_P\gamma, \tag{A.8}$$

with $f_P$ defined as:

$$f_P(\sigma/\tilde{\sigma}) = \frac{2f_0}{1+\sqrt{1+4f_0(f_0-1)\left(\frac{\sigma}{\tilde{\sigma}}\right)^2}}, \qquad f_0 = \frac{C_R}{C_R-1}, \tag{A.9}$$

where $\sigma$ is the shear parameter: $\sigma \equiv \frac{k}{\varepsilon}\sqrt{(U_{i,j})^2}$, $\tilde{\sigma}$ is the shear parameter in the calibration flow and $C_R$ is the Rotta constant.

# Appendix B

## GUIDELINES FOR THE $k$-$\varepsilon$-$f_P$ MODEL

In this Chapter, a number of guidelines for applying the $k$-$\varepsilon$-$f_P$ EVM to wind turbine wakes is given. The $k$-$\varepsilon$-$f_P$ EVM is an isotropic turbulence model with a variable eddy viscosity coefficient $C_\mu$, where $f_P$ defines the variable part of $C_\mu$. The $k$-$\varepsilon$-$f_P$ EVM is presented in Chapter 4.

In EllipSys3D, (the in-house flow solver of the Technical University of Denmark,[36,62]) the $k$-$\varepsilon$-$f_P$ EVM is activated in *input.dat* by adding a single line:

```
C_R 4.5
```

in the input block of the standard k-epsilon model:

```
...
turbulence kepsilon
ke_version rough
loglaw true
roughness <roughness height>
cmu 0.03
ce1 1.20941505330508
ce2 1.92
prtke_ke 1
pred_ke 1.3
kappa 0.4
C_R 4.5
...
```

The value after the keyword `C_R` is the value of the Rotta constant $C_R$, which is the only constant in $f_P$. Section 3.3.2.1 shows that $C_R$ has a large influence on the wake recovery. Therefore, $C_R$ is an important parameter that should be chosen carefully. In Section 4.4.1.3, a calibration of $C_R$ against LES is performed using 8 single wind turbine wake cases, with the constants of the standard the $k$-$\varepsilon$ EVM listed above. From this calibration it is recommended to use $C_R = 4.5$, and it should never be changed to fit a certain measurement case, unless a better calibration indicates a revised value. The $k$-$\varepsilon$-$f_P$ EVM is calibrated for the log region of a neutral ABL, hence: $\tilde{\sigma} = 1/\sqrt{C_\mu}$ (with $C_\mu = 0.03$). The model cannot be used if a boundary layer is not present, e.g., for a wind turbine in

a uniform flow. It is possible to apply the $k$-$\varepsilon$-$f_P$ EVM for non-neutral ABLs, if $\tilde{\sigma}$ can be defined from either a precursor simulation or an expression. It should be noted that the calibration of $C_R$ might be different for a wind turbine wake in a non-neutral ABL, which has not been investigated in the present work.

Section 3.3.2.1 shows that the $C_\mu$ of the $k$-$\varepsilon$-$f_P$ EVM cannot be used to obtain the desired ambient turbulence intensity at hub height, using equation (3.7), as usually performed for the standard the $k$-$\varepsilon$ EVM. Therefore, it is recommend to keep $C_\mu = 0.03$ and tune the ambient turbulence intensity with other parameters, e.g. the roughness height, as motivated in Section 4.4.1.1.

# Bibliography


1. International standard IEC 61400–1, 1999.
2. Apsley, D. D. and Leschziner, M. A. A new low-Reynolds-number nonlinear two-equation turbulence model for complex flows. *International Journal of Heat and Fuid Flow*, 19:209–222, 1998.
3. Aubrun, S., Loyer, S., Hancock, P. E., and Hayden, P. Wind turbine wake properties: Comparison between a non-rotating simplified wind turbine model and a rotating model. *Journal of Wind Engineering and Industrial Aerodynamics*, 120:1–8, 2013.
4. Barthelmie, R. J., Frandsen, S. T., Nielsen, N. M., Pryor, S. C., Réthoré, P.-E., and Jørgensen, H. E. Modelling and measurements of power losses and turbulence intensity in wind turbine wakes at Middelgrunden offshore wind farm. *Wind Energy*, 10:217–228, 2007.
5. Barthelmie, R. J., Frandsen, S. T., Rathmann, O., Hansen, K., Politis, E. S., Prospathopoulos, J., Schepers, J. G., Rados, K., Cabezón, D., Schlez, W., Neubert, A., and Heath, M. Flow and wakes in large wind farms: Final report for UpWind WP8. Technical Report Risø-R-1765, Risø, Roskilde, Denmark, 2011.
6. Barthelmie, R. J., Hansen, K., Frandsen, S. T., Rathmann, O., Schepers, J. G., Schlez, W., Philips, J., Rados, K., Zervos, A., Politis, E. S., and Chaviaropoulos, P. K. Modelling and measuring flow and wind turbine wakes in large wind farms offshore. *Wind Energy*, 12:431–444, 2009.
7. Bechmann, A. *Large-Eddy Simulation of Atmospheric Flow over Complex Terrain*. PhD thesis, DTU-MEK, Denmark, 2007.
8. Bergström, H. Meteorological Conditions at Lillgrund. Technical report, Vattenfall Vindkraft AB, Stockholm, Sweden, 2009.
9. Boussinesq, M. J. *Théorie de l'écoulement tourbillonnant et tumultueux des liquides*. Gauthier-Villars et fils, Paris, France, 1897.
10. Cabezón, D., Migoya, E., and Crespo, A. Comparison of turbulence models for the computational fluid dynamics simulation of wind turbine wakes in the atmospheric boundary layer. *Wind Energy*, 14:909–921, 2011.
11. Calaf, M., Meneveau, C., and Meyers, J. Large eddy simulation study of fully developed wind-turbine array boundary layers. *Physics of Fluids*, 22:015110, 2010.
12. Chen, Y. S. and Kim, S. W. Computation of turbulent flow using an extended turbulence closure model. NASA Contractor Report CR-179204, NASA, USA, 1987.
13. Churchfield, M. J., Lee, S., Moriarty, P. J., Martinez, L. A., Leonardi, S., Vijayaku-

mar, G., and Brasseur, J. G. A Large-Eddy Simulation of Wind-Plant Aerodynamics. In *AIAA Conference, Nashville, USA*, pages 1–19, 2012.

14. Crespo, A. Personal communication. 2012.
15. Dahlberg, J.-Å. Assessment of the Lillgrund windfarm. Technical report, Vattenfall Vindkraft AB, Stockholm, Sweden, 2009.
16. El Kasmi, A. and Masson, C. An extended $k$-$\varepsilon$ model for turbulent flow through horizontal-axis wind turbines. *Journal of Wind Engineering and Industrial Aerodynamics*, 96:103–122, 2008.
17. Gatski, T. B. and Speziale, C. G. On explicit algebraic models for complex turbulent flows. *Journal of Fluid Mechanics*, 254:59–78, 1993.
18. Gaumond, M., Réthoré, P.-E., Ott, S., Peña, A., Bechmann, A., and Hansen, K. S. Evaluation of the wind direction uncertainty and its impact on wake modeling at the Horns Rev offshore wind farm. *Wind Energy*, 17:1169–1178, 2013.
19. Gómez-Elvira, R., Crespo, A., Migoya, E., Manuel, F., and Hernández, J. Anisotropy of turbulence in wind turbine wakes. *Journal of Wind Engineering and Industrial Aerodynamics*, 93:797–814, 2005.
20. Hansen, K. S. Presentation of Lillgrund offshore wind farm and the Siemens SWT-2.3-93 wind turbine. Technical report, EERA DTOC, 2013.
21. Hansen, K. S. WP1 wake model performance validation results for Lillgrund offshore wind farm. Technical report, EERA DTOC, 2013.
22. Hansen, K. S., Barthelmie, R. J., Jensen, L. E., and Sommer, A. The impact of turbulence intensity and atmospheric stability on power deficits due to wind turbine wakes at Horns Rev wind farm. *Wind Energy*, 15:183–196, 2012.
23. Hansen, M. H. Aeroelastic properties of backward swept blades. In *49th AIAA Aerospace Sciences Meeting including the New Horizons Forum and Aerospace Exposition, Orlando, Florida*, 2011.
24. Jensen, L. E. Array efficiency at Horns Rev and the effect of atmospheric stability. In *EWEC, Milan, Italy*, 2007.
25. Jensen, N. O. A note on wind generator interaction. Technical Report Risø-M-2411, Risø National Laboratory, Roskilde, Denmark, 1983.
26. Jonkman, J., Butterfield, S., Musial, W., and Scott, G. Definition of a 5-MW Reference Wind Turbine for Offshore System Development. Technical report, National Renewable Energy Laboratory, 2009.
27. Kelly, M. C. and Gryning, S.-E. Long-term mean wind profiles based on similarity theory. *Boundary-Layer Meteorology*, 136:377–390, 2010.
28. Kim, J., Moin, P., and Moser, R. Turbulence statistics in fully developped channel flow at low Reynolds number. *Journal of Fluid Mechanics*, 177:133–166, 1987.
29. Launder, B. E. An introduction to single-point closure methodology. In Gatski, T. B., Hussaini, M. Y., and Lumley, J. L., editors, *Simulation and Modeling of Turbulent Flows*, pages 243–310. New York: Oxford University Press, 1996.
30. Launder, B. E., Reece, G. J., and Rodi, W. Progress in the development of a

Reynolds-stress turbulence closure. *Journal of Fluid Mechanics*, 68:537–566, 1975.

31. Launder, B. E. and Spalding., D. B. *Mathematical models of turbulence*. Academic Press, London, UK, 1972.
32. Leonard, B. P. A stable and accurate convective modelling procedure based on quadratic upstream interpolation. *Computer Methods in Applied Mechanics and Engineering*, 19:59–98, 1979.
33. Lindenburg, C. and Snel, H. PHATAS-II: program for horizontal axis wind turbine analysis and simulation version II. Technical Report ECN-C–93-038, Energy research Centre of the Netherlands, Petten, The Netherlands, 1993.
34. Machefaux, E., Larsen, G. C., and Rettenmeier, A. Single Wake Meandering, Advection and Expansion - an analysis using an adapted Pulse Lidar and CFD LES-ACL simulations. In *Scientific proceedings of EWEC, Vienna, Austria*, pages 50–55, 2013.
35. Mann, J. The spatial structure of neutral atmospheric surface-layer turbulence. *Journal of Fluid Mechanics*, 273:141–168, 1994.
36. Michelsen, J. A. Basis3d - a platform for development of multiblock PDE solvers. Technical Report AFM 92-05, Technical University of Denmark, Lyngby, Denmark, 1992.
37. Mikkelsen, R. *Actuator Disc Methods Applied to Wind Turbines*. PhD thesis, Technical University of Denmark, Mek dept, Lyngby, Denmark, 2003.
38. Myllerup, L. Non-linear k-$\varepsilon$ Turbulence Model Implementation and Testing. Technical report, Risø National Laboratory, Roskilde, Denmark, 2006.
39. Ott, S. and Nielsen, M. Developments of the offshore wind turbine wake model Fuga. Technical Report E-0046, DTU Wind Energy, Denmark, 2014.
40. Panofsky, H. A. and Dutton, J. A. *Atmospheric Turbulence*. Wiley-interscience, New York, US, 1984.
41. Patankar, S. V. and Spalding, D. B. A calculation procedure for heat, mass and momentum transfer in three-dimensional parabolic flows. *International Journal of Heat and Mass Transfer*, 15:1787–1806, 1972.
42. Pope, S. B. A more general effective-viscosity hypothesis. *Journal of Fluid Mechanics*, 72:331–440, 1975.
43. Pope, S. B. *Turbulent Flows*. Cambridge University Press, Cambridge, UK, 2005.
44. Porté-Agel, F., Wu, Y. T., Lu, H., and J., C. R. Large-eddy simulation of atmospheric boundary layer flow through wind turbines and wind farms. *Journal of Wind Engineering and Industrial Aerodynamics*, 99:154–168, 2011.
45. Prospathopoulos, J. M., Politis, E. S., Rados, K. G., and Chaviaropoulos, P. K. Evaluation of the effects of turbulence model enhancements on wind turbine wake predictions. *Wind Energy*, 14:285–300, 2011.
46. Réthoré, P.-E. *Wind Turbine Wake in Atmospheric Turbulence*. PhD thesis, Aalborg University, Risø DTU, Roskilde, Denmark, 2009.

47. Réthoré, P.-E. and Sørensen, N. N. A discrete force allocation algorithm for modelling wind turbines in computational fluid dynamics. *Wind Energy*, 15:915–926, 2012.
48. Réthoré, P.-E., van der Laan, M. P., Troldborg, N., Zahle, F., and Sørensen, N. N. Verification and validation of an actuator disc model. *Wind Energy*, 17:919–937, 2014.
49. Rhie, C. M. and Chow, W. L. Numerical study of the turbulent fow past an airfoil with trailing edge separation. *AIAA Journal*, 21:1525–1532, 1983.
50. Richards, P. J. and Hoxey, R. P. Appropriate boundary conditions for computational wind engineering models using the $k$-$\varepsilon$ turbulence model. *Journal of Wind Engineering and Industrial Aerodynamics*, 46,47:145–153, 1993.
51. Rodi, W. A new algebraic relation for calculating the Reynolds stress. *Zeitschrift for angewandte mathematik und mechanik*, 56:227–238, 1976.
52. Rotta, J. C. Statistische Theorie nichthomogener Turbulenz. *Z. Physics*, 129:547–572, 1951.
53. Roy, C. J. Grid Convergence Error Analysis for Mixed-Order Numerical Schemes. *American Institute of Aeronautics and Astronautics Journal*, 41(4):595–604, 2003.
54. Sanderse, B., van der Pijl, S. P., and Koren, B. Review of computational fluid dynamics for wind turbine wake aerodynamics. *Wind Energy*, 14:799–819, 2011.
55. Sathe, A., Gryning, S.-E., and Peña, A. Comparison of the atmospheric stability and wind profiles at two wind farm sites over a long marine fetch in the North Sea. *Wind Energy*, 14:767–780, 2011.
56. Schepers, J. G. Personal communication. 2012.
57. Schepers, J. G., Obdam, T. S., and Prospathopoulos, J. Analysis of wake measurements from the ECN Wind Turbine Test Site Wieringermeer, EWTW. *Wind Energy*, 15:575–591, 2012.
58. Shen, W. Z., Mikkelsen, R., Sørensen, J. N., and Bak, C. Tip loss corrections for wind turbine computations. *Wind Energy*, 8:457–475, 2005.
59. Shen, W. Z., Sørensen, J. N., and Mikkelsen, R. Tip loss corrections for Actuator/Navier-Stokes computations. *Solar Energy Engineering*, 127:209–213, 2005.
60. Shih, T. H., Liou, W. W., Shabbir, A., Yang, Z., and Zhu, J. A new $k$-$\varepsilon$ eddy viscosity model for high Reynolds number turbulent flows-model development and validation. Technical report, NASA, USA, 1994.
61. Sørensen, J. N. and Shen, W. Z. Numerical modelling of wind turbine wakes. *Journal of Fluids Engineering*, 124:393–399, 2002.
62. Sørensen, N. N. *General purpose flow solver applied to flow over hills*. PhD thesis, Risø National Laboratory, Roskilde, Denmark, 1994.
63. Sørensen, N. N., Bechmann, A., Johansen, J., Myllerup, L., Botha, P., Vinther, S., and Nielsen, B. S. Identification of severe wind conditions using a

Reynolds Averaged Navier-Stokes solver. *Journal of Physics: Conference series*, 75(012053):1–13, 2007.

64. Sumner, J. and Masson, C. $k$-$\varepsilon$ simulations of the neutral atmospheric boundary layer: analysis and correction of discretization errors on practical grids. *International Journal for Numerical Methods in Fluids*, 70(6):724–741, 2012.
65. Taulbee, D. B. An improved algebraic Reynolds stress model and corresponding nonlinear stress model. *Physics of Fluids*, A4 11:2555–2561, 1992.
66. Taylor, G. J. Wake measurements on the Nibe turbines in Denmark. Contractor Report ETSU WN 5020, National Power - Technology and Environment Centre, 1990.
67. Troen, I. and Petersen, E. L. *European Wind Atlas*. Risø National Laboratory, Roskilde, 1989.
68. Troldborg, N. Personal communication. 2014.
69. Troldborg, N., Larsen, G. C., Madsen, H. A., Hansen, K. S., Sørensen, J. N., and Mikkelsen, R. Numerical simulations of wake interaction between two wind turbines at various inflow conditions. *Wind Energy*, 14:859–876, 2011.
70. Troldborg, N., Sørensen, J. N., and Mikkelsen, R. Numerical simulations of wake characteristics of a wind turbine in uniform inflow. *Wind Energy*, 13:86–99, 2010.
71. Troldborg, N., Sørensen, J. N., Mikkelsen, R., and Sørensen, N. N. A simple atmospheric boundary layer model applied to large eddy simulation of wind turbine wakes. *Wind Energy*, 17:657–669, 2014.
72. Troldborg, N., Zahle, F., Sørensen, N. N., and Réthoré, P.-E. Comparison of wind turbine wake properties in non-uniform inflow predicted by different rotor models. In *Torque conference 2012, Oldenburg, Germany*, 2012.
73. Troldborg, N., Zahle, F., Sørensen, N. N., and Réthoré, P.-E. Comparison of wind turbine wake properties in non-sheared inflow predicted by different CFD rotor models. *Wind Energy*, 2014. Published online: DOI: 10.1002/we.1757.
74. van der Laan, M. P., Sørensen, N. N., Réthoré, P.-E., Mann, J., Kelly, M. C., and Schepers, J. G. Nonlinear Eddy Viscosity Models applied to Wind Turbine Wakes. In *Proceedings for the ICOWES2013, Copenhagen, Denmark*, pages 514–525, 2013.
75. van der Laan, M. P., Sørensen, N. N., Réthoré, P.-E., Mann, J., Kelly, M. C., and Troldborg, N. The $k$-$\varepsilon$-$f_p$ model applied to double wind turbine wakes using different actuator disk force methods. *Wind Energy*, 2014. Published online: DOI: 10.1002/we.1816.
76. van der Laan, M. P., Sørensen, N. N., Réthoré, P.-E., Mann, J., Kelly, M. C., Troldborg, N., Schepers, J. G., and Machefaux, E. An improved $k$-$\varepsilon$ model applied to a wind turbine wake in atmospheric turbulence. *Wind Energy*, 2014. Published online: DOI: 10.1002/we.1736.
77. van der Laan, M. P., Storey, R. C., Sørensen, N. N., Norris, S. E., and Cater, J. E. A

CFD code comparison of wind turbine wakes. *Journal of Physics: Conference Series*, 524(012140):1–10, 2014.

78. Wallin, S. and Johansson, A. V. An explicit algebraic reynolds stress model for incompressible and compressible turbulent flows. *Journal of Fluid Mechanics*, 403:89–132, 2000.

79. Wu, Y. T. and Porté-Agel, F. Large-Eddy Simulation of Wind-Turbine Wakes: Evaluation of Turbine Parametrisations. *Boundary-Layer Meteorology*, 138:345–366, 2011.

80. Wu, Y. T. and Porté-Agel, F. Modeling turbine wakes and power losses within a wind farm using LES: An application to the Horns Rev offshore wind farm. In *Proceeding for the ICOWES2013, Copenhagen, Denmark*, pages 537–548, 2013.

81. Zahle, F. and Sørensen, N. N. Overset grid flow simulation on a modern wind turbine. In *AIAA-2008-6727, Honolulu, Hawaii*, 2008.

This dissertation is submitted in partial fulfilment of the requirements for the degree of Doctor of Philosophy in Engineering at the Technical University of Denmark. The work was done at the Aero-elastic Design Section of the Department of Wind Energy with support of the Center for Computational Wind Turbine Aerodynamics and Atmospheric Turbulence, which is funded by the Danish Council for Strategic Research, grant number 09-067216.

Principal supervisor: Prof. Niels N. Sørensen.
Co-supervisors: Dr. Pierre-Elouan Réthoré, Prof. Jakob Mann and Dr. Mark C. Kelly.
Examiners: Prof. Christian Masson, Dr. Jens I. Madsen and Dr. Robert F. Mikkelsen.

**DTU Wind Energy**

ISBN 978-87-93278-31-8